

## Abstract

# Nonreciprocity in active Josephson junction circuits

Archana Kamal

2013

This thesis work explores different ideas for realizing nonreciprocal photon dynamics using active parametric circuits based on Josephson junctions. The motivation stems from developing non-magnetic alternatives to existing nonreciprocal devices, invariably employing magnetic materials and fields and hence limited in their application potential for use with on-chip microwave superconducting circuits. The main idea rests on the fact the “pump” wave (or the carrier) in an active nonlinear system changes the phase of a small modulation signal just as the magnetic field rotates the polarization of the wave propagating in a Faraday medium. All the implementations discussed in this thesis draw from the basic idea of chaining together discrete parametric processes with an optimal phase difference between the respective pumps to realize nonreciprocity. Though discussed specifically for microwave applications using Josephson junctions as a platform, the ideas presented here are generic enough to be adopted for any nonlinear system implementing frequency mixing.

# **Nonreciprocity in active Josephson junction circuits**

A Dissertation  
Presented to the Faculty of the Graduate School  
of  
Yale University  
in Candidacy for the Degree of  
Doctor of Philosophy

by  
Archana Kamal

Dissertation Director: Prof. Michel H. Devoret

March 11, 2013

Copyright © 2013 by Archana Kamal  
All rights reserved.

*For Mumma and Papa.*

---

## Acknowledgements

---

There have been many people who have been instrumental for the successful completion of this thesis. When I look back, it appears as quite an exciting journey, with many elements of a dramatic tale. The opening credits undoubtedly belongs to my advisor Michel Devoret. Before joining graduate school, I had broken up with physics and it was awkward meeting each other at Yale after a year long separation. It was Michel's class in Mesoscopic Physics which played the cupid and rekindled my interest in my old love quantum mechanics. He introduced us gently and gave me enough time reclaiming my ground in this relationship. Over the years, I not only learnt some insider tips on how to survive a successful marriage with physics from him, but also how to have a lifelong love affair with science in general. His omniscient knowledge, coupled with a work ethic that involves eating, drinking and breathing physics, continues to amaze me. Our longest discussion till date went for over 8 hours! — I think I am going to especially miss my chats with him.

The pleasure of working on Becton fourth floor can be largely attributed to the presence of ace directors such as Steve Girvin and Rob Schoelkopf. With his charming and sharp wit, Steve can infuse fun and clarity in most abstruse concepts. His talks have always been a real crowd puller (the lectures he gave at Les Houches summer school in July 2011 will remain one of my all-time favorites!). Rob's approach of deconstructing and understanding a phenomenon to its bare bones encouraged novices like me to think deeply about their parts, without los-

ing sight of the final resolution of the plot. I am also especially grateful to John Clarke at UC Berkeley who has been a wonderful collaborator and a constant source of inspiration and ideas. John's kindness and patience teaches, by example, what all it takes to be an icon besides just scientific genius. I owe a special thanks to Leonid Glazman with whom I had the steepest learning curves during discussions, both inside and outside the classroom. I would also like to thank Dan Prober and Doug Stone for serving on my thesis committee; they have been instrumental in making Applied Physics department what it is today.

The opportunity to work in Qlab has been rewarding due to its members, in no small measure. Starting out with a few thespians like Vijay, Chad and Vlad, it was fun to watch the Qlab-cast evolve into a true multi-starrer. The present generation of Qlabbers — Baleegh, Ioan, Michael, Shyam, Flavius, Kurtis, Katrina, Ananda, Yehan, Zlatko and Anirudh — form a really dynamic bunch of performers. Nick Masluk deserves a special mention for keeping the show going during the times when I was absconding from BC420 and juggling with theory at the far end of the corridor. He also pushed me (relentlessly at times!) to overcome my initial fear with performing stunts such as transferring helium. Besides you just got to admire a guy who builds his own table-top refrigerator for cooling soda cans (when he doesn't even drink them!!!). It was also great fun to share the floor with colleagues from RSL, who precluded the need to look afar for blockbusters. I would also like to thank my officemates Dan, Anthony, Joel, Faustin and Chris from the Prober lab for making our office the most cinematographic place on the floor (hands down), great to unwind with a refreshing hour of juicy gossip! Also, science is a play where the crew is as important as the cast — thanks to Giselle, Maria, Devon and Terry for making it possible for us to do what we do by taking care of all the chaos backstage (that too with a smile!). You guys are our real heroes.

As in a stage show, the closing credits here hold special significance. So lastly,

I would like to thank my family, especially my parents who took a big leap of faith in allowing me to be so far away from them in order to pursue physics. Their unconditional love and support is reflected in everything I have today and I do in future. A warm thanks to my brother Anupam, who has always been my most engaged audience, hooting/cheering (sometimes even at inopportune moments!) and lending much needed relief during dry spells. I am also grateful to my in-laws, bhaiya and bhabhi who have been most encouraging at all times; especially didi and jiju who have been like my academic godparents. And finally, I thank the most important person without whom this script would have never seen light of the day, who has been my ultimate critic, who has prompted me when I have forgotten my lines, who has always cheered the loudest on my most humble performances, and who has given me the courage to prepare for the next act — my husband Nishant. This is for you.

---

# Contents

---

<b>Acknowledgements</b>	<b>iv</b>
<b>Contents</b>	<b>vii</b>
<b>List of Figures</b>	<b>x</b>
<b>List of Symbols</b>	<b>xiii</b>
<b>Foreword</b>	<b>1</b>
Thesis Overview . . . . .	3
<b>1 Background Concepts</b>	<b>7</b>
1.1 A primer on reciprocity . . . . .	8
1.2 Nonreciprocity with magnetic fields: Faraday Rotation . . . . .	13
1.3 Nonreciprocity without magnetic fields . . . . .	17
1.3.1 Traveling wave parametric amplifiers (TWPA) . . . . .	18
1.4 Chain of parametric circuits: Discrete TWPAs(!) . . . . .	22
1.4.1 Josephson parametric circuits . . . . .	23
1.4.2 Minimal model for parametric wave mixing . . . . .	25
1.5 Implementations of JJ-based frequency mixers . . . . .	34
1.5.1 dc-biased single Josephson junction mixer . . . . .	34
1.5.2 Josephson parametric converter (JPC) . . . . .	38

<b>2</b>	<b>Active Circulator: Nonreciprocity without gain</b>	<b>42</b>
2.1	Proposed scheme . . . . .	43
2.2	Scattering description of the individual components . . . . .	45
2.3	Transfer Matrix Description . . . . .	50
2.4	Results and viability of the design . . . . .	54
2.5	Comparison of passive and active circulator designs . . . . .	57
<b>3</b>	<b>Nonreciprocity in frequency domain</b>	<b>63</b>
3.1	Resistively-shunted junction (RSJ): A case study . . . . .	64
3.2	Harmonic Balance Treatment . . . . .	67
3.2.1	Steady-state response: I-V characteristics . . . . .	68
3.2.2	RF response: Symmetry breaking in frequency conversion . . . . .	74
3.3	Fluctuation Spectrum of the RSJ . . . . .	81
3.4	Discussion . . . . .	83
<b>4</b>	<b>Directional Amplification: Nonreciprocity with gain</b>	<b>86</b>
4.1	Analytically Solvable Model for the dc SQUID . . . . .	88
4.1.1	Harmonic balance treatment . . . . .	94
4.2	Calculation of SQUID Dynamics . . . . .	96
4.2.1	Steady state response: I-V characteristics . . . . .	96
4.2.2	Steady state response: Josephson harmonics . . . . .	99
4.2.3	RF response: Scattering Matrix . . . . .	100
4.3	Power Gain of the SQUID . . . . .	104
4.4	Noise Temperature . . . . .	109
4.5	Discussion . . . . .	114
<b>5</b>	<b>Conclusions</b>	<b>118</b>
5.1	Tunable nonreciprocity with photons . . . . .	118
5.2	Novel dynamical cooling protocols . . . . .	120

5.3 Artificial magnetic fields . . . . .	121
<b>A Faraday Rotation vs Optical Activity</b>	<b>123</b>
A.1 Optical Activity . . . . .	124
A.2 Faraday Rotation . . . . .	126
<b>B Input-output theory</b>	<b>129</b>
<b>C Modulation ellipse</b>	<b>134</b>
<b>D Derivation of the JRM eigenmodes</b>	<b>139</b>
<b>E Loop Variables for the dc SQUID</b>	<b>144</b>
<b>F Static analog circuit for the SQUID</b>	<b>146</b>
<b>Bibliography</b>	<b>149</b>

---

## List of Figures

---

1.1	Reciprocity (upper panel) vs nonreciprocity (lower panel). . . . .	8
1.2	E and H fields for a closed loop conductor. . . . .	10
1.3	Optical Activity vs Faraday rotation. . . . .	15
1.4	Schematic of a ferrite-based circulator. . . . .	16
1.5	Traveling wave parametric amplifiers (TWPA). . . . .	20
1.6	Minimal model for a parametric three-wave mixer. . . . .	26
1.7	Different representations of a modulated signal. . . . .	30
1.8	Phase-sensitive nature of parametric up- and downconversion. . .	31
1.9	Josephson junction in running/voltage regime. . . . .	35
1.10	Circuit schematic of a Josephson ring modulator (JRM). . . . .	39
2.1	Reversible I-Q modulator circuit. . . . .	44
2.2	Description of the active circulator . . . . .	45
2.3	Variation of the difference between forward and backward transmission coefficients of active circulator. . . . .	55
2.4	Bandwidth of the active circulator design. . . . .	55
2.5	Passive JJ-based circulator. . . . .	57
2.6	Experimental demonstration of the active circulator idea using IQ mixers. . . . .	60
2.7	Comparison of passive and active circulator designs . . . . .	61
2.8	Non-commutativity of phase-sensitive rotations . . . . .	62

3.1	Current-biased resistively shunted junction (RSJ). . . . .	66
3.2	Frequency landscape for a junction in voltage state. . . . .	68
3.3	Phase evolution of current-biased RSJ. . . . .	71
3.4	DC characteristics of an RSJ. . . . .	73
3.5	Equivalence between a junction in voltage state and a paramp. . . . .	75
3.6	Symmetry breaking in frequency conversion by an RSJ. . . . .	79
3.7	Monochromatic vs colored (multiharmonic) pumps. . . . .	80
4.1	Microstrip design of the SQUID. . . . .	87
4.2	Circuit schematic of a conventional MWSA. . . . .	89
4.3	SQUID potential profile. . . . .	90
4.4	Equivalent input-output model of the SQUID. . . . .	92
4.5	Frequency landscape of common and differential modes of the SQUID. . . . .	95
4.6	Static transfer function of the SQUID. . . . .	97
4.7	Phase trajectory in 2D SQUID potential. . . . .	100
4.8	RF scattering response of the SQUID. . . . .	103
4.9	Different representations of a two-port network and analog configurations for the dc SQUID. . . . .	107
4.10	Power gain of the MWSA. . . . .	108
4.11	Directionality of the MWSA. . . . .	109
4.12	Caves added noise number for the MWSA. . . . .	113
4.13	SNR deterioration in MWSA with signal frequency. . . . .	115
5.1	Double JRM based active circulator design. . . . .	120
A.1	Faraday Rotation. . . . .	127
B.1	Input-output theory . . . . .	130
C.1	Modulation ellipse representation of two phasors. . . . .	136

C.2	Representation of different modulation schemes. . . . .	138
D.1	Simplified circuit model for the Josephson Ring Modulator (JRM). .	140
E.1	Equivalence between the SQUID differential mode and the op-amp input variables . . . . .	144
F.1	Equivalent low frequency circuit for a SQUID for calculation of uni- lateral power gain . . . . .	147
F.2	Comparison of the low frequency power gains calculated using the RF scattering method and the quasistatic calculation. . . . .	148

---

## List of Symbols

---

### *Constants*

$c$	speed of light
$k_B$	Boltzmann constant
$\Phi_0$	flux quantum ( $\equiv h/(2e) \approx 2 \times 10^{-15}$ WB)
$\varphi_0$	reduced flux quantum ( $\equiv \hbar/2e$ )
$R_q$	reduced superconducting resistance quantum ( $\equiv \hbar/(2e)^2 \approx 1$ k $\Omega$ )

### *Abbreviations*

JJ	Josephson junction
MWSA	microwave SQUID amplifier
MSA	microstrip SQUID amplifier
JRM	Josephson ring modulator
LCP	left-circularly polarized
RCP	right-circularly polarized
RSJ	resistively shunted junction
SIS	superconductor-insulator-superconductor
SQUID	superconducting quantum interference device
TWPA	traveling wave parametric amplifier

### *Roman letters*

$A_N$	Caves added noise number
-------	--------------------------

$\tilde{A}$	wave amplitudes for a plane wave travelling in 3D [dimensions = (watt/area) <sup>1/2</sup> ]
$A(t)^{\text{in/out}}$	input-output wave amplitudes for signals travelling on a 1D transmission line [dimensions = (watt) <sup>1/2</sup> ]
$A_i^{\text{in/out}}$	input-output wave amplitudes associated with the fourier component at frequency $\omega_i$ [dimensions = (action) <sup>1/2</sup> ]
$a_i^{\text{in/out}}$	reduced input-output wave amplitudes associated with the fourier component at frequency $\omega_i$ [dimensions = (time) <sup>1/2</sup> ]
$C_i$	capacitance of an oscillator $i$
<b>E</b>	electric field
$E_J$	Josephson energy
$G_P$	power gain of an amplifier
$g$	gain coefficient in a fibre-optic amplifier [dimensions = length <sup>-1</sup> ]
<b>H</b>	magnetic field
$\mathbb{H}$	hybrid or op-amp matrix
<b>I</b>	Current vector (components denote different spatial or temporal (frequencies) ports)
$I^i$	current associated with a spatial channel $i$
$I_B$	dc bias current
$I_0$	critical current of a Josephson junction
$I_{RF}$	rf current
$I - Q$	in-phase/quadrature; usually referred to as a modulation scheme
<b>J</b>	current density
$k$	wave vector
$\Delta k$	phase mismatch
$L_J$	Josephson inductance
$L_i$	inductance of an oscillator $i$
$M$	mutual inductance
$n_2$	nonlinear refractive index of a $\chi_2$ medium

$q_i$	cross 'reflections' between different spatial ports operating at same frequency $\omega_i$
$R_i$	resistance associated with an oscillator $i$
$R_{dyn}$	dynamic resistance
$r_i$	reflection coefficient at frequency $\omega_i$
$\mathbb{S}$	scattering matrix
$\bar{S}_{VV}$	symmetrized spectral density of voltage fluctuations
$\bar{S}_{JJ}$	symmetrized spectral density of fluctuations in circulating current of SQUID
$\bar{S}_{VJ}$	symmetrized spectral density of correlated fluctuations in circulating current and output voltage in SQUID
$s_d$	scattering amplitude for downconversion with conjugation
$s_u$	scattering amplitude for upconversion with conjugation
$\mathbb{T}$	transfer matrix
$T_N$	noise temperature
$t_d$	scattering amplitude for downconversion without conjugation
$t_u$	scattering amplitude for upconversion without conjugation
$\mathbb{U}$	unity matrix
$\mathbf{V}$	Voltage vector (components denote different spatial or temporal (frequencies) ports)
$V^i$	voltage associated with a spatial channel $i$
$V_{dc}$	dc voltage
$V_{RF}$	rf voltage
$v_{\pm\mp}, v$	scattering amplitudes for mixing between upper and lower sidebands
$\mathbb{Y}$	admittance matrix
$\mathbb{Y}_J$	junction admittance matrix
$\mathbb{Z}$	impedance matrix
$Z_i$	characteristic impedance of a transmission line addressing port $i$

## Greek letters

$\alpha$	parametric coupling strength
$\beta_L$	dimensionless parameter quantifying SQUID loop inductance
$\Gamma_i$	decay rate of an oscillator $i$
$\delta_i$	reduced detuning of input frequency from bare resonance of oscillator $i$
$\epsilon$	permiitivity
$\varepsilon$	dimensionless external bias parameter ( $\equiv \omega_0/\omega_B$ )
$\Phi_{\text{ext}}$	external flux bias
$\phi$	phase angle (usually associated with the pump or carrier wave)
$\varphi$	gauge invariant phase difference across a junction
$\varphi^C$	common phase difference associated with two junctions
$\varphi^D$	differential phase difference associated with two junctions
$\varphi_{\text{ext}}$	dimensionless parametrization of external flux bias ( $\equiv \Phi_{\text{ext}}/\varphi_0$ )
$\mu$	permeability
$\lambda_V$	voltage gain of an amplifier
$\lambda_I'$	reverse current gain of an amplifier
$\theta$	phase shift
$\Omega_c$	dimensionless parameter quantifying junction capacitance in SQUID
$\Omega_i$	dimensionless frequency defined with respect to external bias ( $\equiv \omega_i/\omega_B$ )
$\tilde{\omega}$	voltage expressed in equivalent frequency units
$\hat{\omega}$	current expressed in equivalent frequency units
$\omega^{\text{in/out}}$	input-output wave amplitudes $A^{\text{in/out}}$ expressed in equivalent frequency units
$\omega_B$	dc bias current $I_B$ expressed in equivalent frequency units

$\omega_0$	characteristic Josephson frequency ( $\equiv I_0 R / \varphi_0$ )
$\omega_J$	Josephson oscillation frequency ( $\equiv \langle V_J \rangle / \varphi_0$ )
$\omega_{pl}$	plasma frequency of oscillation inside a Josephson well
$\omega_P$	pump frequency
$\omega_S$	signal frequency
$\omega_I$	idler frequency ( $\omega_P - \omega_S$ )
$\omega_c$	carrier frequency
$\omega_m$	modulating frequency
$\omega_+$	frequency of upper side band ( $\omega_c + \omega_m$ )
$\omega_-$	frequency of lower side band ( $\omega_c - \omega_m$ )

---

# Foreword

---

Symmetries reveal the regularities in physical laws and help us separate the definite from the whimsical and unpredictable. They allow us to formulate a coherent description of nature immune to specificities of initial conditions, and identify universal conservation laws. For instance, it is the invariance of physical laws under space and time translations that yields conservation of momentum and energy. Although the unifying thread between the physics of different systems is symmetry, much of what we observe is rooted in instances of symmetry breaking. A recent example is offered by the discovery of the Higgs boson which predicates a symmetry breaking mechanism believed to lend mass to all elementary particles. In this thesis, we deal with the breaking of a specific symmetry called reciprocity.

Reciprocity refers to a symmetry in the dynamics of a system under an interchange of source and observer. It is ubiquitous in its appeal with applicability ranging from

- optics — symmetry in transmission of light under an exchange of source and detector (Helmholtz reciprocity),
- acoustics/geology — symmetry in transmission of sound/seismic waves under an exchange of source and detector
- thermodynamics — symmetry in particle and heat flows under temperature and pressure differences (Onsager reciprocity)

- mechanics — symmetry under exchange between stresses and induced displacements in elastic bodies

to even (!)

- religion — “So in everything, do to others what you would have them do to you, for this sums up the Law and the Prophets.” (Matthew 7:12)

We will concentrate on the physics of breaking reciprocity in the realm of electromagnetism. Besides being an intriguing theoretical problem in its own right, the realization of nonreciprocity in light transmission provides crucial practical applications across a wide spectrum of systems. Conventional nonreciprocal devices, such as circulators and isolators, rely on magnetic fields to break the reciprocal symmetry of wave propagation by implementing a nonreciprocal rotation of polarization vector of light known as Faraday rotation. The critical functionality provided by such devices is marred by the adversity accompanying the use of magnetic materials and fields which are a major roadblock in monolithic integration of such devices. This predicament is especially shared by superconducting quantum circuits, which on one hand rely on the nonreciprocal components in the measurement chains for preserving the delicate quantum coherence by blocking noisy signals from entering the sample stage, and on the other are endangered due to their deleterious magnetic effects. In addition, nonreciprocal components are an integral part of any measurement scheme relying on parametric amplifiers which have emerged as one of the most promising low-noise quantum measurement systems. Most of these amplifiers operating at microwave frequencies are reflection-based amplifiers i.e. they amplify the desired signal in reflection and are, therefore, totally dependent on circulators and isolators for a usable separation of input and output signals. The above concerns are especially relevant in the wake of huge strides in superconducting qubit technology in recent years with coherence times fast approaching the fault-tolerant computation threshold.

This has led to increasingly stringent experimental requirements on both qubit environment and measurement — both of which crucially involve the circulators and isolators. Thus, finding viable practical alternatives that can overcome the weaknesses presented by the current magnetic technology for nonreciprocity has turned into a compelling research activity.

In addition to immediate relevance, realization of non-magnetic nonreciprocity goes a long way on the path to the long cherished goal of integrated microwave and optical technology. A milestone in this direction is to build systems that can exhibit nonreciprocal (or directional) low-noise amplification and hence fulfil the noise-isolation and measurement requirement in one shot.

In this thesis we will show that it is possible to realize (tunable!) nonreciprocal transmission of microwave light using active parametric devices based on Josephson junctions. Further, we will focus on both flavors of nonreciprocal transmission — *without* and *with* amplification of the signal. While the former simulates the circulator action, the latter can be exploited to achieve directional amplification. In addition to providing integrable nonreciprocal devices, such schemes offer us a novel in-situ knob for controlling/steering light at single-photon level which can open doors to qualitative new physics.

## Thesis Overview

In this section, we include a brief synopsis of the main contributions of this thesis work, which will hopefully excite the reader enough to undertake the exercise of reading the remaining manuscript.

In chapter 1, we begin with an introduction of underlying concepts of nonreciprocity and motivate the importance of non-magnetic on-chip realizations by presenting a brief review of ideas on passive options using magnetic components and their associated problems. Traveling wave parametric amplifier (TWPA),

popular in the optical domain, is discussed as a point in case for elucidating the practicality of a non-magnetic directional device. It provides us with the right background to initiate a discussion of Josephson parametric circuits which perform the same wave-mixing operation as in a TWPA but without the debilitating effect of phase mismatch between participating waves. JJ achieve this due to localized nature of their nonlinearity as a circuit element, as compared to the distributed nature of the nonlinear optical medium employed in TWPAs. In addition, JJ being non-dissipative at microwave frequencies, the platform provided by Josephson parametric circuits is quite appealing for applications such as quantum information processing where systems need to be manipulated at the level of few photons. The phase-sensitive nature of parametric rotations, which is illustrated by a scattering analysis of active Josephson circuits, provides the crucial groundwork for following chapters which employ this idea in its different avatars.

In chapter 2, we discuss the symmetry breaking in spatial channels using two Josephson parametric stages performing frequency conversion, arranged back to back. We show that on tuning the difference in the phases of the two pumps to be  $\pi/4$ , this assembly can emulate a circulator-like action and provides a viable alternative to magnetic nonreciprocal devices. The analyzed prototype, based on successive phase-sensitive rotations performed through a parametric process, is quite promising for its universal appeal and should find easy applications in other frequency regimes with a suitable nonlinear element replacing the JJ (such as an acousto-optic modulator for optics).

In chapter 3, we extend the idea of phase-sensitive rotations to demonstrate a novel scheme breaking the symmetry of frequency conversion. As a prototype, we study the resistively-shunted Josephson junction (RSJ) biased with a dc current greater than the critical current of the junction — a possible choice for JJ-based mixers. This leads the phase associated the junction to have a non-zero

average rate of change corresponding to the appearance of a finite voltage across the junction, in contrast to the usual parametric devices which are operated in the zero dc voltage state with the phase displacement is confined to a single well of the Josephson cosine potential. We introduce an extended version of usual input-output theory of circuits which enables us to capture the running state dynamics of the junctions biased in the voltage regime. This allows us a self-consistent formulation of dc and ac dynamics, in accordance with the ac Josephson effect. Subsequent small signal analysis of the junction as a mixer pumped internally by Josephson harmonics shows the emergence of nonreciprocal frequency conversion. This finds an explanation in multi-path ‘interferences’ in the frequency domain, with phases set by the respective parametric rotation.

Chapter 4 tackles the example of a prototypical microwave SQUID amplifier which is the only known nonreciprocal amplifier based on Josephson junctions. The workhorse of this amplifier is a dc SQUID which can be thought of as two RSJs arranged in a flux-biased loop. The microwave characteristics of a SQUID have been a subject of intense interest mostly due to its promising potential as a nonreciprocal preamplifier for quantum-limited measurements. A quantum treatment of SQUID dynamics at microwave frequencies has however remained an open problem, with the most extensive studies being solely numerical. Based on the ideas developed through the course of chapters 2 and 3, we perform an ab-initio analysis of the SQUID dynamics and show the emergence of nonreciprocal gain as a combination of asymmetric frequency mixing between the two spatial modes (common and differential) of the SQUID ring. Besides unravelling the directional nature of the SQUID response, this treatment also enables us to evaluate figures of merit such as total power gain, noise number and directionality as a function of bias parameters and signal frequency.

We conclude with some final thoughts and offer perspectives in chapter 5. Ap-

pendices **A-F** present some useful derivations and annotate various ideas used throughout the thesis.

The work published in following articles is not included in this thesis:

1. **A. Kamal**, A. Marblestone, M. H. Devoret.  
Signal-to-pump back action and self-oscillation in double-pump Josephson parametric amplifier. *Phys. Rev. B* 79, 184301, 2009.
2. V. E. Manucharyan, N. A. Masluk, **A. Kamal**, J. Koch, L. I. Glazman, M. H. Devoret.  
Evidence for coherent quantum phase-slips across a Josephson junction array. *Phys. Rev. B (Editor's Suggestion)* 85, 024521 2012.
3. N. A. Masluk, I. M. Pop, **A. Kamal**, Z. K. Mineev, M. H. Devoret.  
Microwave Characterization of Josephson Junction Arrays: Implementing a Low Loss Superinductance. *Phys. Rev. Lett.* 109, 137002, 2012.

The last two articles are based on the experimental part of my work involving studies on multi-junction systems such as, Fluxonium – a novel, strongly anharmonic superconducting atom, and arrays of Josephson junctions.

---

## Background Concepts

---

*“Symmetry is what we see at a glance.”*

— Blaise Pascal

Reciprocity is a fundamental symmetry of physics which states that a ray of incoming light and its outgoing partner (“in” and “out” defined with respect to any given observer/object) have an identity mapping between their life histories. Rooted in core theoretical principles of electromagnetism, reciprocity occurs in a gamut of practical situations. It is extensively used for analyzing electromagnetic and antenna systems as it provides useful and handy rules such as, if an antenna serves as an excellent transmitter, then reciprocity dictates that it will also work as an excellent receiver! A simple way of stating this is to say “I see the eye that sees me”.<sup>1</sup>

The notion of nonreciprocity breaks this symmetry and leads us to a special situation of “seeing without being seen” (Fig. 1.1). It is worthwhile to note that such symmetry breaking is completely elastic (conserves energy!) and *not* a specialized case of absorption. To gain a perspective on the realization and importance of nonreciprocity, it may be pertinent to develop a better understanding of reci-

---

<sup>1</sup>This popular version explaining the perfect impartiality of physical dynamics under an interchange of source and detector is also known as the Helmholtz reciprocity theorem.

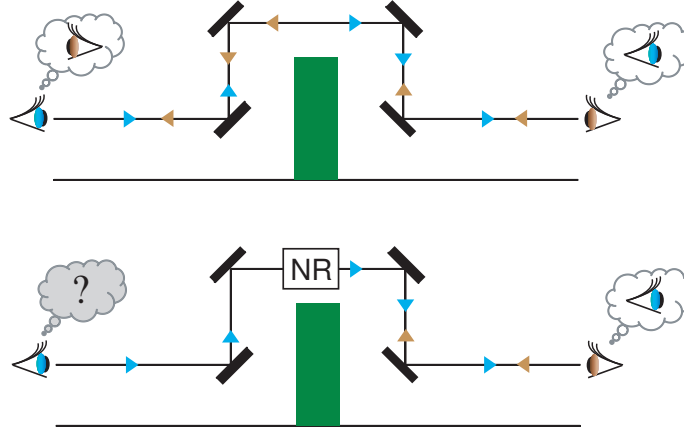


Figure 1.1: **Reciprocity vs nonreciprocity.**

procuity first. In the next section, we present a brief discussion of the underlying concepts in reciprocity. This also provides the appropriate prelude to discuss the concomitant challenges and strategies available for breaking it!

## 1.1 A primer on reciprocity

The earliest and one of the most widely used formal definitions of reciprocity was originally propounded by Rayleigh, which naturally follows from Maxwell's equations describing electromagnetic fields [Landau and Lifshitz, 1984]. The formal statement of the theorem is as follows: if a current density  $\mathbf{J}^{(1)}$  that produces an electric field  $\mathbf{E}^{(1)}$  and a magnetic field  $\mathbf{H}^{(1)}$ , where all three are periodic functions of time with angular frequency  $\omega$ , and in particular they have time-dependence  $\exp(-i\omega t)$  and similarly a second current  $\mathbf{J}^{(2)}$  at the same frequency  $\omega$  which (by itself) produces fields  $\mathbf{E}^{(2)}$  and  $\mathbf{H}^{(2)}$ , then under certain simple conditions on the materials of the medium, the reciprocity principle states that for an arbitrary surface  $S$  enclosing a volume  $V$

$$\int_V [\mathbf{J}^{(1)} \cdot \mathbf{E}^{(2)} - \mathbf{E}^{(1)} \cdot \mathbf{J}^{(2)}] dV = \oint_S [\mathbf{E}^{(1)} \times \mathbf{H}^{(2)} - \mathbf{E}^{(2)} \times \mathbf{H}^{(1)}] \cdot d\mathbf{A}. \quad (1.1)$$

This result is usually applied (and more easily interpreted) for certain special cases where either the surface integral or volume integral vanishes. For example, if the surface  $S$  is chosen to exclude any external sources so that  $\mathbf{J}^{(1)} = \mathbf{J}^{(2)} = 0$ , then the above equations reduces to

$$\oint_S [\mathbf{E}^{(1)} \times \mathbf{H}^{(2)} - \mathbf{E}^{(2)} \times \mathbf{H}^{(1)}] \cdot d\mathbf{A} = 0. \quad (1.2)$$

Alternatively, one can integrate Eq. (1.1) over an infinitely remote surface to kill the surface integrals and obtain,

$$\int_V [\mathbf{J}^{(1)} \cdot \mathbf{E}^{(2)} dV = \int_V \mathbf{E}^{(1)} \cdot \mathbf{J}^{(2)}] dV \quad (1.3)$$

The integrals here are taken only over the volumes of sources 1 and 2 respectively as currents  $\mathbf{J}^{(1)}$  and  $\mathbf{J}^{(2)}$  are zero elsewhere. Both of the above forms are referred to as the Lorentz reciprocity theorem. The basic assumption in the above derivation is the *symmetry of the permittivity  $\epsilon$  and permeability  $\mu$  matrices* describing the system. The concept of reciprocity is not limited to light waves. In fact, the reciprocal symmetry in propagation of light in vacuum holds true for electromagnetic signals in circuits, and is frequently employed to prove symmetries in the descriptions of system response such as those based on impedance and scattering matrices. For description of ohmic electrical circuits (i.e. currents respond linearly to the applied field), we can rewrite Eq. (1.3) as,

$$I^{(1)}V^{(2)} = I^{(2)}V^{(1)} \quad (1.4)$$

where we have used the fact that current density  $J^\alpha$  represents the current crossing a unit area defined perpendicular to the selected branch of the circuit  $I = \int_S \mathbf{J} \cdot \mathbf{n} dA$  and the line integral of electric field over a path connecting the two

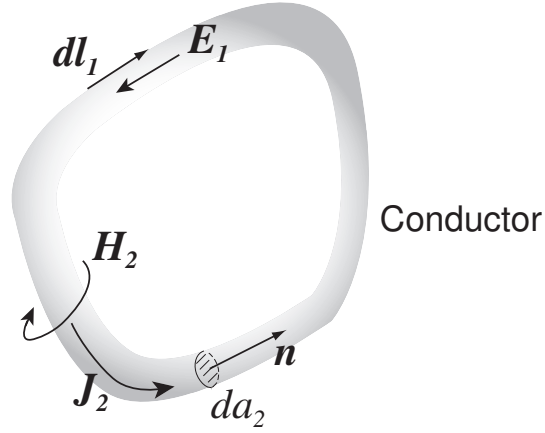


Figure 1.2:  $\mathbf{E}$  and  $\mathbf{H}$  fields for a closed loop conductor.

selected nodes gives the voltage around the loop  $V = \int \mathbf{E} \cdot d\mathbf{l}$  (see Fig. 1.2 elaborating the choice of appropriate surface and line elements for a closed circuit loop). Choosing our imposed stimuli to be either currents

$$V^\alpha = Z^{\alpha\beta} I^\beta \quad (\alpha, \beta = \text{port indices}) \quad (1.5)$$

or voltages,

$$I^\beta = Y^{\beta\alpha} V^\alpha \quad (\alpha, \beta = \text{port indices}), \quad (1.6)$$

Eq. (1.4) yields the reciprocity condition for impedance or admittance response matrices respectively, i.e.

$$Z^{\alpha\beta} = Z^{\beta\alpha} \quad \text{or} \quad Y^{\beta\alpha} = Y^{\alpha\beta}. \quad (1.7)$$

It is important to remind ourselves that the indices in Eq. (1.7) expressing reciprocity between spatially distinct channels (or ports)  $\alpha$ ,  $\beta$  of a circuit implicitly assumes the associated current and voltage signals to be of the same frequency. Nonetheless, one frequently encounters situations in which the system dynam-

ics invariable involve multiple frequencies coupled to the same spatial channel or different frequencies coupled to different spatial channels. These considerations are especially inevitable for understanding reciprocal behavior in the paradigm of nonlinear systems, such as the Josephson junction, which can perform mixing of different frequency or temporal channels. To express reciprocal symmetry for such cases correctly, we need to translate relations in Eq. (1.7) in a language independent of the nature of the port involved (spatial or temporal).

A simple translation is offered by the input-output theory (IOT) which allows us to establish a relationship between the traveling-wave quantities such as input and output waves entering or leaving the circuit respectively, and the standing mode quantities such as currents and voltages defined across fixed terminals/branches of a circuit (see Appendix B for details). IOT models the circuit dynamics as a scattering between incoming and outgoing field amplitudes of the form  $a_i^{\text{in,out}(\alpha)} = (V \mp Z_\alpha I) / \sqrt{\hbar\omega_i Z_\alpha}$ , representing a signal of frequency  $\omega_i$  traveling on a spatial channel represented as a transmission line of characteristic impedance  $Z_\alpha$ ,

$$\begin{pmatrix} \mathbf{a}^{\text{out},(\alpha)} \\ \mathbf{a}^{\text{out},(\beta)} \\ \vdots \end{pmatrix} = \underbrace{\begin{pmatrix} S^{\alpha\alpha} & S^{\alpha\beta} & \dots \\ S^{\beta\alpha} & S^{\beta\beta} & \dots \\ \vdots & \vdots & \ddots \end{pmatrix}}_{\mathbb{S}} \begin{pmatrix} \mathbf{a}^{\text{in},(\alpha)} \\ \mathbf{a}^{\text{in},(\beta)} \\ \vdots \end{pmatrix}. \quad (1.8)$$

Here the Greek indices ( $\alpha, \beta, \dots$ ) index the spatial channels as before (such as the source and the detector). The vector notation has been introduced to denote the different frequency components associated with each wave amplitude traveling on a given spatial  $\mathbf{a}^{\text{out}(\alpha)} = (a_1^\alpha, a_2^\alpha, \dots, a_i^\alpha, \dots, a_{N_\alpha}^\alpha)$  and  $\mathbf{a}^{\text{out}(\beta)} = (a_1^\beta, a_2^\beta, \dots, a_i^\beta, \dots, a_{N_\beta}^\beta)$ . For such a case, each of the scattering 'elements'  $S^{\alpha\beta}$  become sub-matrices with dimensions,  $N_\alpha \times N_\beta$ , determined by the number of temporal channels associated

with spatial ports  $\alpha$  and  $\beta$  respectively. The scattering description is also closer to many experimental situations where spatial ports are addressed with transmission lines serving as conduits of electromagnetic waves, rather than being connected to voltage or current sources and multimeters. In case the circuit is passive i.e. all input and output waves have the same frequency, then reciprocity leads to a symmetry between off-diagonal scattering amplitudes describing mixing of spatial ports at a given frequency

$$S_{ii}^{\alpha\beta} = S_{ii}^{\beta\alpha}. \quad (1.9)$$

This can be, equivalently, expressed as the condition of full scattering matrix being symmetric

$$\mathbb{S} = \mathbb{S}^T, \quad (1.10)$$

a condition completely analogous to the one in Eq. (1.7). As expected, the condition of reciprocity constrains the scattering matrices quite tightly; for instance, a three-port network cannot be reciprocal, lossless ( $\mathbb{S}$  is unitary or energy conserving) and matched (which means no reflections at the ports  $\mathbb{S}^{\alpha\alpha} = 0 \forall \alpha$ ) simultaneously [Pozar, 2005].

If the circuit can perform mixing of different frequency channels (temporal ports), the off-diagonal scattering elements describing frequency conversion pick up non-symmetric phases (usually equal and opposite) and hence break the reciprocity in phase.<sup>2</sup> Nonetheless, quite remarkably, we still have reciprocity in amplitude between pairs of frequency channels traveling on the same

$$|S_{i,k}^{\alpha\alpha}| = |S_{k,i}^{\alpha\alpha}| \quad (1.11)$$

---

<sup>2</sup>See a detailed discussion in section 1.4.2.

or different spatial ports

$$|S_{i,k}^{\alpha\beta}| = |S_{k,i}^{\beta\alpha}|. \quad (1.12)$$

It should be noted that for active devices performing frequency mixing, we can define a scattering matrix  $\mathbb{S}$  and corresponding reciprocity relationships just as for a passive device, *only* if the  $\mathbb{S}$  matrix is defined in basis of equivalent photon amplitudes  $a_i^{\text{in,out}(\alpha)} = (V \mp Z_\alpha I) / \sqrt{\hbar\omega_i Z_\alpha}$  at participating frequencies (note the important normalization factor  $\sqrt{\omega_i}$ ).

The wide applicability of the reciprocity principle, thus, arises from the fact that the underlying basis of reciprocal response of electromagnetic fields draws from rather simple and general ideas, which elevates it to a status of a *Newton's third law for electromagnetic fields*. The violation of this symmetry therefore requires rather special conditions such as those realized in gyrotropic materials, the subject of our next discussion. It will also provide us with an example of how nonreciprocity in phase can be exploited to achieve nonreciprocity in amplitude transmission.

## 1.2 Nonreciprocity with magnetic fields: Faraday Rotation

Reciprocity is violated by the magneto-optic Faraday effect [Pozar, 2005] — the nonreciprocal rotation of the polarization vector of light that results from different propagation velocities of left- and right-circularly polarized waves in the presence of an applied magnetic field  $\mathbf{H}$  parallel to the direction of propagation. The reason for such a nonreciprocal response is due to the fact that the susceptibility tensor ( $\zeta$ ), namely either the permittivity  $\epsilon$  (gyrotropic) or permeability  $\mu$  (gyromagnetic),

ceases to be symmetric in the presence of a magnetic field.

$$\zeta_{ik}(\mathbf{H}) = \zeta_{ki}^*(-\mathbf{H}) \quad (\zeta = \epsilon \text{ or } \mu). \quad (1.13)$$

For a lossless material, the tensor should be hermitian [Landau and Lifshitz, 1984] but not necessarily real, i.e.  $\zeta_{ik} = \zeta_{ik}^*$ . In conjunction with Eq. (1.13), this gives the condition that in a lossless gyrotropic medium, the real and imaginary parts of the susceptibility tensor are even and odd functions of the applied field respectively. Hence, a typical susceptibility tensor describing such a material is of the form,

$$\begin{bmatrix} B_x \\ B_y \\ B_z \end{bmatrix} = \begin{pmatrix} \mu_1 & i\mu_2 & 0 \\ -i\mu_2 & \mu_1 & 0 \\ 0 & 0 & \mu_3 \end{pmatrix} \begin{bmatrix} H_x \\ H_y \\ H_z \end{bmatrix} \quad (1.14)$$

where  $\mu_2$  reverses sign with the direction of the external field. This form of the permeability tensor is also known as the Polder tensor [Polder, 1949]. We note that the permeability matrix given above is hermitian and positive-definite, i.e.  $\mu_1, \mu_3 > 0$  and  $|\mu_2| < \mu_1$ .

The nonreciprocal phenomenon of Faraday rotation should be contrasted with the superficially similar, though reciprocal, effect of optical activity where the polarization vector of light is rotated on passage through a non-centrosymmetric (chiral) medium. Both of the above are similar in that they rest on the phenomenon of circular birefringence which leads to different phase velocities for left and right circularly polarized light — this difference causes a rotation of plane of polarization of the wave as it propagates through a birefringent material. However, there is a crucial difference between the two: while the rotations in chiral or optically active media are reciprocal, Faraday media perform nonreciprocal rotation of polarization (see Fig. 1.3). For interested readers, Appendix A includes a detailed

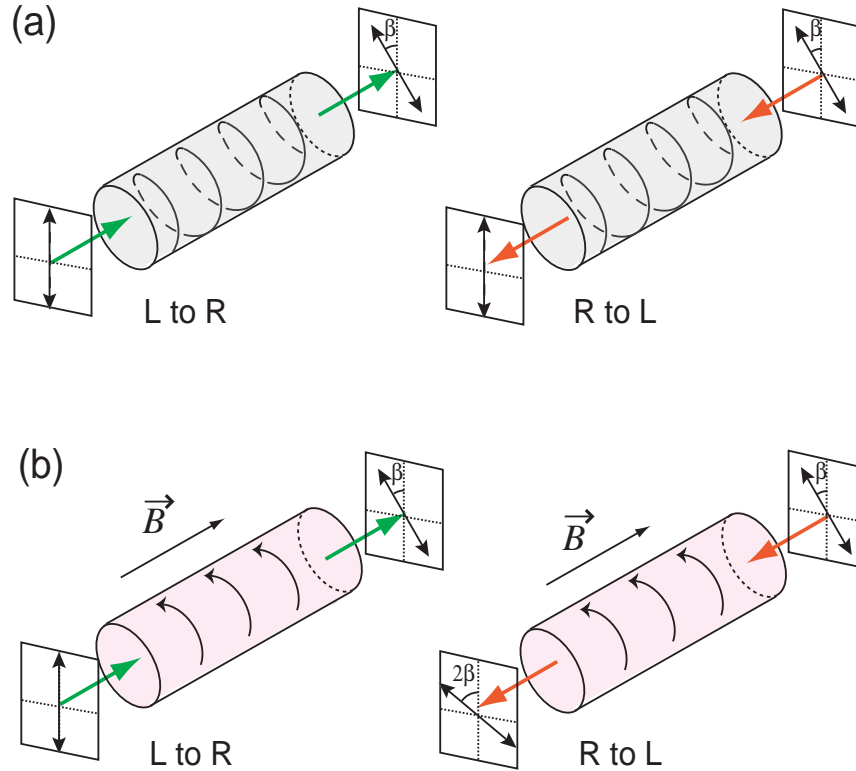
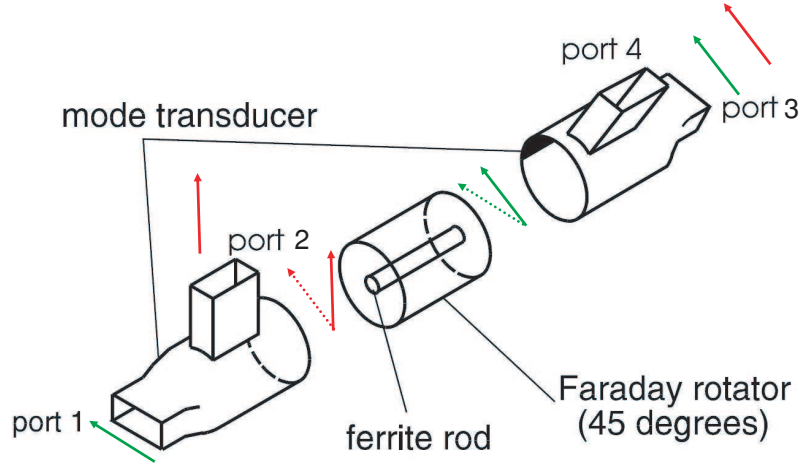


Figure 1.3: **Optical Activity vs Faraday rotation.** (a) Rotation of the polarization vector of light on passage through an optically active medium, recovers on reversing the direction of propagation. This occurs because optical rotation depends on the chirality of the medium (represented as a helix) which also reverses with the direction of propagation. (b) In Faraday rotation, on the other hand, the sense of light rotation as seen with respect to the direction of propagation is different for the two propagation directions, leading to the doubling of the rotation angle on reversing the ray through the medium. This is because the sign of optical rotation is tied to a rotation-like property of the medium (shown by the arrows), set by an external magnetic field that remains fixed for both forward and reverse propagating waves.

discussion of light propagation in the two kinds of birefringent media to explain this difference.

The phenomenon of Faraday rotation is employed in nonreciprocal devices, such as the isolators or circulator, by exploiting the nonreciprocal phase shifts in conjunction with a polarizer-analyzer configuration of the optical devices. The



Source: Philips Semiconductos

Figure 1.4: **Schematic of a ferrite-based circulator.** Conventional circulator design (a waveguide analogue is shown here) using Faraday rotation. The main element is a rod of ferrite, biased using a permanent magnet, and a length appropriate to rotate the phase of the propagating waves by 45 degrees. The green arrows depict the rotation of polarization vector of the wave propagating from left to right. The red arrows show the change in polarization on propagation from right to left. For simplicity of representation the magnetic field vectors are shown for the  $TE_{10}$  mode of the waveguide couplers.

scattering matrix of a device (see Appendix B), such as that shown for the circulator in Fig. 1.3 can be written as:

$$\mathbb{S} = \begin{pmatrix} 0 & 0 & 0 & 1 \\ 0 & 0 & 1 & 0 \\ 1 & 0 & 0 & 0 \\ 0 & 1 & 0 & 0 \end{pmatrix}. \quad (1.15)$$

As seen clearly from the last equation,  $S_{ij} \neq S_{ji} \ i \in \{1, 2, 3, 4\}$  i.e.  $\mathbb{S} \neq \mathbb{S}^T$  and hence the scattering is nonreciprocal. In addition, as the diagonal elements representing reflections at each port are identically zero the device is matched. Further, as the matrix is unitary (i.e.  $\mathbb{S}^\dagger \mathbb{S} = 1$ ) the device is lossless.<sup>3</sup>

<sup>3</sup>In practical devices, there is a minor loss of the order of few tenths of a dB (< 0.2 dB for

### 1.3 Nonreciprocity without magnetic fields

In conventional ferrite-based circulators, the rotation angle for a given material varies proportionally with magnetic fields and the distance light covers in the ferrite. Thus the requirement of large nonreciprocal phase shifts (such as those shown in Fig. 1.4) necessarily translates into either large magnetic fields and/or bulky nonreciprocal components – both of which present a severe handicap to their integration with on-chip superconducting devices. Thus though quite simple to use and hence ubiquitous in their application, there has been active research to find a substitute for Faraday-active media by exploring alternative non-magnetic options that can imitate nonreciprocal transmission characteristics.

Another area which can benefit greatly from on-chip nonreciprocity is low-noise mesoscopic measurements, where one needs to amplify weak signals coming from the sample at low temperatures before they are routed to noisy room temperature electronics. Josephson parametric amplifiers (a.k.a. ‘paramps’) have emerged as a popular choice for such applications as they exploit the non-dissipative nonlinearity of the junction to process and amplify microwave signals with minimum possible noise. However, most paramps are operated in a reflection mode with both the input and output signals collected on the same spatial channel [Castellanos-Beltran and Lehnert, 2007; Yamamoto et al., 2008; Vijay et al., 2009; Bergeal et al., 2010a] and hence are critically dependent on nonreciprocal components for their functionality. Besides making the measurement chain vulnerable to the usual pitfalls accompanying the use of magnetic nonreciprocal devices (losses, bulk), it also places a limitation on multiplexing such set-ups due to increased complexity. This becomes a pragmatic concern when evaluating practical viability of a scaled-up version with multiple qubit-amplifier assemblies.

---

waveguide circulators and 0.3-0.5 dB for microstrip or coax circulators) owing to the losses in ferrite and dielectric material.

One of the most promising realizations of ‘magnet-free’ directionality<sup>4</sup> is the traveling wave parametric amplifier (TWPA). As evident from its name, this device also amplifies signals propagating along a preferred direction that is set by proper phasing of signals desired for a parametric amplification process (not a magnetic field!). Such a device working at microwave frequencies can be panacea for applications such as superconducting qubit readout, alleviating both the isolation and measurement problems simultaneously. There are already examples of such a device in the optical domain, which is the subject of the discussion in next section.

### 1.3.1 Traveling wave parametric amplifiers (TWPA)

The basic design of a TWPA involves nonlinear devices placed periodically along the length of a distributed structure such as a transmission line. Originally proposed for electronic amplifiers at microwave and radiofrequencies in 1961 [Tien, 1961], it was first adapted for optical amplifiers aided by the advent of lasers and optical fibers [Hansryd et al., 2002] [Fig. 1.5(a)] which enabled the high power densities necessary to access nonlinear effects required for parametric amplification. The optical versions of TWPA usually employ a nonlinear dielectric in which the polarization  $p$  has nonlinear dependence on the electric field  $E$  of the form:

$$p = \epsilon_0\chi E + \chi_{NL}E^2, \quad (1.16)$$

where  $\epsilon = \epsilon_0(1 + \chi)$  is the usual linear part of the polarization and  $\chi_{NL}E^2$  represents the nonlinear contribution.

To elucidate the underlying principle, we present here a simplified analysis of parametric wave-mixing in a TWPA<sup>5</sup>, which involves three plane waves of

---

<sup>4</sup>The term *directional* is used in this thesis to describe systems that implement nonreciprocity *with gain* of the transmitted signal. This choice is motivated by parlance in the community where amplifiers exhibiting this property are called directional amplifiers.

frequencies  $\omega_S$ ,  $\omega_I$  and  $\omega_P$  propagating in a nonlinear medium according to the equations

$$E_S(t) = e_S e^{i(\omega_S t - k_S z)} + c.c., \quad (1.17)$$

$$E_I(t) = e_I e^{i(\omega_I t - k_I z)} + c.c., \quad (1.18)$$

$$E_P(t) = e_P e^{i(\omega_P t - k_P z)} + c.c. \quad (1.19)$$

On substituting the instantaneous electric field in the medium  $E(t) = E_S + E_I + E_P$  in Maxwell's equations, we end up with a system of coupled equations of motion of the form [Yariv, 1997]

$$\frac{d\tilde{A}_S}{dz} = -i\kappa \tilde{A}_I^* \tilde{A}_P e^{-i(\Delta k)z}, \quad (1.20a)$$

$$\frac{d\tilde{A}_I^*}{dz} = +i\kappa \tilde{A}_S \tilde{A}_P^* e^{i(\Delta k)z}, \quad (1.20b)$$

$$\frac{d\tilde{A}_P}{dz} = -i\kappa \tilde{A}_S \tilde{A}_I e^{i(\Delta k)z}, \quad (1.20c)$$

where the  $\tilde{A}_k = e_k / \sqrt{\omega_k}$  are square roots of the photon fluxes [dimensions of (power/area)<sup>1/2</sup>] at the respective frequencies and

$$\Delta k = k_P - (k_S + k_I) \quad (1.21)$$

$$\kappa = \chi_{NL} \sqrt{\frac{\mu}{\epsilon_0} \omega_P \omega_S \omega_I}. \quad (1.22)$$

The basic idea now is to amplify a weak signal, say at  $\omega_S$ , by means of frequency conversion of photons from a strong beam at  $\omega_P$  (called the 'pump') into  $\omega_S$  (and

---

<sup>5</sup>A more detailed discussion of parametric systems, with emphasis on realization with Josephson junctions, will be presented in the next chapter

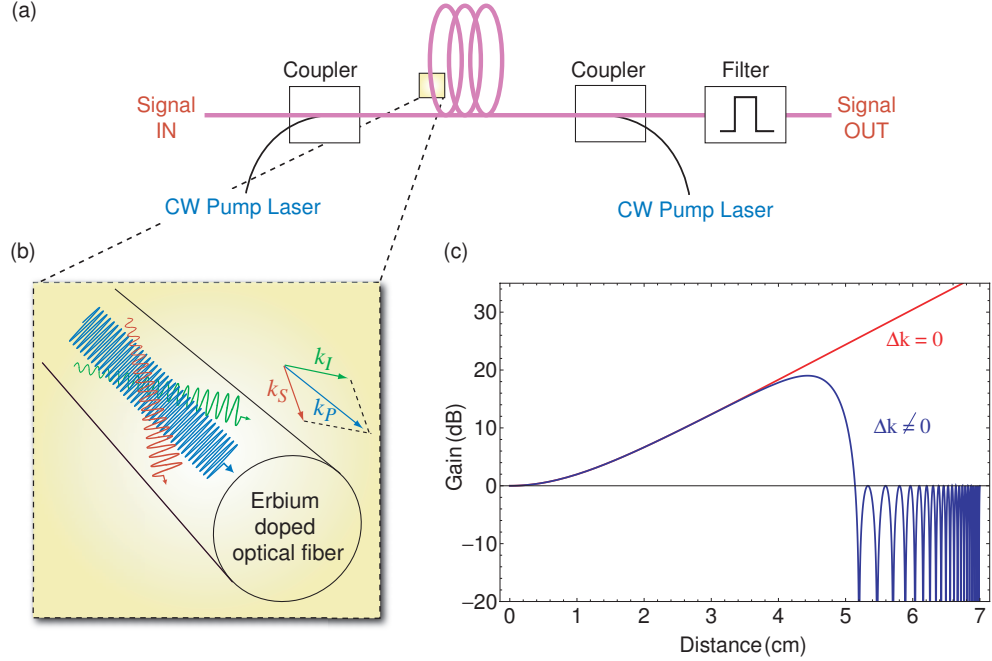


Figure 1.5: **Traveling wave parametric amplifiers (TWPA)**. (a) Schematic of a TWPA based on optical fiber. (b) Parametric three-wave mixing in TWPA between pump (blue), signal (red) and idler waves (green). With proper phase matching ( $\Delta k = 0$ ), as shown by the  $k$  vector diagram in the inset, signal and idler waves are amplified as they travel along the optical fibre. (c) Comparison of signal gain with and without phase matching, as a function of distance traversed along a silica fibre of core diameter  $10 \mu\text{m}$ . The calculation is done assuming the phase mismatch due to Kerr nonlinearity only i.e.  $\Delta k = \Delta n \omega/c$  where  $\Delta n = n_2 \times \text{Intensity}$ , with typical values of nonlinear refractive index  $n_2 = 10^{-14} \text{ cm}^2/\text{watt}$ ) reported for silica fibres.

$\omega_I$  called the idler channel). For this to work correctly, we require

$$\Delta k = 0; \quad (\text{phase matching}) \quad (1.23)$$

$$\omega_P = \omega_S + \omega_I; \quad (\text{frequency matching}). \quad (1.24)$$

On ensuring the above two conditions we get an amplification of photon fluxes at the signal and idler frequencies as they propagate through the medium [see

Fig. 1.5(b)]

$$\begin{aligned}
N_S(z) \propto \tilde{A}_S(z)^* \tilde{A}_S(z) &= |\tilde{A}_S(0)|^2 \cosh^2 \frac{gz}{2} \\
&\xrightarrow{gz \ll 1} \frac{|\tilde{A}_S(0)|^2}{4} e^{gz} \tag{1.25}
\end{aligned}$$

$$\begin{aligned}
N_I(z) \propto \tilde{A}_I(z)^* \tilde{A}_I(z) &= |\tilde{A}_S(0)|^2 \sinh^2 \frac{gz}{2} \\
&\xrightarrow{gz \ll 1} \frac{|\tilde{A}_S(0)|^2}{4} e^{gz} \tag{1.26}
\end{aligned}$$

where  $g = 2\kappa\tilde{A}_P(0)$  and we have assumed no input at the idler frequency  $\tilde{A}_I(0) = 0$ . It should be noted that in writing the above equations, we have assumed a stiff pump ignoring the effect of pump depletion. This essentially involves ignoring the dynamics of the pump described by Eq. (1.20c) and linearizing Eqs. (1.20a) and (1.20b) assuming the pump amplitude  $A_P$  to be constant <sup>6</sup>.

We can see that TWPA has *unilateral* (or directional) gain as it only amplifies signals that are traveling in the direction of the pump — we can see this from Eqs. (1.20a), where if the signal opposes the pump ( $z \rightarrow -z$ ), then following the calculation as outlined above we get exponential deamplification of the signal as energy flows in reverse from the signal to the pump. Besides unilateral amplification, the TWPAs have mainly being exploited for their large operational bandwidths which allow applications such ultra-fast switching and signal addressing, as there are no resonating structures that limit the dynamic bandwidth of the device.

However, one of the major caveats in the version of the traveling-wave amplification discussed above is the assumption of *phase matching* ( $\Delta k = 0$ ). For

---

<sup>6</sup>We will continue to make the approximations of a stiff drive throughout this thesis. The effect of a depleted or ‘soft’ drive can indeed be appreciable as shown in Ref. [Marhic et al., 2001] and like. In the paradigm of driven Josephson parametric amplifiers, we calculated this effect for a double-pump scheme involving four-wave mixing [Kamal et al., 2009]. Such schemes are expected to realize a stiffer pump due to relatively large spectral separation between the signal and the pump.

obtaining sufficient gain with traveling wave schemes, signals need to travel over sufficiently large distances (gain coefficients being  $0.5 - 0.7 \text{ cm}^{-1}$  for typical nonlinear dielectrics). Ensuring a proper phase relationship between the interacting waves of different frequencies over large distances becomes a challenge. This is particularly complicated by the nonlinear ‘Kerr effect’ of the medium Eq. (1.16) which makes the refractive index, and hence phase matching, intensity dependent (since  $k = \omega n(\omega)/c$ ). As the signal propagates in a TWPA, its amplitude increases continuously with distance due to amplification, making it harder to satisfy the condition of phase matching throughout the propagation length. This leads to a significant reduction in the gain coefficient  $g$  of Eqs. (1.25) and (1.26)

$$g \xrightarrow{\Delta k \neq 0} \sqrt{g^2 - (\Delta k)^2}, \quad (1.27)$$

which can be obtained from Eqs. (1.20a)-(1.20c) by including  $\Delta k \neq 0$ . In fact, we see that unless  $g \leq \Delta k$ , the amplification of signal is unsustainable and the photon fluxes at signal and idlers oscillate as functions of the distance as  $\cos[((\Delta k)^2 - g^2)^{1/2}z]$  and  $\sin[((\Delta k)^2 - g^2)^{1/2}z]$  respectively, as shown in Fig. 1.5(c).

In recent years there has been renewed interest in TWPAs based on nonlinear superconducting devices such as Josephson junctions [Tholen et al., 2007; Siddiqi] and high kinetic inductance nanowires [Ho Eom et al., 2012] to achieve wideband operation at microwave frequencies.

## 1.4 Chain of parametric circuits: Discrete TWPAs(!)

The discussion of TWPAs in the last section shows that propagation in parametric systems requires phase matching between the interacting signal and pump waves, thus making this a useful knob to set a preferred direction. This idea can be exploited in a chain of multiple standing-wave parametric devices, such as those

realizable in optical and microwave domains, to realize a discrete version of the TWPA. Very recently, promising experimental efforts [Abdo et al., 2013b] have shown that by employing a chain of discrete “0D” parametric stages (essentially where signal and pump waves interact only at a localized region in space), it is possible to achieve a preferred propagation direction by exploiting a gradient in the phases of the pumps across stages. The electrical version of paramps employing Josephson junctions (JJs) are examples of such “0D” parametric devices, where the JJ acts as a localized nonlinear scatterer for microwaves. In this design, parametric mixing occurs over a much smaller distance as compared to the total distance travelled by the waves. This makes this scheme practically free of phase mismatch between signal and pump waves as the wave mixing occurs in only discrete stages, in contrast to the continuous mixing in distributed TWPA schemes. The following section presents a brief review of basic equations governing wave mixing in Josephson parametric devices and two practical strategies employing JJs as a mixer.

### **1.4.1 Josephson parametric circuits**

The phrase ‘parametric system’ refers to any generic system whose operation depends upon the time variation of a characteristic parameter. This parameter can be either be the bob-axis distance in a swinging pendulum, or a time-varying reactance (inductance/capacitance) in a circuit. For microwave parametric circuits, the workhorse is the superconducting Josephson tunnel junction (JJ). A JJ consists of a superconductor-insulator-superconductor sandwich and forms the only known nonlinear non-dissipative circuit element working at microwave frequencies. It has a current phase relationship of the form (also known as the first Joseph-

son relation)

$$J = I_0 \sin \varphi, \quad (1.28)$$

where  $J$  denotes the supercurrent flowing through the junction,  $\varphi = 2\pi\Phi/\Phi_0$  represents the gauge-invariant phase difference between the superconducting electrodes (corresponding to a flux  $\Phi = \int_{-\infty}^t V(t')dt'$  across the junction) and  $I_0$  is the critical current of the junction or the maximum possible zero voltage current that can be passed through the JJ.<sup>7</sup> The usual way to achieve parametric operation is to vary the flux  $\Phi$  associated with the junction through a time-dependent external stimuli such as an rf voltage or current. In such a picture, we can establish the equivalence of this kind of nonlinear response with a parametric system by differentiating Eq. (1.28)

$$\frac{dJ}{dt} = \frac{2\pi I_0 \cos \varphi(t)}{\Phi_0} V(t). \quad (1.29)$$

Here  $V = \dot{\Phi}$  is the voltage across the junction, and we identify a junction inductance

$$L_J = \frac{\Phi_0}{2\pi I_0 \cos \varphi(t)}. \quad (1.30)$$

The Josephson junction can thus be thought of as a parametric (time-varying) inductor whose value can be controlled by an associated time-dependent voltage (and hence flux)

$$V(t) = V_{dc} + V_{RF} \cos(\omega t + \theta). \quad (1.31)$$

---

<sup>7</sup> $I_0$  is a characteristic parameter set during the junction fabrication by controlling the area and the thickness of the insulating layer.

Here  $V_{dc} = \langle \dot{\Phi} \rangle$  denotes the dc voltage associated with the junction.

Another useful way to parameterize a junction is to calculate the energy  $U$  stored in the junction as

$$\begin{aligned}
 U &= \int_t V(t') J(t') dt' \\
 &= \frac{\Phi_0 I_0}{2\pi} \int \dot{\varphi}(t') \sin \varphi dt' \\
 &= -E_J \int_0^\varphi \sin \varphi d\varphi \\
 &= -E_J (1 - \cos \varphi),
 \end{aligned} \tag{1.32}$$

which shows that unlike a linear inductor which has a quadratic relationship between energy and flux, the Josephson energy has a cosine dependence on flux<sup>8</sup> with the depth of each cosine well being  $2E_J$ .

## 1.4.2 Minimal model for parametric wave mixing

In this section we will consider how a parametric circuit such as that based on a JJ can perform frequency mixing or conversion. The idea is completely analogous to the three wave mixing introduced in the context of TWPAs in section 1.3.1 but now instead of a distributed medium we will employ a parametric reactance (like the Josephson inductance) to achieve the wave mixing. The circuit schematic, conducive for a scattering analysis of such a process, is shown in Fig. 1.6. The minimal system describing frequency conversion comprises two parametrically coupled oscillators  $A$  and  $B$  with a low frequency ( $\omega_m$ ) signal coupled to port  $A$  and high frequency sidebands coupled to port  $B$ . The dynamics of the system can

---

<sup>8</sup>It is important to note that the dimensionless flux (or phase) associated with a junction as  $\varphi(t) = \Phi(t)/\varphi_0 = \varphi_0^{-1} \int_{-\infty}^t V(t') dt'$  is actually a gauge-invariant quantity, unlike the flux associated with a conventional inductor  $\Phi = \int_{area} d\mathbf{a} \cdot \mathbf{B}$ .

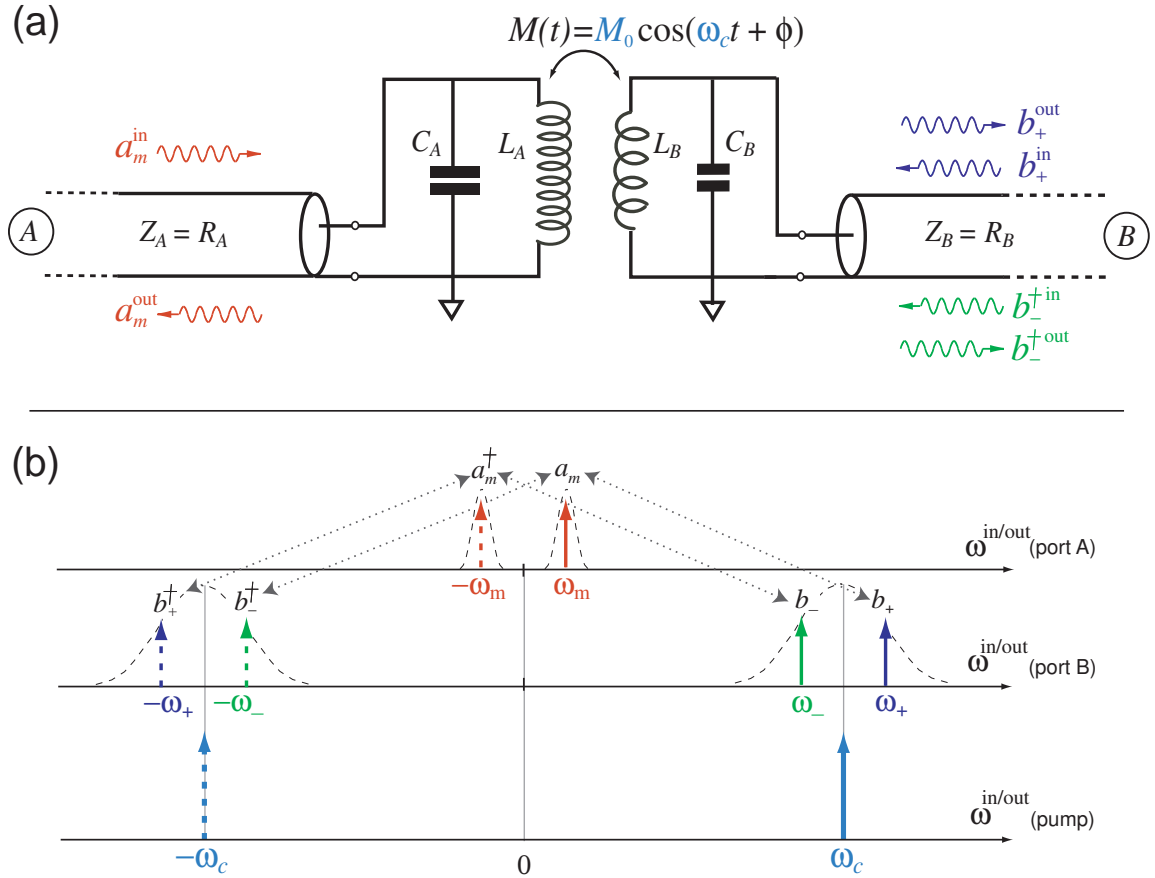


Figure 1.6: **Minimal model for a parametric three-wave mixer.** (a) Circuit schematic for a parametric circuit performing reversible frequency conversion. The resonance lineshapes of the two spatially distinct channels  $A$  and  $B$  are centered at  $\omega_{A,B} = 1/\sqrt{L_{A,B}C_{A,B}}$ . The incoming and outgoing signals at modulating frequency  $\omega_m = \omega_A$  travel on channel  $A$ . The two sidebands at  $\omega_{\pm}$  are detuned by equal amounts from the carrier at  $\omega_c$  and travel on channel  $B$ . The parametric element is represented by the time-varying mutual inductance which is varied sinusoidally at the carrier frequency  $\omega_c = \omega_B - \omega_A$ . (b) Spectral density/response landscape for various channels in three-wave mixing. The dotted lines represent the couplings between different channels. The solid and the dashed arrows represent different frequencies and respective conjugates.

be described by coupled equations of the form:

$$C_A \ddot{\Phi}^A(t) + \frac{\dot{\Phi}^A(t)}{R_A} + \frac{\Phi^A(t)}{L_A} + \frac{\Phi^B(t)}{M} \cos(\omega_c t + \phi) = I_{RF}^A(t) \quad (1.33a)$$

$$C_B \ddot{\Phi}^B(t) + \frac{\dot{\Phi}^B(t)}{R_B} + \frac{\Phi^B(t)}{L_B} + \frac{\Phi^A(t)}{M} \cos(\omega_c t + \phi) = I_{RF}^B(t), \quad (1.33b)$$

where the variables  $\Phi^{A,B}$  denote the node fluxes associated with each of the oscillators. The parametric coupling is achieved by a time-dependent mutual inductance<sup>9</sup> of the form identical to that realized using Josephson inductance Eq. (1.30)

$$M(t)^{-1} = M_0^{-1} \cos(\omega_c t + \phi). \quad (1.34)$$

On expressing Eqs. (1.33) in the frequency domain and ignoring the rapidly rotating terms (rotating wave approximation), we obtain a linearly coupled system of equations for the mode fluxes oscillating at the signal ( $\Phi_m^A$ ), upper sideband ( $\Phi_+^B$ ) and lower sideband ( $\Phi_-^{B*}$ ) frequencies

$$(\delta_m + i)\Phi_m^A + \frac{L_A}{M}(\Phi_+^B e^{-i\phi} + \Phi_-^{B*} e^{i\phi}) = \frac{2V_m^{\text{in}}}{\omega_A} \quad (1.35a)$$

$$(\delta_{\pm} + i)\Phi_{\pm}^B + \frac{L_B}{M}\Phi_m^A e^{i\phi} = \frac{2V_{\pm}^{\text{in}}}{\omega_B} \quad (1.35b)$$

$$(-\delta_{\pm} - i)\Phi_{\pm}^{B*} + \frac{L_B}{M}\Phi_m^A e^{-i\phi} = \frac{2V_{\pm}^{\text{in}}}{\omega_B} \quad (1.35c)$$

where we have expressed the input rf drives as propagating waves on respective transmission lines. Following the notation introduced in section 1.1, the superscripts index the spatial channels and the subscripts are a short-hand for the

---

<sup>9</sup>We discuss how to actually realize such an inductance using JJ circuits in section 1.5.

respective frequency (temporal channel). Here

$$\begin{aligned}\delta_m &= \frac{|\omega_m - \omega_A|}{\Gamma_A}; & \Gamma_A &= \frac{1}{2Z_A C_A} \\ \delta_{\pm} &= \frac{|\omega_{\pm} - \omega_B|}{\Gamma_B}; & \Gamma_B &= \frac{1}{2Z_B C_B}.\end{aligned}$$

It is instructive to note that Eqs. (1.35) share the same structure as Eqs. (1.20c) discussed for describing signal-idler coupling in a TWPA. The major difference is that for frequency conversion the external drive is at the carrier frequency  $\omega_c = \omega_B - \omega_A$  equal to the difference between the signal and idler resonator frequencies, while for amplification it is at the pump frequency  $\omega_P = \omega_S + \omega_I$  equal to the sum frequency of the signal and idler. On using the input-output relations

$$V^{\text{out}}[\omega] = i\omega\Phi[\omega] - V^{\text{in}}[\omega] \quad (1.36)$$

and expressing input voltages in terms of normalized photon fluxes  $a_i^{\text{in/out}} = V^{\text{in/out}}/\sqrt{2\hbar\omega_i R_i}$ , we obtain the following relationship between different incoming and outgoing signals

$$\begin{pmatrix} a_m^{\text{out}} \\ b_+^{\text{out}} \\ b_-^{\dagger,\text{out}} \end{pmatrix} = \begin{pmatrix} r_m & t_d e^{-i\phi} & s_d e^{i\phi} \\ t_u e^{i\phi} & r_+ & v e^{2i\phi} \\ -s_u e^{-i\phi} & -v e^{-2i\phi} & r_- \end{pmatrix} \begin{pmatrix} a_m^{\text{in}} \\ b_+^{\text{in}} \\ b_-^{\dagger,\text{in}} \end{pmatrix} \quad (1.37)$$

where we have suppressed the superscripts for brevity.<sup>10</sup> Here

$$r_m = -\frac{(\delta_m - i)}{(\delta_m + i)} \quad (1.38a)$$

$$r_+ = \frac{(\delta_m + i)(\delta_{\pm}^2 + 1) - 2i\alpha^2}{(\delta_m + i)(\delta_{\pm} + i)^2} \quad (1.38b)$$

$$r_- = \frac{(\delta_m + i)(\delta_{\pm}^2 + 1) + 2i\alpha^2}{(\delta_m + i)(\delta_{\pm} + i)^2} \quad (1.38c)$$

$$t_u = t_d = \frac{2i\alpha}{(\delta_m + i)(\delta_{\pm} + i)} \quad (1.38d)$$

$$s_u = s_d = \frac{2i\alpha}{(\delta_m + i)(\delta_{\pm} + i)} \quad (1.38e)$$

$$v = \frac{-2i\alpha^2}{(\delta_m + i)(\delta_{\pm} + i)^2} \quad (1.38f)$$

with  $\alpha^{-1} = M_0/\sqrt{L_A L_B}$ . It becomes immediately evident by looking at the off-diagonal elements of the  $\mathbb{S}$ -matrix that though the net up- and down-converted amplitudes are equal, they pick up equal and opposite phases determined by the pump phase  $\phi$ .

To further elucidate the rotation of signals in the quadrature plane with the pump phase, we present two equivalent representations of the sidebands in a frame rotating with the pump, as shown in Fig. 1.7. In the first representation, the each phasor is represented as a vector rotating at an angular frequency  $\omega_m$  in the complex plane. In the second representation, we identify them with two quadratures defined in the  $I - Q$  plane as

$$I = \text{Re}[b_+ + b_-^*] \quad (1.39a)$$

$$Q = \text{Im}[b_+ - b_-^*]. \quad (1.39b)$$

Figure 1.7(b) shows a plot of these quadratures, calculated using the expressions in Eq. (1.37). We see that the resultant signal represented as a modulation ellipse

---

<sup>10</sup>The fact that different frequency components are traveling on different spatial channels is not crucial to the following discussion.

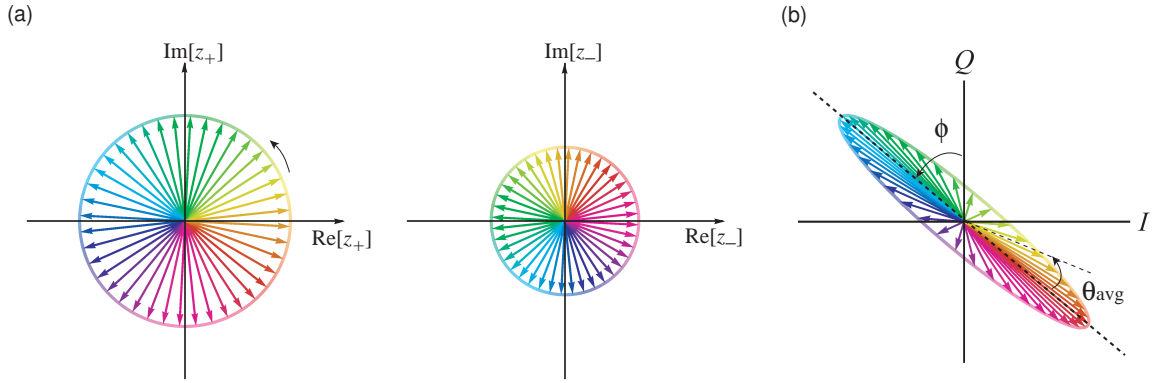


Figure 1.7: **Different representations of a modulated signal.** (a) Complex-plane representation of sidebands as phasors  $z_{\pm} = |b_{\pm}|e^{i(\omega_m t + \theta_{\pm})}$  in a frame rotating at the carrier frequency  $\omega_c$ . The amplitudes  $|b_{\pm}|$  are encoded as the radius of the circle. The time progression of rotation as  $e^{i\omega_m t}$  is shown as colored arrows with yellow denoting the phases  $\theta_{\pm}$  at time  $t = 0$ . (b) The combined representation given in Eq. (1.39) encodes the four real numbers associated with the two complex phasors as four distinct properties of a modulation ellipse: (i) length of the semi-major axis ( $|b_+| + |b_-|$ ), (ii) length of the semi-minor axis ( $|b_+| - |b_-|$ ), (iii) tilt of the ellipse,  $(\theta_+ - \theta_-)/2$  and (iv) average phase at  $t=0$ ,  $\theta_{\text{avg}} = (\theta_+ + \theta_-)/2$  (shown by the position of yellow along the ellipse with respect to semi-major axis). The vector sum of the two phasors is constrained to move along this ellipse at all times. As seen from Eq. (1.37), the tilt angle is equal to the pump phase  $\phi$  in the parametric mixing scheme.

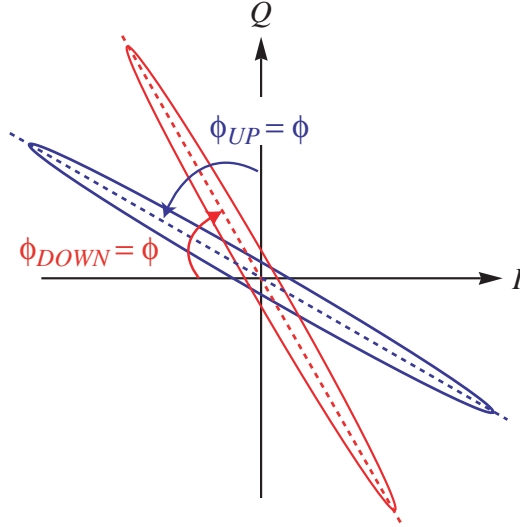


Figure 1.8: **Phase-sensitive nature of parametric up- and downconversion.** Resultant signals after parametric upconversion (blue) and parametric downconversion (red), described by Eq. (1.37). Different phases are obtained for upconverted and downconverted signals generated using the same pump with phase  $\phi$ .

has a tilt solely determined by the phase angle  $\phi$  of the pump. This is closely analogous to the rotation of polarization of a linearly polarized light wave in Faraday rotation, if we identify the phasors  $b_+$  and  $b_-$  as right and left circularly polarized components of modulated signal (see Fig. A.1 in Appendix A). Furthermore, while in the upconversion case we get a polarization by  $\phi$  about the  $Q$  axis [‘blue’ block of Eq. (1.37)], in the downconversion case we get a polarization  $\phi$  about the  $I$  axis [‘red’ block of Eq. (1.37)].

The phase-sensitive nature of these parametric ‘rotations’ forms the crux of the ideas presented in the following chapters:

- in chapter 3, we first show how chaining together two such parametric stages with phase nonreciprocity realizes amplitude nonreciprocity in spatial channels
- in chapter 4, we show how in the presence of higher-order mixing with pump harmonics, parametric rotations can lead to amplitude nonreciprocity

in temporal channels and break the symmetry of frequency conversion.

- in chapter 5, the combination of spatial and temporal nonreciprocity will help us explain directional amplification in SQUID amplifiers

### Comment on symmetries of the scattering matrix

In this annotation to section 1.4.2, we comment on the various symmetries associated with the scattering matrix derived in Eq. (1.37).

#### 1. Unitarity (conservation of energy and information)

The condition of unitarity is usually expressed as the scattering matrix obeying  $\mathbb{S}^\dagger \mathbb{S} = 1$ . It can also be formulated for the full  $2N \times 2N$  scattering matrix  $\tilde{\mathbb{S}}$  describing the device operation for all modes and their conjugates

$$\begin{pmatrix} a_i^{\text{out}} \\ a_i^{\dagger \text{out}} \\ \vdots \\ a_{2N}^{\text{out}} \\ a_{2N}^{\dagger \text{out}} \end{pmatrix} = \underbrace{\begin{pmatrix} s_{ii} & 0 & \dots & 0 & s_{i,2N} \\ 0 & s_{ii}^* & \dots & s_{1,2N}^* & 0 \\ \vdots & \vdots & \ddots & \vdots & \vdots \\ 0 & s_{2N,i}^* & \dots & s_{2N,2N}^* & 0 \\ s_{2N,i} & 0 & \dots & 0 & s_{2N,2N} \end{pmatrix}}_{\tilde{\mathbb{S}}} \begin{pmatrix} a_1^{\text{in}} \\ a_1^{\dagger \text{in}} \\ \vdots \\ a_{2N}^{\text{in}} \\ a_{2N}^{\dagger \text{in}} \end{pmatrix}. \quad (1.40)$$

as

$$\tilde{\mathbb{S}}^T \mathbb{K} \tilde{\mathbb{S}} = \mathbb{K}, \quad (1.41)$$

where  $\mathbb{K} = i\sigma_X \otimes U_N$  where  $U_N$  denotes unit matrix of dimension  $N$ . We note that the matrix obtained in Eq. (1.37) is non-unitary, that is  $\mathbb{S}^\dagger \mathbb{S} \neq 1$ , which implies non-conservation of photon number as is natural for an active device with an external energy source ('carrier' here). This is in agreement with the observation that it recovers its unitary form as we turn off the coupling  $M_0$

responsible for energy transfer between the pump and the signal modes.

## 2. *Symplecticity* (conservation of information alone)

The full  $2N \times 2N$  scattering matrix  $\tilde{\mathbb{S}}$

$$\begin{pmatrix} a_i^{\text{out}} \\ a_i^{\dagger\text{out}} \\ \vdots \\ a_{2N}^{\text{out}} \\ a_{2N}^{\dagger\text{out}} \end{pmatrix} = \underbrace{\begin{pmatrix} s_{ii} & 0 & \dots & 0 & s_{i,2N} \\ 0 & s_{ii}^* & \dots & s_{1,2N}^* & 0 \\ \vdots & \vdots & \ddots & \vdots & \vdots \\ 0 & s_{2N,i}^* & \dots & s_{2N,2N}^* & 0 \\ s_{2N,i} & 0 & \dots & 0 & s_{2N,2N} \end{pmatrix}}_{\tilde{\mathbb{S}}} \begin{pmatrix} a_1^{\text{in}} \\ a_1^{\dagger\text{in}} \\ \vdots \\ a_{2N}^{\text{in}} \\ a_{2N}^{\dagger\text{in}} \end{pmatrix}. \quad (1.42)$$

describing the device operation for all modes is *symplectic*<sup>11</sup> i.e.

$$\tilde{\mathbb{S}}^T \mathbb{J} \tilde{\mathbb{S}} = \mathbb{J}, \quad (1.43)$$

where  $\mathbb{J} = i\sigma_Y \otimes \mathbb{U}_N$  represents a symplectic structure defined on the  $2N \times 2N$  phase space ( $N =$  number of degrees of freedom). Symplecticity can also be expressed by the following constraint on the rows of the scattering matrix

$$\sum_{j=1}^{2N} (-1)^{j-1} |s_{ij}|^2 = 1. \quad (1.44)$$

The condition of *symplecticity* ensures the absence of any extraneous degrees of freedom. It follows from the fact that a transformation of the modes as performed by the scattering matrix needs to be a canonical transformation which preserves the phase space volume and hence *information*. The condition of no missing information [Clerk et al., 2003] or information preservation is a crucial condition for achieving ultimate limits of system performance constrained solely by laws of quantum mechanics (quantum-limited

operation) [Clerk et al., 2010].

The condition of symplecticity has a deep analogy in quantum mechanics: this translation is easily made by identifying that photon fluxes ( $a^{\text{in},\dagger}[\omega]$ ,  $a^{\text{in}}[\omega]$ ) are nothing but the bosonic creation and annihilation operators [Yurke, 2004]. Symplecticity expressed in this language leads to preservation of quantum mechanical commutation relations for the input and output photon operators (see Appendix B for details)

$$[a^{\alpha,\text{in/out}}[\omega_i], a^{\dagger,\beta,\text{in/out}}[\omega_j]] = \delta^{\alpha\beta} \delta(\omega_i + \omega_j). \quad (1.45)$$

Thus, symplecticity is a more general symmetry than unitarity as it applies to both active and passive devices.

## 1.5 Implementations of JJ-based frequency mixers

In this section we discuss two practical strategies to use Josephson junction devices as frequency converters; the first involves frequency mixing using a single voltage-biased JJ while the second is based a novel device known as the Josephson ring modulator.

### 1.5.1 dc-biased single Josephson junction mixer

The use of Josephson junction as a mixer is an extensively investigated idea both experimentally and theoretically. Here we present a brief synopsis of the fundamental concepts required for understanding frequency conversion using a single JJ; we refer interested readers to reviews for details on this subject. The basic idea involves irradiation of a JJ with rf signals, very similar to that introduced in section 1.4.2. The main difference, however, is that unlike the case for parametric

---

<sup>11</sup>An immediate consequence is *unimodularity* i.e.  $\det(\tilde{\mathbb{S}}) = 1$

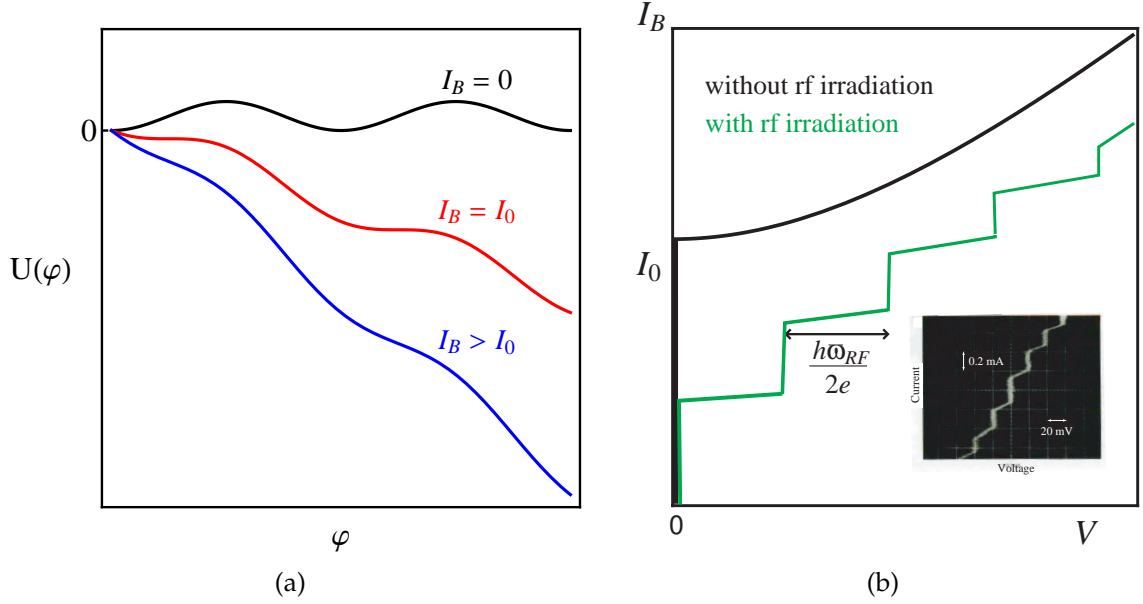


Figure 1.9: **Josephson junction in running/voltage regime.** (a) Josephson potential for different values of a bias current. For  $I_B > I_0$ . (b) DC current-voltage characteristics of a junction biased in the voltage state with and without rf drive. In the presence of an rf drive, constant voltage steps appear due to locking of the motion of the phase  $\varphi$  with external drive. The inset shows the demonstration by S. Shapiro for a JJ irradiated with an RF tone of 9.75 GHz (from Physics Today, Oct 1969, pp. 45).

frequency conversion involving only an RF bias, the junction is now biased with a constant dc voltage  $V_{dc}$  or equivalently a dc current bias  $I_B > I_0$ . This tilts the Josephson cosine potential [Eq. (1.32)], leading to a potential profile known as a *washboard* potential [Fig. 1.9(a)]. The phase excursions in such a junction are not limited to a single well of the Josephson cosine potential and the junction phase ‘runs’ across many wells of the washboard

$$\varphi(t) = \phi_0 + \frac{2eV_{dc}}{\hbar}t, \quad (1.46)$$

where  $V_{dc}$  is the constant voltage impressed across the junction. Using this equa-

tion in Eq. (1.28) gives a supercurrent component oscillating at frequency

$$\omega_J \equiv 2eV_{dc}/\hbar = V_{dc}/\varphi_0, \quad (1.47)$$

where  $\varphi_0 = 2e/\hbar = \Phi_0/2\pi$  represents the reduced flux quantum. Eq. (1.47) is known as the a.c. (or second) Josephson relation and the oscillation frequency  $\omega_J$  is called the Josephson frequency. For performing frequency mixing with a JJ, either the internally generated Josephson oscillation at  $\omega_J$  or an external rf drive can be employed as the pump. We present the mixing equations for the most general case here by writing down the full expression for junction current in the presence of the Josephson frequency and rf drives for both an external carrier of frequency  $\omega_c$  and a modulating signal of frequency  $\omega_m$ ,

$$\frac{J}{I_0} = \sin[\omega_J t + \phi_0 + \frac{V_m}{\varphi_0 \omega_m} \cos(\omega_m t) + \frac{V_c}{\varphi_0 \omega_c} \cos(\omega_c t)], \quad (1.48)$$

where  $V_c$  and  $V_m$  represent the respective amplitudes of rf voltages. This gives<sup>12</sup>

$$\frac{J}{I_0} = \sum_{k=-\infty}^{\infty} \sum_{l=-\infty}^{\infty} J_k \left( \frac{V_m}{\varphi_0 \omega_m} \right) J_l \left( \frac{V_c}{\varphi_0 \omega_c} \right) \sin[(\omega_J + k\omega_m + l\omega_c)t + \phi_0] \quad (1.49)$$

where  $k$  and  $l$  are integers, and we have used the trigonometric identities

$$\begin{aligned} \cos(X \sin \theta) &= \sum_{n=-\infty}^{\infty} J_n(X) \cos(n\theta) \\ \sin(X \sin \theta) &= \sum_{n=-\infty}^{\infty} J_n(X) \sin(n\theta). \end{aligned}$$

---

<sup>12</sup>The more realistic scenario is to use current bias  $I_B > I_0$  as for a zero resistance device such as JJ the current is fixed by an external resistor in the circuit [Henry et al., 1981]. Similarly, in the rf case the drive is never an ideal voltage bias but is closer to a current drive for both rf as well as dc. In such a case, numerical calculations are required to attain step widths and an analytical closed-form solution such as that given is available only for the voltage-biased JJ case. [Tinkham, 1996]

Here  $J_n$ 's represent Bessel functions of order  $n$  and determine the amplitude of different frequency components of the supercurrent. Eq. (1.49) predicts the appearance of current steps at constant voltage, known as *Shapiro steps* [Shapiro, 1963], for definite values of frequencies which lead to a cancellation of the oscillating part in the argument of sine and give a dc contribution to the supercurrent. The currents steps at  $\omega_J = k\omega_m$  and  $\omega_J = l\omega_c$ , correspond to a single applied rf signal [Fig. 1.9(b)]. However, we also get steps for voltage corresponding to  $\omega_J = k\omega_m \pm m\Delta\omega$  and  $\omega_J = l\omega_c \pm m\Delta\omega$  where  $\Delta\omega = \omega_{\pm} = |\omega_c \pm \omega_m|$  ( $m$  is an integer). These additional steps form a series spaced by the difference frequency  $\omega_{\pm}$  at each of the regular Shapiro steps (for  $\omega_m \ll \omega_c$ ). The presence of such steps in the dc characteristics of JJ is signature of three-wave mixing performed by the junction.

### Limitations of Josephson mixers

It has been known that biasing the junction on a Shapiro step results in large excess noise in conversion leading to unstable device behavior. This is attributed to the rather large dynamic resistance of the device biased on a Shapiro step and subsequent broadening of the Josephson oscillation playing the role of the carrier (see Refs. [Schoelkopf] and [Likharev, 1996] and references therein for a comprehensive discussion). One of the strategies to overcome this problem is using magnetic fields to suppress Cooper pair tunneling and realize an SIS quasiparticle mixer which take advantage of the strong quasiparticle nonlinearity of JJs along with an external carrier. The analysis is similar to that presented in the last section with a few differences: the current steps now occur at voltages  $n\hbar\omega_{rf}/e$  due to quasiparticle tunneling (*Dayem-Martin steps*), and hence have twice the voltage spacing as compared to Shapiro steps. Also, their sharpness is defined by the sharpness of the superconducting energy gap. An excellent review of SIS mixers can be found

in Refs. [Tucker, 1979; Tucker and Feldman, 1985].

In the following section, we discuss an alternate strategy involving a novel JJ-based frequency converter operated in the zero-voltage regime of the junction. The unique feature of this device is its implementation of the minimal three-wave mixing described in section 1.4.2, unlike the single JJ mixers which essentially involve the full  $\sin \varphi$  nonlinearity of the junction and hence have a complicated frequency landscape, in general.

### 1.5.2 Josephson parametric converter (JPC)

In this section, we describe an alternative system for implementing parametric frequency conversion using JJs in zero voltage stage. The heart of the system is Josephson ring modulator (JRM) consisting of four Josephson junctions, each with critical current  $I_0 = \frac{\hbar}{2eL_J}$  forming a ring threaded by a flux  $\Phi = \Phi_0/2$  where  $\Phi_0$  is the flux quantum (see Fig. 1.10). The device has the symmetry of a Wheatstone bridge and behaves as a dissipationless nonlinear mixer for the microwaves. If the requirements of frequency matching and phasing are met for the input waves, then this circuit is capable of showing interesting effects like parametric amplification, upconversion and downconversion [Bergeal et al., 2010b,a; Abdo et al., 2013a].

The device dynamics are best described in its eigenbasis. The three spatial eigenmodes of the system correspond to currents

$$I^X = \frac{-I^{(1)} + I^{(3)}}{\sqrt{2}}, \quad (1.50a)$$

$$I^Y = \frac{-I^{(2)} + I^{(4)}}{\sqrt{2}}, \quad (1.50b)$$

$$I^Z = \frac{-I^{(1)} + I^{(2)} - I^{(3)} + I^{(4)}}{2} \quad (1.50c)$$

flowing in three external inductances  $L_X$ ,  $L_Y$  and  $L_Z$  that are much larger than

the junction inductance  $L_J = \varphi_0^2 E_J^{-1}$ . We refer the interested reader to Appendix D for a simple and fun calculation of these modes. Each junction  $j \in \{\alpha, \beta, \gamma, \delta\}$

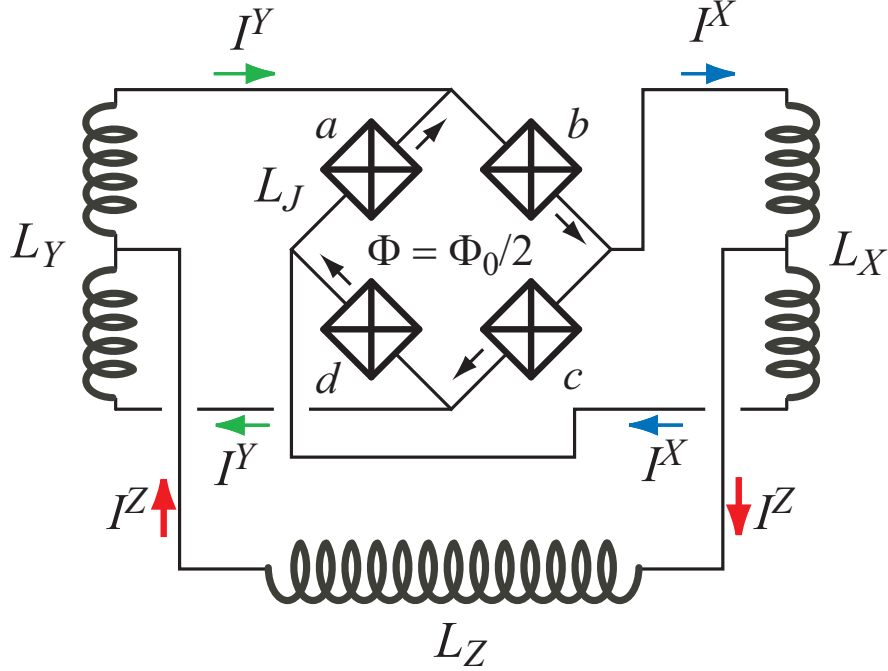


Figure 1.10: **Circuit schematic of a Josephson ring modulator (JRM).** Three-wave mixing element consisting of a loop of four nominally identical Josephson junctions threaded by a flux in the vicinity of half a flux quantum. Mutual inductances, not shown here, couple this circuit to inductances  $L_A$ ,  $L_B$  and  $L_C$  of three external oscillators via the inductances  $L_X$ ,  $L_Y$  and  $L_Z$  respectively, which are much larger than the junction inductance  $L_J$ . The three currents  $I^X$ ,  $I^Y$  and  $I^Z$  correspond to the three orthogonal modes of the structure.

is traversed by a current  $I^j$  and at the working point (i.e.  $\Phi = \Phi_0/2$ ) we express its energy as  $E^j = E_J(\Phi/4)[1 - \sqrt{1 - (I^j/I_0)^2}]$ . Expanding up to fourth order in current and using the effective junction parameters at the given flux bias  $L_J^{\text{eff}} = \sqrt{2}L_J$  and  $I_0' = I_0/\sqrt{2}$ , we obtain [Abdo et al., 2013a]

$$E^j = \frac{1}{2}L_J^{\text{eff}} I^{j,2} - \frac{1}{24} \frac{L_J^{\text{eff}}}{I_0'^2} I^{j,4}, \quad (1.51)$$

where we have used the relation  $E_J(\Phi_0/8) = L_J^{\text{eff}} I_0'^2$  for a single junction. The cur-

rents in the junctions can be expressed in terms of eigenmode currents [Eq. (1.50)]

$$I^a = \frac{I^X - I^Y}{\sqrt{2}} + I^Z + I_\Phi, \quad (1.52a)$$

$$I^b = \frac{I^X + I^Y}{\sqrt{2}} - I^Z + I_\Phi, \quad (1.52b)$$

$$I^c = \frac{-I^X + I^Y}{\sqrt{2}} + I^Z + I_\Phi, \quad (1.52c)$$

$$I^d = \frac{-I^X - I^Y}{\sqrt{2}} - I^Z + I_\Phi, \quad (1.52d)$$

where  $I_\Phi$  is the supercurrent induced in the ring by the externally applied flux  $\Phi$ . On using Eq. (1.52) in the expression of the total energy of the ring Eq. (1.51) and keeping terms up to third order in the currents, we obtain

$$E_{JRM} = \frac{1}{2} L_J^{eff} \left[ (I^X)^2 + (I^Y)^2 + \frac{1}{4} (I^Z)^2 \right] - 2 \frac{L_J^{eff} I_\Phi}{I_0^2} I^X I^Y I^Z. \quad (1.53)$$

We can express the currents as

$$I^{X,Y,Z} = \frac{\Phi_{a,b,c}}{L_{a,b,c}} \frac{M_{a,b,c}}{L_{X,Y,Z}} = \frac{\Phi_{a,b,c}}{L_{a,b,c}^{eff}}, \quad (1.54)$$

where  $M_{a,b,c}$  are the mutual inductances between  $L_{X,Y,Z}$  and the oscillator inductances  $L_{a,b,c}$ . It becomes evident from Eq. (1.53) that the only third order mixing term is of the form  $I^X I^Y I^Z$ . For parametric operation, the  $Z$  mode is usually employed as the pump or carrier in amplification and frequency conversion respectively. It is now straightforward to see that on identifying the associated fluxes  $\Phi^{X,Y,Z} = L_{X,Y,Z} I^{X,Y,Z}$  and using Eq. (1.53) to write down equations of motion will lead to a parametric coupling term identical to that in Eq. (1.33).

The realization of a pure third order nonlinearity allows the JRM to perform minimal three-wave mixing, without producing spurious modulation products.

This condition is essential for information preservation, giving the JRM a powerful advantage for quantum information processing applications such as qubit readout. It is also important for stability of the JRM operated as a mixer, as presence of third order terms such as  $(I^X)^3$ ,  $(I^Y)^3$ ,  $(I^X)^2 I^Z$ ,  $(I^Y)^2 I^Z$  would lead to an undesirable change in mode frequencies with signal and pump powers.

---

# Active Circulator: Nonreciprocity without gain

---

*“Mother, may I go and maffick,  
Tear around and hinder traffic?”*

– H. H. Munro (from *The Complete Saki*)

Some of the most crucial components in any microwave measurement chain are the passive nonreciprocal elements like circulators and isolators, which are used to protect the samples from the noise breathed down by higher temperature stages such as the cryogenic HEMTs (high electronic mobility transistors). A large variety of qubit-readout protocols also involve reflectometric measurements and rely on circulators and isolators for separation of input and output channels [Wallraff et al., 2004; Mallet et al., 2009] introduced in the section A.2. In this chapter, we present the full analysis of a model for a four-port circulator based on parametric active devices with no magnetic components. In active devices the energy source – provided by the pump – acts as the external “bias” field and sets the reference phase for the system, in analogy with the role played by the magnetic field in a Faraday medium. We exploit this effect in a two-stage chain of active devices with pump phases at each stage shifted appropriately to obtain nonreciprocal transmission.

## 2.1 Proposed scheme

The main building block of our design is a reversible  $IQ$  (in-phase/quadrature) modulator capable of performing noiseless frequency up- and down-conversion. A convenient analytical model capturing the fundamental properties of the device is shown in Fig. 2.1(a). The device comprises two low-frequency  $LC$  resonators (addressed by two semi-infinite transmission lines  $A'$  and  $A''$ ) coupled to a high frequency resonator (addressed by the transmission line  $B$ ) through time-varying couplings  $M_1, M_2$  that emulate the role of the pump drive in active nonlinear devices and transfer energy from the tone at  $\omega_c$  to the signal modes propagating on the transmission lines. The presence of two low-frequency ports allows us to operate the circuit in a manner analogous to the  $IQ$  modulation schemes routinely used in radiofrequency (RF) communication systems and microwave pulse engineering (hence the name). This circuit converts the two orthogonal spatial modes (low frequency signals of frequency  $\omega_m$  travelling on  $A', A''$ ) into two orthogonal temporal modes travelling on the same spatial line ( $B$ ) (sidebands at frequencies  $\omega_+, \omega_-$ ).<sup>1</sup> In view of the reversible frequency conversion performed by this device, we will henceforth refer to it as the up/down-converter (UDC). In practice, such a device can be implemented on-chip using a ring modulator based on Josephson junctions, along the lines of the recently demonstrated experiment with Josephson parametric converter [Bergeal et al., 2010b,a].

The complete design for the active circulator (Fig. 2.2) consists of a UDC functioning as a frequency up-converter, a phase-shifter and a second UDC functioning as a frequency down-converter. A concise representation of the dynamics at each of the three stages in the cascade is provided by the scattering matrix  $\mathbb{S}$  which relates the outgoing wave amplitudes to the incoming wave amplitudes as seen

---

<sup>1</sup>This construction is conducive from a transfer matrix analysis point-of-view also (presented in section 2.3), which becomes significantly straightforward for even number of participating modes.

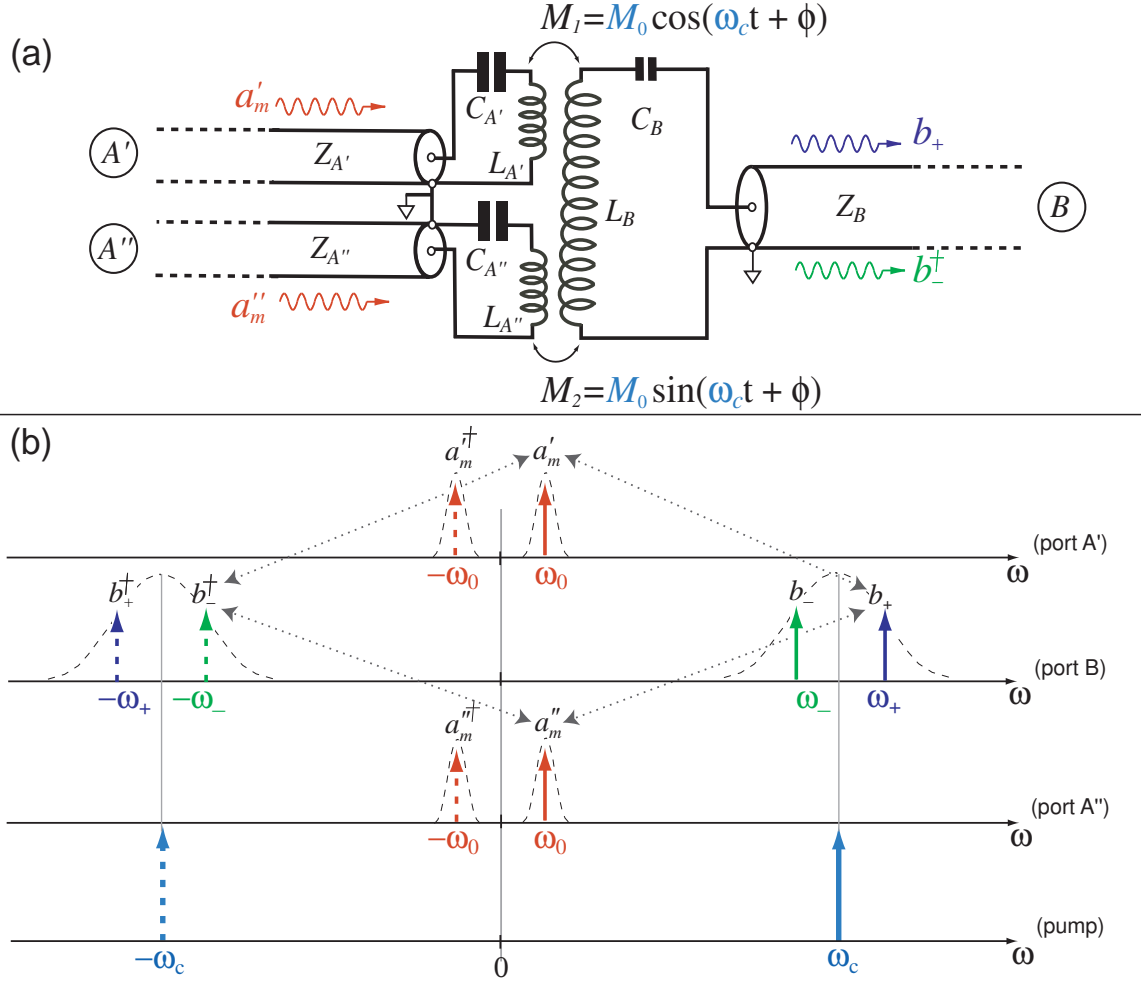


Figure 2.1: **Reversible I-Q modulator circuit.** (a) Circuit schematic of an active in-phase/quadrature modulator carrying out frequency up/down conversion (UDC) containing only dispersive components. The UDC performs the same operation as that of the circuit discussed in Fig. 1.6 but instead of one it has *two* low frequency ports  $A'$  and  $A''$  coupled to high frequency port  $B$ , with phases on the respective carriers differing by 90 degrees. (b) Spectral density/response landscape for various channels of the UDC. The dotted lines represent the couplings between different channels. The solid and the dashed arrows represent different frequencies and respective conjugates. The resonance lineshapes of the two spatially distinct channels  $A'$  and  $A''$  are centered at  $\omega_{A'} = \omega_{A''} = 1/\sqrt{L_{A',A''}C_{A',A''}}$ . Here we show the case when the incoming signal at  $\omega_m$  is resonant with the center frequency ( $\omega_m = \omega_{A',A''}$ ). The two sidebands generated by the UDC on channel  $B$  are detuned from the carrier  $\omega_c$  by equal and opposite amounts.

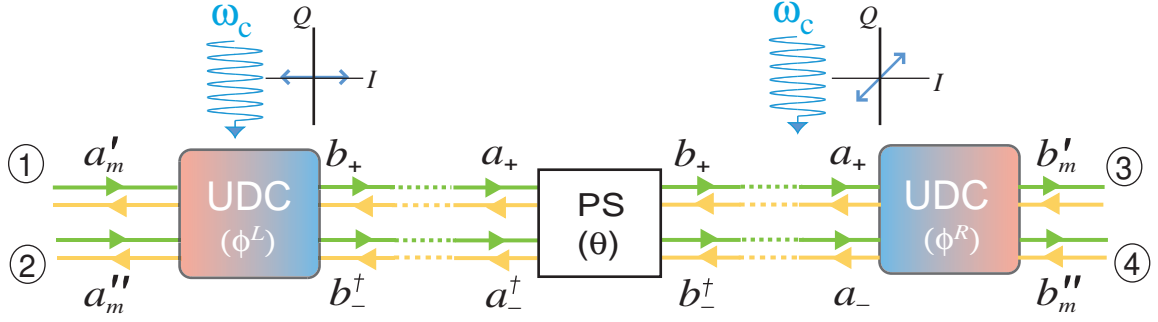


Figure 2.2: **Description of the active circulator.** Circuit schematic of the active circulator design: the first UDC stage acts as a frequency up-converter (indicated by a gradation in the color of the relevant box) with a parametric coupling modulated at the carrier frequency  $\omega_c = \omega_+ - \omega_m = \omega_- + \omega_m$  and a phase  $\phi^L$  indicated against the carrier wave in the  $IQ$  plane. This is followed by a phase shifter that phase shifts both the sidebands by  $\pi/2$ . The final UDC stage acts as a frequency down-converter, with the carrier phase  $\phi^R$ .

from different ports of the network. In the following section, we present detailed calculations of scattering matrix of each stage.

## 2.2 Scattering description of the individual components

As many readers might have already realized, the design of UDC closely shares its basic framework with the parametric frequency converter discussed in section 1.4.2. Each of its  $IQ$  coupled ports performs frequency mixing in a way described by the parametric model, though with different phases for the parametrically modulated coupling. The UDC system can be analyzed in the input-output paradigm using the method outlined in section 1.4.2 with inclusion of an extra low frequency port. Here we present a different but equivalent method to derive the scattering matrix  $\mathbb{S}$  which is based on the linear response approach and allows us to bypass writing down explicit equations of motion. This is accomplished by

evaluating the impedance matrix  $\mathbb{Z}$  of the UDC, as seen from its ports, and using the identity [Pozar, 2005]

$$\mathbb{S} = (\mathbb{Z} + \mathbb{Z}_0)^{-1} \times (\mathbb{Z} - \mathbb{Z}_0). \quad (2.1)$$

to calculate the  $\mathbb{S}$  matrix. Here

$$\mathbb{Z}_0 = \text{diag}(Z_{A'}, Z_{A''}, Z_B, Z_B), \quad (2.2)$$

with  $Z_{A'} = Z_{A''}$  and  $Z_B$  denoting the characteristic impedances of the semi-infinite transmission lines serving as low and high frequency ports respectively. For the parametrically coupled series LC oscillators forming the UDC stage, [Fig. 2.1 (a)], we obtain the total impedance matrix  $Z$  by adding the inductive ( $\mathbb{Z}_{\text{ind}}$ ) and capacitive ( $\mathbb{Z}_{\text{cap}}$ ) contributions respectively. The inductance matrix  $\mathbb{L}$  defines the constitutive relationship between the currents and fluxes for different inductances of the circuit:

$$\begin{pmatrix} \Phi'_m(t) \\ \Phi''_m(t) \\ \Phi_+(t) \\ \Phi_-(t) \end{pmatrix} = \begin{pmatrix} L_{A'} & 0 & M_0 e^{-i\phi} & M_0 e^{i\phi} \\ 0 & L_{A''} & iM_0 e^{-i\phi} & -iM_0 e^{i\phi} \\ M_0 e^{i\phi} & -iM_0 e^{i\phi} & L_B & 0 \\ M_0 e^{-i\phi} & iM_0 e^{-i\phi} & 0 & L_B \end{pmatrix} \begin{pmatrix} I'_m(t) \\ I''_m(t) \\ I_+(t) \\ I_-(t) \end{pmatrix} \quad (2.3)$$

$$= \mathbb{L} \begin{pmatrix} I'_m(t) \\ I''_m(t) \\ I_+(t) \\ I_-(t) \end{pmatrix}. \quad (2.4)$$

In writing the above matrix, we ignore the fluxes at higher harmonics of the modes at  $\omega_m$  and  $\omega_{\pm}$ . The inductive contribution to the impedance is then calculated

using the identity,  $V_i = \dot{\Phi}_i$ , to obtain

$$\begin{pmatrix} V'_m \\ V''_m \\ V_+ \\ V_- \end{pmatrix} = jL \underbrace{\begin{pmatrix} \omega_m & 0 & 0 & 0 \\ 0 & \omega_m & 0 & 0 \\ 0 & 0 & \omega_+ & 0 \\ 0 & 0 & 0 & -\omega_- \end{pmatrix}}_{Z_{\text{ind}}} \begin{pmatrix} I'_m \\ I''_m \\ I_+ \\ I_- \end{pmatrix}, \quad (2.5)$$

where the subscripts denote the relevant frequency modes. Here we have suppressed superscripts  $A$  and  $B$  for brevity. It is straightforward to define the capacitance matrix for the circuit in the same manner,

$$C = \text{diag}(C_{A'}, C_{A''}, C_B, C_B) \quad (2.6)$$

and obtain the capacitive contribution to the impedance,

$$\begin{pmatrix} V'_m \\ V''_m \\ V_+ \\ V_- \end{pmatrix} = (jC)^{-1} \underbrace{\begin{pmatrix} \omega_m & 0 & 0 & 0 \\ 0 & \omega_m & 0 & 0 \\ 0 & 0 & \omega_+ & 0 \\ 0 & 0 & 0 & -\omega_- \end{pmatrix}^{-1}}_{Z_{\text{cap}}} \begin{pmatrix} I'_m \\ I''_m \\ I_+ \\ I_- \end{pmatrix}. \quad (2.7)$$

The extra negative sign on the fourth element along the diagonal in the  $\omega$  matrix of equations (2.5) and (2.7) accounts for the generation of the conjugate wave amplitude  $a^\dagger[\omega_-]$  as a result of mixing the carrier  $\omega_c$  and signal  $\omega_m$ . Hence, on taking the Fourier transform of the current and voltage vectors, an extra negative sign appears for the corresponding coefficient. The total  $Z$  matrix, using Eqs. (2.5) and

(2.7), can thus be written as,

$$\begin{aligned} \mathbb{Z} &= \mathbb{Z}_{\text{ind}} + \mathbb{Z}_{\text{cap}} \\ &= \begin{pmatrix} -i\delta_m Z_{A',A''} & 0 & -i\alpha Z_B e^{-i\phi} & -i\alpha Z_B e^{i\phi} \\ 0 & -i\delta_m Z_{A',A''} & \alpha Z_B e^{-i\phi} & -\alpha Z_B e^{i\phi} \\ -i\alpha Z_{A',A''} e^{i\phi} & -\alpha Z_{A',A''} e^{i\phi} & -i\delta_{\pm} Z_B & 0 \\ i\alpha Z_{A',A''} e^{-i\phi} & -\alpha Z_{A',A''} e^{-i\phi} & 0 & -i\delta_{\pm} Z_B \end{pmatrix}. \end{aligned} \quad (2.8)$$

As in section 1.4.2, we have introduced the symbols

$$\begin{aligned} \delta_m &= \frac{|\omega_m - \omega_{A',A''}|}{\Gamma_{A',A''}}; & \Gamma_{A',A''} &= \frac{Z_{A',A''}}{2L_{A',A''}} \\ \delta_{\pm} &= \frac{|\omega_{\pm} - \omega_c|}{\Gamma_B}; & \Gamma_B &= \frac{Z_B}{2L_B} \\ \alpha &= \frac{M_0}{\sqrt{L_{A',A''} L_B}}, \end{aligned}$$

with  $\Gamma_i$  denoting the linewidth of the  $i^{\text{th}}$  resonator. The slight difference in the definition of linewidths  $\Gamma_i$  and coupling strength  $\alpha$  is a consequence of using parallel vs. series  $LC$  resonators in the two cases — the two descriptions, being dual to each other, are completely equivalent dynamically under RWA approximation (valid for sufficiently high quality factor resonance circuits). Using Eq. (2.8) in (2.1), we obtain the  $\mathbb{S}$ -matrix as:

$$\begin{pmatrix} a_m^{\text{out}} \\ a_m^{\prime\prime\text{out}} \\ b_+^{\text{out}} \\ b_-^{\dagger\text{out}} \end{pmatrix} = \begin{pmatrix} r_m & -q_m & t_d e^{-i\phi} & s_d e^{i\phi} \\ q_m & r_m & i t_d e^{-i\phi} & -i s_d e^{i\phi} \\ t_u e^{i\phi} & -i t_u e^{i\phi} & r_+ & 0 \\ -s_u e^{-i\phi} & -i s_u e^{-i\phi} & 0 & r_- \end{pmatrix} \begin{pmatrix} a_m^{\text{in}} \\ a_m^{\prime\prime\text{in}} \\ b_+^{\text{in}} \\ b_-^{\dagger\text{in}} \end{pmatrix}. \quad (2.9)$$

Here  $a$  and  $b$  denote the (reduced) amplitudes or the annihilation operators for the waves travelling on left and right transmission lines respectively. We follow this

convention for the rest of the circuit, as shown in Fig. 2.2. The reflection coefficients at various ports are denoted by  $r_m, r_+$  and  $r_-$ . The cross reflection between the low frequency signal ports is denoted by  $q_m$ . The transmission coefficients are written as  $t$  (transmission without conjugation) and  $s$  (transmission with conjugation) with subscripts ( $u, d$ ) indicating the up-conversion and down-conversion respectively. The detailed expressions of scattering coefficients are given by:

$$r_m = \frac{(\delta_m^2 + 1)(\delta_{\pm} + i)^2 - 4\alpha^4}{(\delta_m + i)^2(\delta_{\pm} + i)^2 - 4\alpha^4}; \quad (2.10a)$$

$$q_m = \frac{4\alpha^2(\delta_{\pm} + i)}{(\delta_m + i)^2(\delta_{\pm} + i)^2 - 4\alpha^4}; \quad (2.10b)$$

$$r_+ = \frac{(\delta_m + i)(\delta_{\pm} - i) - 2\alpha^2}{(\delta_m + i)(\delta_{\pm} + i) - 2\alpha^2}; \quad (2.10c)$$

$$r_- = \frac{(\delta_m + i)(\delta_{\pm} - i) + 2\alpha^2}{(\delta_m + i)(\delta_{\pm} + i) + 2\alpha^2}; \quad (2.10d)$$

$$t_u = t_d = i \left( \frac{2\alpha}{(\delta_m + i)(\delta_{\pm} + i) - 2\alpha^2} \right); \quad (2.10e)$$

$$s_u = s_d = i \left( \frac{2\alpha}{(\delta_m + i)(\delta_{\pm} + i) + 2\alpha^2} \right). \quad (2.10f)$$

Equations (2.10) show that the effective coupling strength  $\alpha$  plays the role of the parametric drive (“pump”) in the UDC. In the limit  $\alpha = 0$ , the transmission coefficients  $t_i$  and  $s_i$  become identically zero while the reflection coefficients  $r_i$  reduce to those for three independent series LCR circuits with resonance frequencies  $\omega_m$  and  $\omega_c$  respectively. It is useful to note that the phase of the carrier, denoted by  $\phi$ , affects only the transmitted amplitudes and rotates the two sidebands in opposite directions as can be seen from the corresponding scattering coefficients  $s$  and  $t$  in Eq. (2.9). The invariance of reflection amplitudes to the phase of the coupling will be important in understanding total reflections of the cascade, as we describe later.

We can similarly describe the action of the frequency-independent phase shift-

ing (PS) stage using a scattering matrix of the form

$$\begin{pmatrix} a_+^{\text{out}} \\ a_-^{\dagger\text{out}} \\ b_+^{\text{out}} \\ b_-^{\dagger\text{out}} \end{pmatrix} = \begin{pmatrix} 0 & 0 & e^{-i\theta} & 0 \\ 0 & 0 & 0 & e^{i\theta} \\ e^{-i\theta} & 0 & 0 & 0 \\ 0 & e^{i\theta} & 0 & 0 \end{pmatrix} \begin{pmatrix} a_+^{\text{in}} \\ a_-^{\dagger\text{in}} \\ b_+^{\text{in}} \\ b_-^{\dagger\text{in}} \end{pmatrix}. \quad (2.11)$$

## 2.3 Transfer Matrix Description

In order to obtain the combined action of the parametric chain, we use the transfer matrix formalism. Starting from an “in-out” scattering representation,

$$\begin{pmatrix} a^{\text{out}} \\ b^{\text{out}} \end{pmatrix} = \mathbb{S} \begin{pmatrix} a^{\text{in}} \\ b^{\text{in}} \end{pmatrix} \quad (2.12)$$

we can obtain a port-specific description using the transfer matrices as

$$\begin{pmatrix} b^{\text{out}} \\ b^{\text{in}} \end{pmatrix} = \mathbb{T} \begin{pmatrix} a^{\text{in}} \\ a^{\text{out}} \end{pmatrix} \quad (2.13)$$

where, as before,  $a$  and  $b$  denote the (reduced) amplitudes or the annihilation operators for the waves travelling on left and right hand side ports respectively. The reversal of ‘in’ and ‘out’ in the column vectors on the left and right hand sides of Eq. (2.13) is required to maintain a consistent sense of propagation through the device as the output of the  $(N - 1)^{\text{th}}$  stage acts as the input for the  $N^{\text{th}}$  stage in the chain. The transfer matrix representation allows us to calculate the total transfer matrix of the device in a straightforward manner by successively multiplying the transfer matrices calculated for each of the stages,

$$\mathbb{T}_{\text{total}} = \mathbb{T}_{DC} \times \mathbb{T}_{PS} \times \mathbb{T}_{UC}. \quad (2.14)$$

Here the subscripts  $UC$ ,  $DC$  index the upconversion ( $UC$ ) and downconversion ( $DC$ ) stages respectively (Fig. 2.2). The scattering matrix of the whole device is then obtained from  $T_{\text{total}}$  using the inverse of the transformation in Eq. (2.18). This transfer matrix description is equivalent to the usual  $ABCD$  matrix of the circuit theory defined in terms of the voltages and currents for a two-port network [Pozar, 2005],

$$\begin{pmatrix} V^b \\ I^b \end{pmatrix} = \begin{pmatrix} A & B \\ C & D \end{pmatrix} \begin{pmatrix} V^a \\ I^a \end{pmatrix}. \quad (2.15)$$

As there exists a straightforward mapping between the reduced wave amplitudes  $a_i$  introduced earlier, and the currents and voltages at the ports (Appendix B),

$$a^{\text{out},i}[\omega_j] = \frac{V^i + Z_i I^i}{\sqrt{2Z_i \hbar \omega_j}}, \quad (2.16)$$

$$a^{\text{in},i}[\omega_j] = \frac{V^i - Z_i I^i}{\sqrt{2Z_i \hbar \omega_j}}, \quad (2.17)$$

we can easily adapt the concept to the above choice of variables.

First, we derive the transfer matrix of the (left) UDC stage performing upconversion,  $\mathbb{T}_{UC}$ , by expressing sideband amplitudes ( $b_+$ ,  $b_-^\dagger$ ) in terms of low frequency amplitudes ( $a'_m$ ,  $a''_m$ ),

$$\begin{pmatrix} a'_m{}^{\text{out}} \\ a''_m{}^{\text{out}} \\ b_+^{\text{out}} \\ b_-^{\dagger\text{out}} \end{pmatrix} = \mathbb{S} \begin{pmatrix} a'_m{}^{\text{in}} \\ a''_m{}^{\text{in}} \\ b_+^{\text{in}} \\ b_-^{\dagger\text{in}} \end{pmatrix} \mapsto \begin{pmatrix} b_+^{\text{out}} \\ b_+^{\text{in}} \\ b_-^{\dagger\text{out}} \\ b_-^{\dagger\text{in}} \end{pmatrix} = \mathbb{T}_{UC} \begin{pmatrix} a'_m{}^{\text{in}} \\ a'_m{}^{\text{out}} \\ a''_m{}^{\text{in}} \\ a''_m{}^{\text{out}} \end{pmatrix}. \quad (2.18)$$

On performing the above transformation for Eq. (2.9), we obtain the transfer ma-

trix  $\mathbb{T}_{UC}$  as

$$\mathbb{T}_{UC} = \begin{pmatrix} t_+^{LR} e^{i\phi} & t_+^{*,RL} e^{i\phi} & -it_+^{LR} e^{i\phi} & it_+^{*,RL} e^{i\phi} \\ t_+^{RL} e^{i\phi} & t_+^{*,LR} e^{i\phi} & -it_+^{RL} e^{i\phi} & it_+^{*,LR} e^{i\phi} \\ t_-^{LR} e^{-i\phi} & t_-^{*,RL} e^{-i\phi} & it_-^{LR} e^{-i\phi} & it_-^{*,RL} e^{-i\phi} \\ t_-^{RL} e^{-i\phi} & t_-^{*,LR} e^{-i\phi} & it_-^{RL} e^{-i\phi} & it_-^{*,LR} e^{-i\phi} \end{pmatrix}, \quad (2.19)$$

with

$$\begin{aligned} t_+^{LR} &= i \left( \frac{(\delta_m - i)(\delta_{\pm} - i) - 2\alpha^2}{4\alpha} \right) \\ t_+^{RL} &= i \left( \frac{(\delta_m - i)(\delta_{\pm} + i) - 2\alpha^2}{4\alpha} \right) \\ t_-^{LR} &= i \left( \frac{(\delta_m - i)(\delta_{\pm} - i) + 2\alpha^2}{4\alpha} \right) \\ t_-^{RL} &= i \left( \frac{(\delta_m - i)(\delta_{\pm} + i) + 2\alpha^2}{4\alpha} \right). \end{aligned}$$

The subscripts (+, -) refer to the resultant sideband generated at the output ( $\omega_+$  or  $-\omega_-$ ) while  $LR(RL)$  indicates the relevant direction of propagation as *left-to-right* (*right-to-left*). We note that the condition for the transformation describing the mapping between  $\mathbb{S}$  and  $\mathbb{T}$  matrices to be non-singular is that the determinant of the off-diagonal blocks of  $\mathbb{S}$  be non-zero. This is achieved by having different phases for coupling (such as in the  $IQ$  scheme) the two low-frequency channels  $A'$  and  $A''$  with the high frequency channel  $B$  (Fig. 2.1). Further,  $IQ$  coupling ensures that mixing within sidebands is suppressed ( $s_{34}$  and  $s_{43}$ , are zero in Eq. (2.9)). However, if the phase difference between the two couplings  $M_1$  and  $M_2$  deviates from 90 degrees, crosstalk appears between the two sidebands generated at the high frequency port of the UDC. Furthermore, when  $M_1$  and  $M_2$  are completely in phase ( $I - I$ ), the two sidebands are maximally coupled while the cross reflections  $q_m$  between the low-frequency input ports reduce to zero. In such a case,

the aforementioned condition on the scattering matrix is violated and the usual transfer matrix analysis is precluded.

Using the method described for the UDC, we can similarly obtain the transfer matrix for the phase shifting stage from its scattering matrix [Eq. (2.11)]

$$\mathbb{T}_{PS} = \begin{pmatrix} e^{-i\theta} & 0 & 0 & 0 \\ 0 & e^{i\theta} & 0 & 0 \\ 0 & 0 & e^{i\theta} & 0 \\ 0 & 0 & 0 & e^{-i\theta} \end{pmatrix}. \quad (2.20)$$

We also note that

$$\begin{aligned} \mathbb{T}_{DC} &= \mathbb{F}^{-1} \times \mathbb{T}_{UC}^{-1} \times \mathbb{F} \\ &= \mathbb{F} \times \mathbb{T}_{UC}^{-1} \times \mathbb{F}, \quad (\mathbb{F}^{-1} = \mathbb{F}) \end{aligned} \quad (2.21)$$

where  $\mathbb{F} = \sigma_X \otimes \mathbb{U}_2$ , ( $\sigma_X$  is the 2D pauli spin matrix and  $\mathbb{U}_2$  is the 2D unity matrix). This matrix  $\mathbb{F}$  is required to flip the indices, thus maintaining consistency in labelling the ‘in’ and ‘out’ amplitudes along a given direction of propagation.

For simplicity we consider the operation at resonance, that is, when the input signal frequency coincides with the band center of the input resonators. Setting the phase of the pump at the first UDC stage  $\phi^L = 0$  for calculational simplicity, we observe a transmission resonance for  $\theta = \pm\pi/2$  (phase rotation by the PS stage),  $\phi^R = \pi/4$  (phase of the pump at the second UDC stage),  $\delta_{\pm} = 1/\sqrt{2}$  (detuning of the sidebands from the carrier in units of linewidth i.e. half width at full maximum of the resonance lineshape) of the high frequency resonator), and  $\alpha^L = \alpha^R = M_0/\sqrt{L_{A',A''}L_B} = 2^{-3/4}$  (strength of the parametric coupling). For this choice of parameters, we obtain the scattering matrix of the complete device (cf.

Fig. 2.2) as

$$\begin{pmatrix} a_m^{\prime\text{out}} \\ a_m^{\prime\prime\text{out}} \\ b_m^{\prime\text{out}} \\ b_m^{\prime\prime\text{out}} \end{pmatrix} = \mathbb{S}_{\text{total}} \begin{pmatrix} a_m^{\prime\text{in}} \\ a_m^{\prime\prime\text{in}} \\ b_m^{\prime\text{in}} \\ b_m^{\prime\prime\text{in}} \end{pmatrix}$$

with

$$\mathbb{S}_{\text{total}} = \begin{pmatrix} 0 & 0 & 0 & i \\ 0 & 0 & -i & 0 \\ i & 0 & 0 & 0 \\ 0 & i & 0 & 0 \end{pmatrix}. \quad (2.22)$$

This is the matrix of a perfect four-port circulator described in section A.2, up to constant phase factors.

## 2.4 Results and viability of the design

We next study the tolerance of the active circulator scheme to deviations of parameters such as the pump strength ( $\alpha$ ), phase shift ( $\theta$ ) and pump phase ( $\phi^R$ ) in Fig. 2.3. The plot in (a) shows that the design is robust to moderate deviations from the preferred phase angle  $\theta = \pi/2$ , and coupling (or equivalent pump strength)  $\alpha^R = \alpha^L = 2^{-3/4}$  (values indicated with dashed arrows along the axis; this makes the active circulator design a feasible candidate for use in practical circuits. Further, we see that the response is periodic in the pump phase  $\phi^R$  with a period equal to  $\pi$ . An interesting feature of our device is the reversal of its transmission characteristics with the phase of the pumps ( $\phi^{R,L} \mapsto -\phi^{L,R}$ ) [Fig. 2.3(c)]. In the classic circulators based on passive Faraday rotation, this can be accomplished by changing the polarity of the magnetic bias field. Thus the relative shift of the

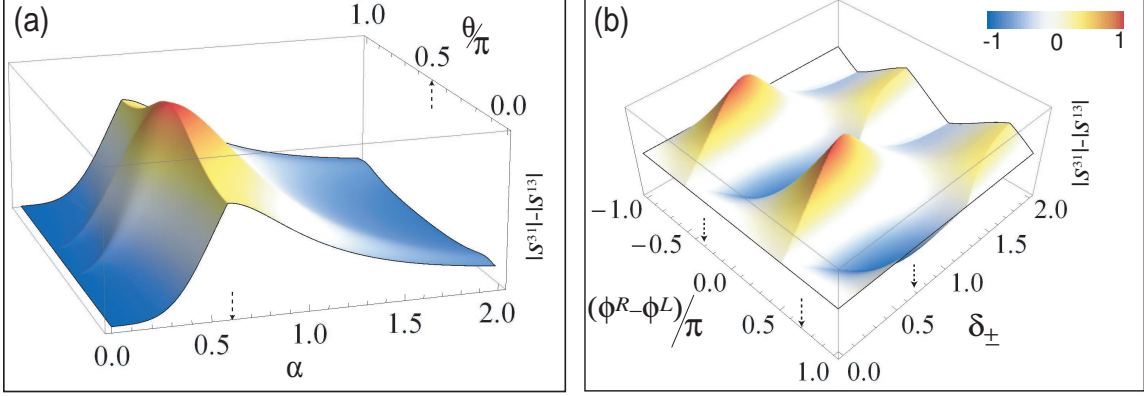


Figure 2.3: **Variation of the difference between forward and backward transmission coefficients ( $|s^{31}| - |s^{13}|$ ).** Asymmetry in transmission calculated as a function of strength of the coupling  $\alpha$  and phase rotation  $\theta$  carried out by the second phase-shifting stage (a), and detuning  $\delta_{\pm}$  and the phase of the pump at downconversion stage  $\phi^R$  (also the relative pump phase as  $\phi^L = 0$ ) (b). The points of maxima correspond to the ideal values reported in the text.

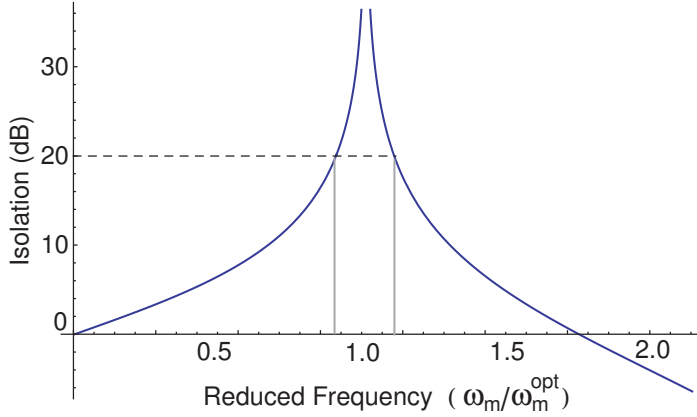


Figure 2.4: **Bandwidth of active circulator design.** Isolation of the active circulator as a function of reduced signal frequency  $\omega_m$  normalized in units of optimal signal frequency corresponding to maximum isolation ( $\omega_m^{\text{opt}} = \Gamma_{\pm}/\sqrt{2}$ ), calculated with  $\alpha = 2^{-3/4}$ ,  $\theta = \pi/2$  and  $\phi^R - \phi^L = \pi/4$ .

pump phase in an active device indeed plays a role equivalent to the magnetic field in a Faraday medium. One of the desirable characteristics of a circulator is wide bandwidth. The commercial designs available for typical cryogenic setups have operating frequency ranges of 4-8 GHz or 8-12 GHz for circulators and 4-12 GHz for isolators [Pamtech]. The typical bandwidth of active circulator design is

around quarter of an octave, mostly limited by the quality factor of the resonators employed in the active up/downconversion stages (Fig. 2.4). Though modest as compared to conventional designs, this suffices for the applications such as qubit readout. The main merit of incorporating such a device in the measurement chain is of course noiseless operation of the device, as opposed to intrinsically lossy passive realizations based on ferrites. Another characteristic of a circulator is its large power handling capability (usually in kilowatts for commercial designs). However, usually quantum systems are operated and measured at low powers at the level of a few photons. The throughput of the active circulator scheme, limited by the dynamic range of the parametric stages, should be sufficient for quantum information applications. Since the active UDC stages in our design are ideally realized using parametric devices like the JPC that employ large Josephson junctions, the throughput of our device compares favorably to other recently proposed passive designs based on small JJs shown in Fig. 2.5 [Koch et al., 2010]. Using large Josephson junctions also helps overcome the natural disadvantage of very small Josephson junctions which are susceptible to charging effects and hence charge noise.

Fig. 2.6 shows a representative experimental demonstration of the idea of realizing isolation with cascaded parametric up- and downconversion using a circuit employing regular mixers. The scheme shows an isolation of 30 dB between forward and backward transmission. In the forward direction, the transmission is  $-10$  dB, a figure entirely explained by the insertion loss of the mixers in the chain.

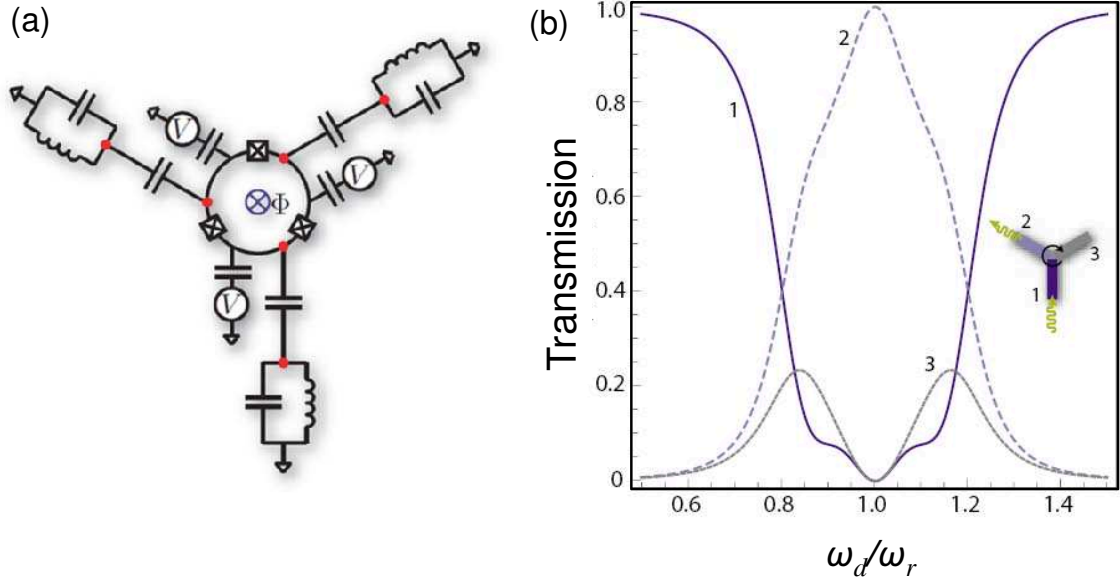


Figure 2.5: **Passive JJ-based circulator.** (a) A passive circuit comprising three JJs arranged in a flux-biased ring coupling three resonators proposed in Ref. [Koch et al., 2010]. By tuning the phase collected by the waves around the ring ( $\pi/6$ ) with the flux bias  $\Phi$ , the system shows circulator-like action. (b) Calculated transmission coefficients for appropriate phase, when port 1 is driven with a frequency  $\omega_d$ . For drive frequencies close to the resonator frequency  $\omega_r$ , the signal is transferred from port 1 to port 2 nonreciprocally.

## 2.5 Comparison of passive and active circulator designs

The analogy between a conventional circulator and the active circulator design proposed in this paper is made apparent from the respective wave propagation diagrams shown in Fig. 2.7. Nonetheless there are important differences between the two designs despite the identity of the final  $\mathbb{S}$  matrix. First and foremost, unlike the conventional design in Fig. 2.7(a), the waves travelling along different arms in Figs. 2.7(b), (c) are not of the same frequency. The active beam splitters (UDCs here) implement frequency conversion and the two interference ‘paths’ between the beam splitters refer to the two temporal channels in the frequency

domain (which actually travel on the same spatial port), as opposed to the two physically distinct, spatially separate paths in (a). Further, the coefficients on the forward (green) and backward (red) propagating arms of the active circulator design [Fig. 2.7(b)] involve deamplification followed by amplification, unlike the passive splitters (90 or 180 degree hybrids) employed in Faraday rotation schemes. This can be observed by squaring the amplitudes on each of the two arms originating from (or terminating into) a port and calculating the net power output, for each isolated UDC stage. It is straightforward to observe that, unlike the case of Fig. 2.7(a), they do not add up to unity. Nonetheless, the overall transmission is unity due to an exact cancellation of the reduction and gain in amplitudes. The wave propagation diagrams in Fig. 2.7(b) reveal another important difference of this design from that of a conventional circulator. The non-reciprocal action of the active circulator is not based upon any non-reciprocal phase shifters; instead it relies on the active stages used for frequency up- and down-conversion.

To further elucidate this point, let us reconsider the sub-matrix of Eq. (2.9) describing the scattering for one of the low-frequency  $I$  inputs,

$$\begin{pmatrix} r_m & te^{-i\phi} & se^{i\phi} \\ te^{i\phi} & r_+ & 0 \\ -se^{-i\phi} & 0 & r_-, \end{pmatrix} \quad (2.23)$$

where we have used the fact  $t_u = t_d = t$  and  $s_u = s_d = s$ . This matrix has the same structure as the matrix obtained in Eq. (1.37) for a minimal parametric mixer. As explained in section 1.4.2, the up- and downconversion blocks of this matrix implement the phase-sensitive rotations shown in Fig. 1.8. In active circulator design we have two such stages with the relative phase difference between carriers for up- and downconversion to be  $\pi/4$ . For such a configuration, the net rotations in

the forward and backward directions

$$[I, Q]_{FWD} = [I, Q]_{DC} \left( \frac{\pi}{4} \right) \times [I, Q]_{UC} (0) \quad (2.24)$$

$$[I, Q]_{BWD} = [I, Q]_{DC} (0) \times [I, Q]_{UC} \left( \frac{\pi}{4} \right) \quad (2.25)$$

in fact align along orthogonal quadratures in the  $I - Q$  plane, as shown in Fig. 2.8. Here the angles in parentheses denote the phase angles of the respective carrier phases. Thus in the forward direction, an  $I$  input after parametric rotations finds itself in the right quadrature to be demodulated into  $I$  channel; while in the backward direction it is demodulated into the  $Q$  channel leading to perfect isolation. The key idea to achieve nonreciprocity thus rests in exploiting *non-commutative phase-sensitive rotations* for channelling the signal transmission in orthogonal quadratures after forward and backward propagation through the device.

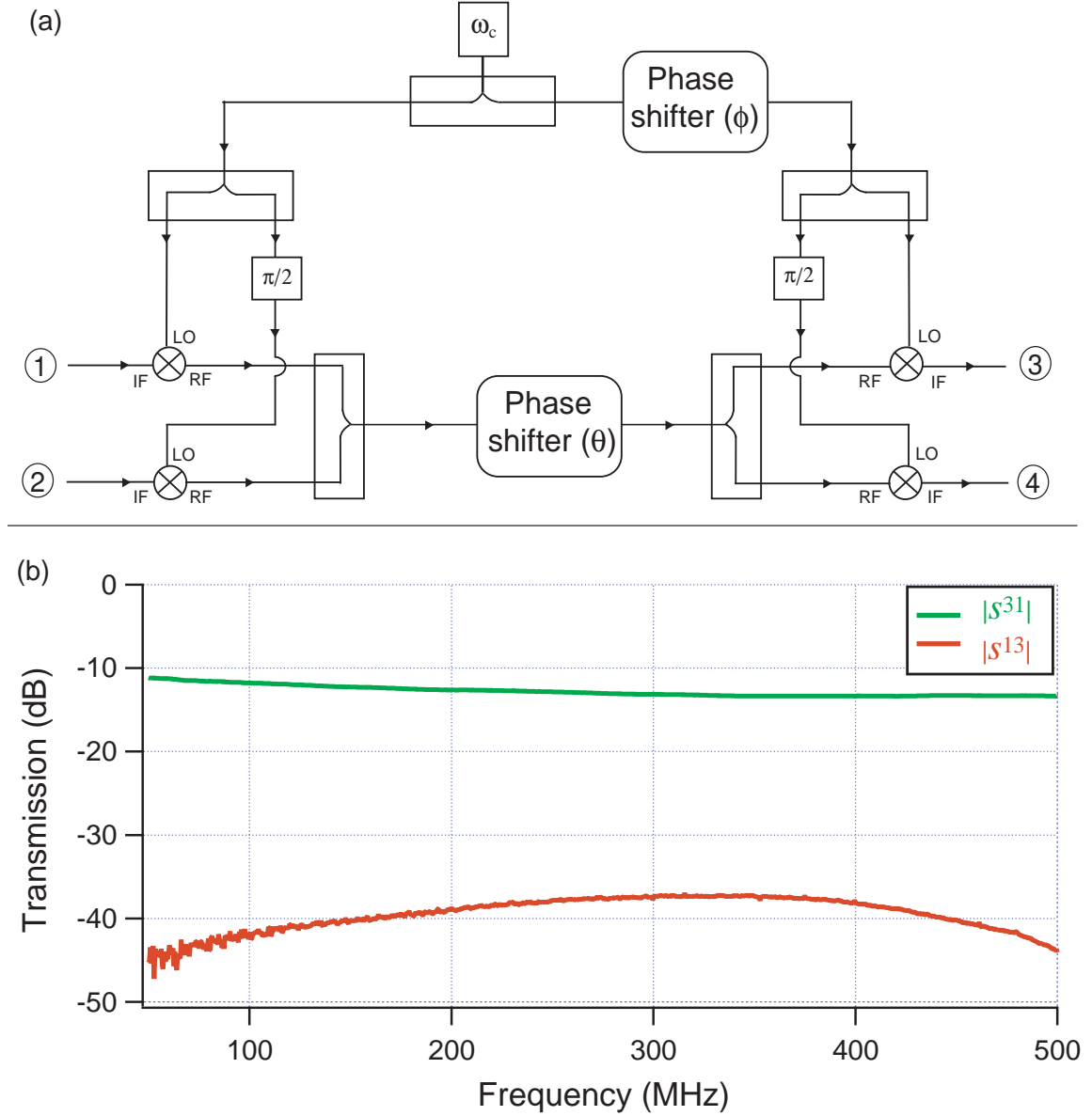


Figure 2.6: **Experimental demonstration of the active circulator idea using IQ mixers.** (a) Circuit schematic of a non-reversible circuit implementing the active circulator proposal. The circuit employs dissipative components such as the mixers (represented by the cross in circle symbol). At each stage, the CW tone from the generator imposing a carrier frequency  $\omega_c$  ('pump') is split into two copies, one phase shifted by  $\pi/2$  with respect to the other to realize an  $I - Q$  modulation of the carrier by the signal at  $\omega_m$ , as that described in Fig. 2.2(a). The modulated  $I$  and  $Q$  channels are then combined to propagate onto a single spatial channel which enter a phase shifter and then demodulated in a similar manner using a carrier that is phase shifted by  $\Delta\phi$ . (b) Measurement of forward ( $|S^{31}|$ ) and backward ( $|S^{13}|$ ) scattering coefficients using a vector network analyzer.

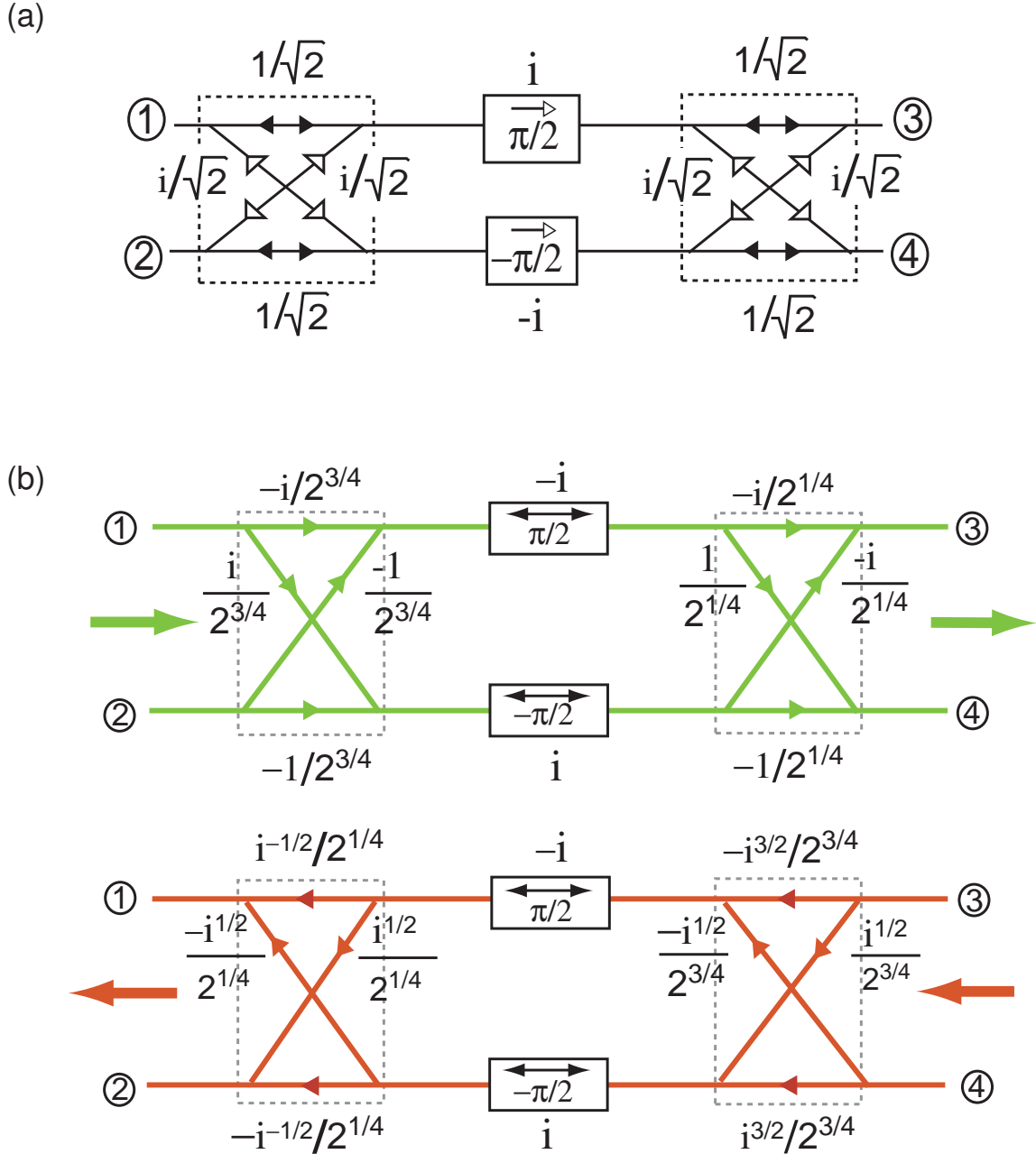


Figure 2.7: **Comparison of passive and active circulator designs.** (a) Wave propagation diagram of a conventional four-port passive circulator. The device consists of two 90 degree hybrids (equivalent to optical beam splitters) separated by a *non-reciprocal* phase shifter based on Faraday rotation. Solid black arrows indicate an amplitude split with no phase change while open arrows indicate an amplitude split with a 90 degree phase change. The non-reciprocal phase shift is effective only for the propagation direction indicated by the arrow on the phase shifter box. (b) Forward (green) and backward (red) propagation diagrams calculated using transfer matrix method for circuit in Fig. 2.2 with appropriate choice of detuning ( $\delta_{\pm} = 1/\sqrt{2}$ ) and coupling strengths ( $\alpha^L = \phi^R = 2^{-3/4}$ ) for maximum isolation.

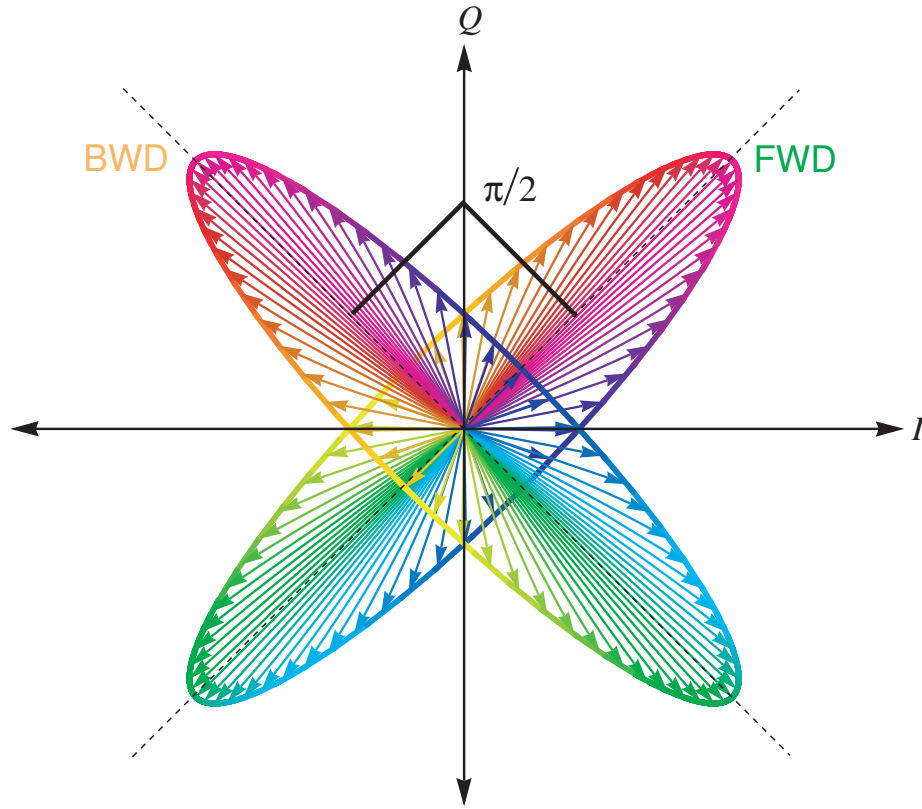


Figure 2.8: **Non-commutativity of phase-sensitive rotations.** Cascading two phase-sensitive rotations in an up-down conversion scheme leads to modulation along direction differing by  $\pi/2$  in the  $I - Q$  plane. This is due to the phase-sensitive nature of rotation of the parametric conversion process, as described in Fig. 1.8. Thus, a modulation with a zero phase followed by a demodulation with a  $\pi/4$  phase (Forward) is different from a modulation with  $\pi/4$  and demodulation with zero phase (Backward), due to non-commutativity of these rotations (the modulation phases are determined by the phases of the pump as explained previously). There is also a common phase change as shown by a change in position of the yellow arrow with respect to the semi-major axis, but this does not participate in deciding the net orientation as explained in Fig. 1.7(b).

---

## Nonreciprocity in frequency domain

---

*“There is nothing more deceptive than an obvious fact.”*

– Sherlock Holmes in *Boscombe Valley Mystery* (by Arthur Conan Doyle)

Recent ideas regarding reciprocityl symmetry breaking, in the realm of superconducting JJ-based devices, have involved multi-junction systems with both passive[Koch et al., 2010] and active realizations [Kamal et al., 2011], the latter as described in chapter 2. The active-circulator prototype showed that multiple parametric stages pumped using the same RF tone but appropriately tuned phases across stages can realize nonreciprocity in spatial channels. In both the passive and active realizations of non-magnetic nonreciprocal systems, the crux of the mechanism of symmetry breaking rests on a passive (flux in a superconducting ring) or active (carrier phase gradient in a parametric JJ device) ‘bias’ imposed externally on the system. This causes the signals to gather appropriate phase shifts leading to an interferometric reinforcement in one preferred direction set by the bias. In this chapter, we explore a novel form of nonreciprocity in temporal channels, which manifests itself as symmetry breaking in frequency domain. Though this may seem like an unconventional place to look for nonreciprocity at first glance, it is actually more natural to think about it in the paradigm of para-

metric processes whose dynamics essentially entail nonlinear frequency mixing. Hence, this exercise may unravel the possibility of symmetry breaking at an even more fundamental level in single JJ devices.

The system of our choice is a single resistively-shunted junction (RSJ), biased using a dc current. This choice is not quite random, but rather an inspired guess. The RSJ, besides being studied extensively both theoretically [Ingold et al., 1994] and experimentally [Koch et al., 1980; Joyez et al., 1999] in the past, has provided a model system for study of directed transport phenomenon such as realization of *fluxon ratchets*. This mode of a current-biased single junction has received much attention in recent years, though most investigations have centered on the dc current-voltage characteristics of such systems, such as those discussed in section 1.5. In the following sections, we will attempt to gain a detailed understanding of ac dynamics of an RSJ by studying it as a scatterer for microwaves. The language of our analysis will be provided by the input-output theory of circuits (Appendix B), well suited for such an exercise. There a dc understanding at rf frequencies of A scattering description of the RSJ will also provide us with crucial insights into the directionality of the microwave SQUID amplifier, which has the dynamics of a “two-dimensional” RSJ.

### 3.1 Resistively-shunted junction (RSJ): A case study

We will begin with a brief introduction of an RSJ biased in the voltage (or running) regime of the junction by means of a dc current  $I_B > I_0$ , where  $I_0$  represents the critical current of the junction. In the presence of a dc current bias, we can write down the Kirchhoff’s current law for the circuit shown in Fig. 3.1(a) as

$$I(t) + J(t) = I_B + I_{RF}(t) \quad (3.1)$$

Using the first Josephson relation  $J = I_0 \sin \phi$  and the identification  $V(= IR) = \varphi_0 \dot{\phi}$ , where  $\varphi_0 = \hbar/2e$  is the reduced flux quantum, the dynamics of the junction can be modelled by means of a nonlinear equation of motion for the phase difference  $\varphi$  across the junction

$$\frac{\varphi_0}{R} \dot{\phi} + I_0 \frac{\partial}{\partial \varphi} \left( \frac{U}{E_J} \right) = I_{RF}(t),^1 \quad (3.2)$$

in a *washboard potential* (Fig. 3.1(b)).

$$U = E_J \left( 1 - \cos \varphi - \varphi \frac{I_B}{I_0} \right). \quad (3.3)$$

Equation (3.2) describes an overdamped oscillator with characteristic frequency  $\omega_0 \equiv I_0 R / \varphi_0$ . This Josephson frequency can also be thought of as the frequency of oscillation of the supercurrent flowing in the junction at the characteristic dc voltage  $V_{dc} = I_0 R$  (with the identification  $\omega_J = V_{dc} / \varphi_0$  according to second Josephson relation).

To facilitate an input-output analysis of the RSJ circuit (see Appendix B for details), we represent the shunt resistor  $R$  as a semi-infinite transmission line of characteristic impedance  $R$ , with the rf drive modelled as incoming waves represented as  $I_{RF}(t) = 2A^{\text{in}} / \sqrt{R}$  (shown in Fig. 3.1(c)). This leads us to the relation

$$\tilde{\omega} + \hat{\omega} = \omega_B + 2\omega^{\text{in}}(t), \quad (3.4)$$

where we have expressed all currents and voltages in equivalent frequency (or

---

<sup>1</sup>Taking into account the junction capacitance leads to an ‘inertia’ term for the phase particle, of the form  $RC\ddot{\phi}$ .

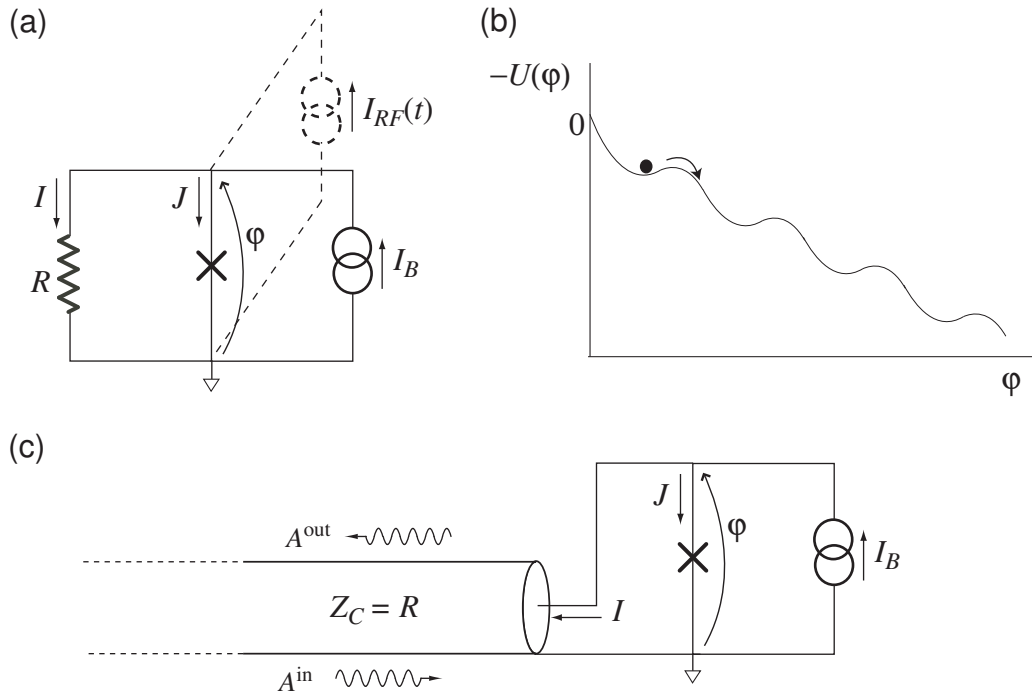


Figure 3.1: **Current-biased resistively shunted junction (RSJ)**. (a) Circuit schematic of a resistively shunted junction (RSJ) with a dc current bias  $I_B > I_0$ . (b) The effective potential of the junction with a current bias above the critical current of the junction. In this regime, the phase particles runs down a tilted washboard sampling different Josephson cosine wells leading to appearance of a net voltage across the junction (hence this regime is also called the voltage or running regime). (c) Equivalent input-output model for an RSJ where the signals of interest are expressed as propagating waves travelling on a semi-infinite transmission line.

energy) units

$$\widehat{\omega} \equiv \frac{JR}{\varphi_0} \quad (\text{junction current}) \quad (3.5)$$

$$\check{\omega} \equiv \frac{V}{\varphi_0} \quad (\text{junction voltage}) \quad (3.6)$$

$$\omega_B \equiv \frac{I_B R}{\varphi_0}; \quad \omega_0 \equiv \frac{I_0 R}{\varphi_0} \quad (\text{characteristic currents}). \quad (3.7)$$

It is instructive to note that Eq. (3.2) includes nonlinearity to infinite order due to the presence of the  $\sin \varphi$  term in  $\widehat{\omega}$ . Nonetheless, we can work in the perturbative limit assuming the phase fluctuating component of the phase induced by the oscillating current  $I_{RF}(t)$  to be small compared to the average value of the phase in the running state (i.e.  $I_B > I_0$ ). Thus, we may express the phase  $\varphi$  across the junction,

$$\varphi = \omega_J t + \delta\varphi(t) \quad (3.8)$$

and expand the  $\sin \varphi$  term as a series in  $\delta\varphi$  about the working point set by the average value of the phase diffusion across the junction corresponding to a voltage  $\langle \check{\omega} \rangle = \omega_J$  (second Josephson relation).

## 3.2 Harmonic Balance Treatment

To enable a harmonic balance analysis, we decompose the perturbative component of the phase,  $\delta\varphi$  in Eq. (3.8), in two oscillating parts:

$$\delta\varphi(t) = \Pi(t) + \Sigma(t), \quad (3.9)$$

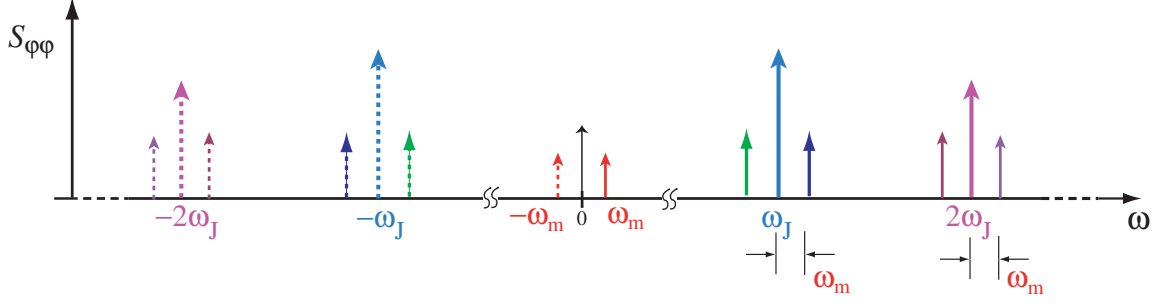


Figure 3.2: **Frequency landscape for a junction in voltage state.** Relevant frequencies for a harmonic balance analysis of an RSJ biased in the voltage or running regime. The solid and the dashed arrows represent different frequencies and respective conjugates. The tall arrows represent the various Josephson harmonics  $\Pi(t)$  while the shorter arrows represent the signal and sideband frequencies  $\Sigma(t)$ . The dc bias is represented by a black arrow at zero frequency.

with  $\langle \dot{\Pi}(t) \rangle = \langle \dot{\Sigma}(t) \rangle = 0$  and,

$$\Pi = \sum_{k=1}^K p_k^x \cos k\omega_J t + p_k^y \sin k\omega_J t \quad (3.10)$$

$$\Sigma = \sum_{n=-N}^{+N} s_n^x \cos(n\omega_J + \omega_m)t + s_n^y \sin(n\omega_J + \omega_m)t. \quad (3.11)$$

This exercise enables a calculation of the response of the junction at the relevant frequencies of interest (Fig. 3.2). Here  $\Pi(t)$  represents the phase components oscillating at the Josephson frequency and its harmonics while  $\Sigma(t)$  represents the components at the signal frequency  $\omega_m$  ( $\ll \omega_J$ ) and the corresponding sidebands  $\omega_{\pm N} = N\omega_J \pm \omega_m$  generated due to the frequency mixing performed by the non-linearity of JJ.

### 3.2.1 Steady-state response: I-V characteristics

We first evaluate the  $\delta\phi_P$  part of the system response at Josephson frequency and harmonics ( $\omega_J, 2\omega_J, \dots$ ). We do this by evaluating the steady state response of the junction, by setting  $\omega^{\text{in}}(t) = 0$  in Eq. (3.4) as these are generated internally in the

running regime and are not controlled by any external input drive<sup>2</sup>.

As a check of the convergence and accuracy of the harmonic series expansion, we self-consistently evaluate the dc contribution along with the response at Josephson frequency and compare it with the exact expression known for the IV-characteristics for the RSJ as  $\omega_J = \sqrt{\omega_B^2 - \omega_0^2}$ . This is necessitated by the connection between the amplitude of the dc voltage that appears across the junction and the frequency of Josephson oscillation in the running state as per the second Josephson relation.

For illustrative purposes, let us consider the expansion of the sine nonlinearity to lowest order in  $\Pi(t)$  and include only the first Josephson harmonic in our analysis [ $K = 1$  in Eq. (3.10)]. Now from Eq. (3.4), we have

$$\check{\omega}[\omega_J] + \hat{\omega}[\omega_J] = 0 \quad (3.12)$$

with

$$\begin{aligned} \check{\omega} &= \dot{\varphi} \\ &= \omega_J + \dot{\Pi}_{K=1} \\ &= \omega_J - p_1^x \omega_J \sin(\omega_J t) + p_1^y \omega_J \cos(\omega_J t) \end{aligned} \quad (3.13)$$

and

$$\begin{aligned} \hat{\omega} &= \omega_0 \sin \phi = \omega_0 \sin(\omega_J t + \Pi_{K=1}) \\ &= \omega_0 \sin(\omega_J t) + \omega_0 \cos(\omega_J t) \Pi_{K=1} \\ &= \omega_0 \sin(\omega_J t) + \omega_0 \cos(\omega_J t) [p_1^x \cos(\omega_J t) + p_1^y \sin(\omega_J t)]. \end{aligned} \quad (3.14)$$

---

<sup>2</sup>We have also ignored quantum fluctuations at the Josephson frequency and harmonics.

Collecting terms oscillating at  $\omega_J$  from Eqs. (3.13) and (3.14), we obtain

$$p_1^x = \frac{\omega_0}{\omega_J}; \quad p_1^y = 0. \quad (3.15)$$

Collecting terms at dc from Eqs. (3.13) and (3.14) and using the value of the Josephson oscillation amplitude obtained above, we get

$$\omega_J + \frac{\omega_0^2}{2\omega_J} = \omega_B. \quad (3.16)$$

Solving this quadratic equation in  $\omega_J$  and retaining the leading order term gives

$$\omega_J = \omega_B \left( 1 - \frac{1}{2} \frac{\omega_0^2}{\omega_B^2} \right). \quad (3.17)$$

This expression agrees exactly with the leading order contribution of the exact dc solution  $\omega_J = \sqrt{\omega_B^2 - \omega_0^2}$  [Henry et al., 1981].

This method becomes computationally intensive for higher order expansions in the perturbation  $\Pi(t)$ . It becomes important to include the effect of Josephson harmonics and their sidebands at higher orders, as we access the nonlinear portion of the dc characteristics by reducing the bias current  $I_B$  towards the critical current of the junction  $I_0$ . This is evident from the phase trajectories shown in Fig. 3.3, calculated by a direct numerical integration of Eq. (3.2) in steady state ( $I_{RF}(t) = 0$ ). A clever trick is to expand the Josephson amplitudes  $p_{k,x}$ ,  $p_{k,y}$  and frequency  $\omega_J$  as a truncated power series in a small expansion parameter of choice,

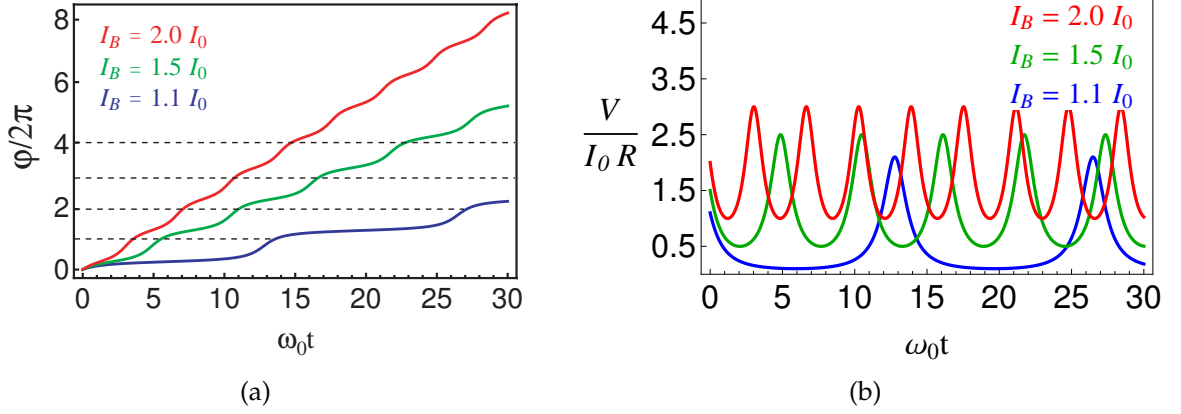


Figure 3.3: **Phase evolution of current-biased RSJL.** (a) Phase evolution of the JJ in a tilted washboard potential and the (b) corresponding voltage across JJ for three different values of dc bias current  $I_B$ . As  $I_B$  is reduced towards  $I_0$ , the particle motion becomes increasingly nonlinear which leads to the generation of higher Josephson harmonics.

say  $\varepsilon$ ,

$$p_k^x = \sum_{i=0}^{2K-1} p_{k,i}^x \varepsilon^i \quad (3.18)$$

$$p_k^y = \sum_{i=0}^{2K-1} p_{k,i}^y \varepsilon^i \quad (3.19)$$

$$\omega_J = \sum_{i=0}^{2K} w_{J,i} \varepsilon^i \quad (3.20)$$

and then impose harmonic balance at each order of  $\varepsilon$ . The degree  $k$  of the resultant polynomial evaluation of  $a$  and  $b$  coefficients is set by the desired order of expansion in  $\delta\phi$ . The expansion parameter can be chosen to be either an *explicit* bias parameter such as the inverse of the bias current  $\varepsilon = \omega_0/\omega_B$  (as  $I_0 < I_B$  in the running regime of JJ), or an *implicit* bias seen by the junction such as the dc voltage  $\varepsilon = \omega_0/\omega_J$  that appears across the JJ in the running regime. Here we have chosen the normalization constant to be the characteristic Josephson frequency  $\omega_0$  corresponding to the critical current of the junction.

Use of these expansions in Eq. (3.12) leads to a system of linear simultane-

ous equations correct to the relevant order in the perturbation parameter  $\varepsilon$ . They can be then solved to calculate the amplitude and frequency of Josephson oscillation as a power series in  $\varepsilon$ . Determination of the Josephson frequency also leads to an automatic evaluation of dc voltage as  $\omega_J = \langle \tilde{\omega} \rangle$ . Figure 3.4 shows the dc characteristics evaluated in this manner for expansion of the  $\sin \varphi$  nonlinearity up to the first, third and fifth order respectively. Equivalent expansions in previous works [Clerk, 2006; Ingold and Grabert, 1999] have confirmed the convergence of such perturbation series methods for experimentally relevant parameters. Furthermore, this parameter serves as the effective strength of the different Josephson harmonics which play a role analogous to the strong “pump” tone of conventional parametric amplifiers. The pump values calculated using this approach for the case of  $K = 1$  in Eq. (3.10) are

$$p_{1,0}^x = 0; \quad p_{1,1}^x = \varepsilon \quad (3.21a)$$

$$p_{1,0}^y = 0; \quad p_{1,1}^y = 0. \quad (3.21b)$$

with

$$w_{J,0} = 1; \quad w_{J,1} = 0; \quad w_{J,2} = \frac{1}{2} \quad (3.22)$$

corresponding with the exact expansion for dc voltage  $\omega_J$  to second order in  $\varepsilon$

$$\frac{\omega_J}{\omega_B} = 1 - \frac{\varepsilon^2}{2}. \quad (3.23)$$

Similarly, on going to the next order in the perturbation [ $K=2$  in Eq. (3.10)], we

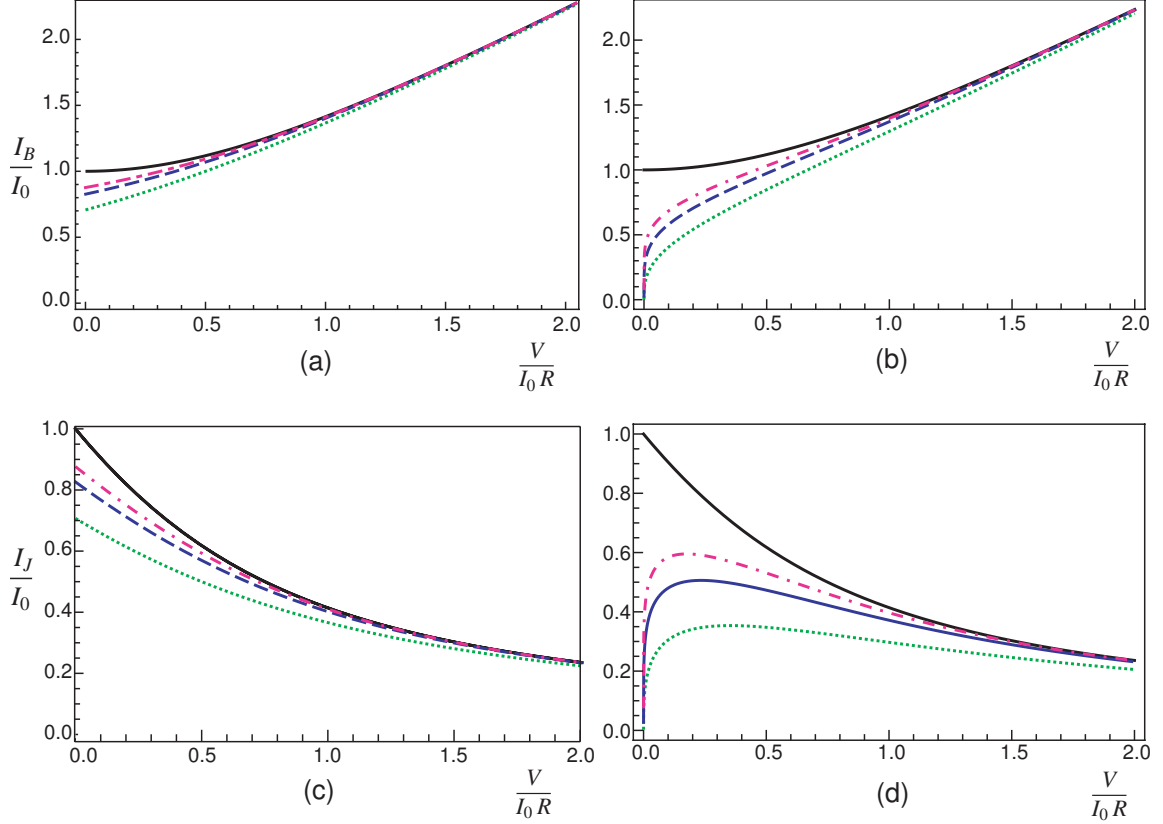


Figure 3.4: **DC characteristics of an RSJ.** Comparison of dc IV characteristics of an RSJ calculated using the harmonic series method for different orders of expansion in junction nonlinearity. In each plot the solid black line represents the exact analytical result  $\omega_J = \sqrt{\omega_B^2 - \omega_0^2}$ , while green (dotted), blue (dashed) and violet (dotted-dashed) curves show the calculated dc response using the harmonic balance treatment with one [K=1], two [K=2] or three [K=3] Josephson harmonics respectively. Figures (a) and (b) show the variation of bias current  $I_B$  as a function of voltage  $V$  across the junction, calculated using  $\varepsilon = \omega_0/\omega_B$  and  $\varepsilon = \omega_0/\omega_J$  as the expansion parameter respectively. Figures (c) and (d) show the corresponding curves for current flowing the junction  $J$  as a function of voltage  $V$ .

find the following series for the amplitudes of higher Josephson harmonics

$$p_{1,0}^x = 0; \quad p_{1,1}^x = \varepsilon; \quad p_{1,2}^x = 0; \quad p_{1,3}^x = \frac{\varepsilon^3}{4} \quad (3.24a)$$

$$p_{1,0}^y = 0; \quad p_{1,1}^y = 0; \quad p_{1,2}^y = 0; \quad p_{1,3}^y = 0 \quad (3.24b)$$

$$p_{2,0}^x = 0; \quad p_{2,1}^x = 0; \quad p_{2,2}^x = 0; \quad p_{2,3}^x = 0 \quad (3.24c)$$

$$p_{2,0}^y = 0; \quad p_{2,1}^y = 0; \quad p_{2,2}^y = -\frac{\varepsilon^2}{4}; \quad p_{2,3}^y = 0. \quad (3.24d)$$

along with the dc contribution

$$\begin{aligned} w_{J,0} = 1; \quad w_{J,1} = 0; \quad w_{J,2} = -\frac{1}{2} \\ w_{J,3} = 0; \quad w_{J,4} = -\frac{1}{8} \end{aligned} \quad (3.25)$$

On extending the analysis, we find that the series of Josephson harmonics generated by the junction is of the form,

$$\Pi(t) = \sum_{k=1}^K p_{2k-1}^x \cos[(2k-1)\omega_J t] + p_{2k}^y \sin[(2k)\omega_J t]. \quad (3.26)$$

Such a series with alternate even and odd harmonics phase shifted by  $\pi/2$  is frequently encountered in nonlinear systems such as driven ratchets and leads to directed transport. In the following section, we will elucidate the symmetry breaking in frequency conversion performed by a JJ pumped by a biharmonic drive.

### 3.2.2 RF response: Symmetry breaking in frequency conversion

Proceeding along the lines delineated in the last section, we now evaluate the response of the junction at the signal and sideband frequencies. For this purpose, we consider the second part of the phase perturbation  $\Sigma(t)$  [see Eq. (3.11)] and perform the harmonic balance of Eq. (3.4) at  $\omega_m$  and  $n\omega_J \pm \omega_m$ . In this analysis the input/source term  $\omega^{\text{in}}(t)$  is included, which represents either the quantum fluctuations or a weak probe at the signal frequency. The various Josephson harmonics ( $\Pi(t)$ ) evaluated earlier play the role of an effective ‘colored’ pump seen by the junction. This can be seen by considering the lowest order dynamics in the small

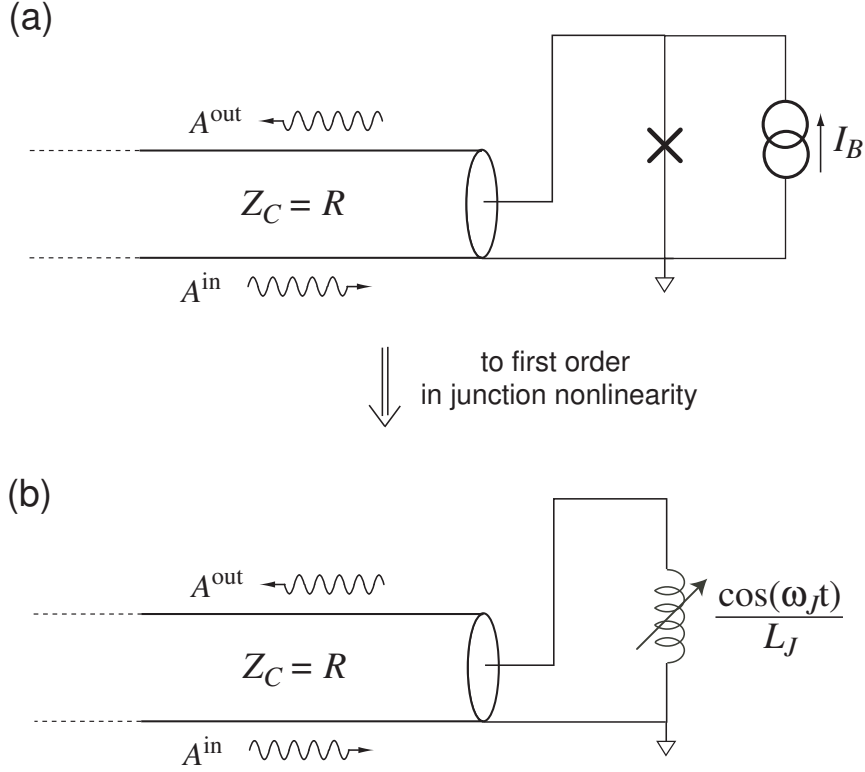


Figure 3.5: **Equivalence between a junction in voltage state and a paramp.** Circuit schematic showing the equivalence of a current-biased RSJ in (a) with a parametrically varying inductance  $L_J = I_0\varphi_0$  in (b). The pump is the internal Josephson oscillation of frequency  $\omega_J$  generated due to phase running in the voltage state.

signal limit  $\Sigma(t)/(\omega_J t) \ll \Pi(t)/(\omega_J t) \ll 1$  described by Eq. (3.4) as

$$\delta\dot{\Sigma} + \omega_0 \cos(\omega_J t)\Sigma = 2\omega^{\text{in}}(t). \quad (3.27)$$

Eq. (3.27) describes an inductance, parametrically varied using a “pump” of frequency  $\omega_J$  and strength  $\omega_0$  set by the critical current of the junction (Fig. 3.5).

Thus in the limit of a small amplitude input signal, which is the relevant limit for most practical situations, we can describe the junction dynamics as that of a parametric oscillator pumped by different Josephson harmonics. We can then employ the usual input-output theory (Appendix B), to write down a linear response description in terms of an admittance matrix  $\mathbb{Y}_J$  as seen from the resistance

port. This can be obtained from the current-phase and voltage-phase relationships [Eqs. (3.5),(3.6)]

$$\hat{\omega} = \hat{\mathbb{M}}\Sigma, \quad (3.28)$$

$$\check{\omega} = \check{\mathbb{M}}\Sigma \quad (3.29)$$

as

$$\mathbb{Y}_J = \hat{\mathbb{M}}\check{\mathbb{M}}^{-1}. \quad (3.30)$$

The vectors in the equations above are defined in the basis of all signal and side-band frequencies of interest,  $(n\omega_J + \omega_m)$ ,  $n \in [-N, +N]$  leading to a  $2(2N + 1) \times 2(2N + 1)$  admittance matrix. We further note that the matrix is block diagonal

$$\mathbb{Y}_J = \begin{pmatrix} Y & 0 \\ 0 & Y^* \end{pmatrix}. \quad (3.31)$$

since harmonic balance leads to two disjoint mixing manifolds  $(\pm\omega_s, \pm\omega_J \pm \omega_s, \mp\omega_J \pm \omega_s)$  with  $(2N + 1)$  frequencies each. Each sub-matrix  $Y$  is a square matrix of the form,

$$Y = \frac{i\varepsilon}{2} \begin{pmatrix} 0 & \frac{-f(\varepsilon)}{(\Omega_J + \Omega_m)} & \frac{f(\varepsilon)}{(\Omega_J - \Omega_m)} \\ \frac{-f(\varepsilon)}{\Omega_m} & 0 & y_+ \\ \frac{-f(\varepsilon)}{\Omega_m} & y_- & 0 \end{pmatrix}, \quad (3.32)$$

where  $f(\varepsilon)$  is a real-valued polynomial function in  $\varepsilon$  whose explicit form depends on the order of expansion and  $\Omega_m = \omega_m/\omega_B$  represents the normalized signal frequency. We have chosen to work with the  $\varepsilon$  expansion as it offers slightly better convergence at a given order as shown by Fig. 3.4 — it is straightforward to

switch from one representation to another using the constitutive relations provided by the dc calculation). For calculating the above admittance matrix, we have restricted ourselves to  $N = 1$  in Eq. (3.11) i.e. sidebands of only the first Josephson harmonic  $\omega_J$  are included.

To elucidate the dispersive ratchet implemented by the dc-biased RSJ, we consider two cases:

- *Case I:*  $\Pi(t) = \varepsilon \cos \omega_J t$  [see Eq. (3.21)].

In this case,

$$y_+ = y_- = 0; \quad f(\varepsilon) = 1.$$

- *Case II:*  $\Pi(t) = \left(\varepsilon + \frac{\varepsilon^3}{4}\right) \cos \omega_J t - \frac{\varepsilon^2}{4} \sin(2\omega_J t)$  [see Eq. (3.24)].

In this case,

$$y_{\pm} = \frac{i\varepsilon}{2(\Omega_J \mp \Omega_m)}; \quad f(\varepsilon) = \left(1 - \frac{\varepsilon^2}{4}\right). \quad (3.33)$$

The presence of the second Josephson harmonic  $2\omega_J$  thus leads to additional off-diagonal terms mixing the two sidebands  $\Omega_J \pm \Omega_m$ . It should be noted that these terms carry an additional phase  $i$  with respect to other components in the matrix due to the phase shift  $\pi/2$  of the second harmonic with respect to the Josephson frequency  $\omega_J$ .

We may now evaluate the scattering matrix  $\mathbb{S}$  of the RSJ from  $\mathbb{Y}_J$  using the identity,

$$\mathbb{S} = \Omega^{-1}(1 + \mathbb{Y}_J)^{-1}(1 - \mathbb{Y}_J)\Omega, \quad (3.34)$$

for both the cases listed above. We obtain

$$\mathbb{S} = \begin{pmatrix} r_m & t_d & s_d \\ t_u & r_+ & v_{+-} \\ -s_u & v_{-+} & r_- \end{pmatrix}, \quad (3.35)$$

where the matrix  $\Omega = \text{diag}(|\Omega_J + \Omega_m|, |\Omega_m|, |\Omega_J - \Omega_m|)$  is used to normalize the scattering coefficients in terms of single photon fluxes.

- *Case I:* On including only the first Josephson harmonic in our calculation [K=1], we obtain

$$r_m = 1 + \frac{\varepsilon^2}{1 - \Omega_m^2} \quad (3.36a)$$

$$r_+ = 1 - \frac{\varepsilon^2}{2\Omega_m(1 + \Omega_m)} \quad (3.36b)$$

$$r_- = 1 + \frac{\varepsilon^2}{2\Omega_m(1 - \Omega_m)} \quad (3.36c)$$

$$t_d = t_u = \frac{-i\varepsilon}{\sqrt{\Omega_m(1 + \Omega_m)}}, \quad (3.36d)$$

$$s_d = s_u = \frac{i\varepsilon}{\sqrt{\Omega_m(1 - \Omega_m)}}, \quad (3.36e)$$

$$v_{+-} = v_{-+} = 0, \quad (3.36f)$$

where we have used the second Josephson relation to relevant order  $\Omega_J = \langle \tilde{\omega} \rangle / \omega_B = (2 + \varepsilon^2)/2$  for expressing all coefficients solely in terms of bias parameter  $\varepsilon$  and input frequency  $\Omega_m$ . All scattering coefficients are correct up to  $\mathcal{O}(\varepsilon^2)$  and the  $\mathbb{S}$  matrix is symplectic up to  $\mathcal{O}(\varepsilon^3)$ .

Eqs. (3.36) show that at first order, we recover the usual symmetric scattering. The junction functions as a regular mixer with net frequency up- and downconversion being equal with respect to both the sidebands [Fig. 3.6(a) upper panel]. However, the phase-sensitive nature of frequency conversion

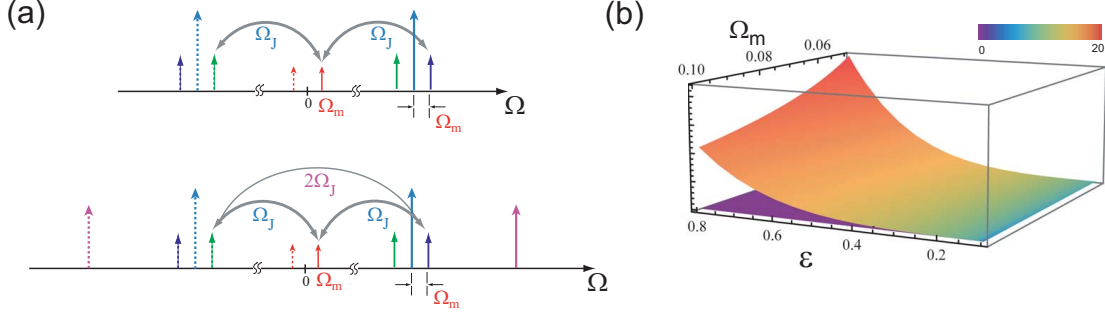


Figure 3.6: **Symmetry breaking in frequency conversion by an RSJ.** (a) Various frequency mixing processes in the presence of Josephson frequency (upper panel) and in the presence of one additional Josephson harmonic (lower panel) ( $K=1, N=1$ ). In the first case three-wave mixing leads to symmetric frequency conversion between the signal frequency ( $\omega_m$ ) and sidebands ( $\omega_{\pm}$ ). The second case involves simultaneous three and four wave mixing, the latter performed by the second Josephson harmonic ( $K=2, N=1$ ). (b) Asymmetry in frequency conversion parametrized as  $(|t_u|^2 + |s_u|^2) - (|t_d|^2 + |s_d|^2)$  for the two cases discussed above, as a function of input frequency and bias parameter  $\varepsilon$ . The lower surface plot (corresponding to the *case I*) shows zero asymmetry while the upper surface plot (corresponding to the *case II*) shows a strongly nonreciprocal frequency upconversion as the input frequency  $\Omega_m$  approaches zero and bias current  $I_B$  is decreased towards the junction critical current  $I_0$  (or  $\varepsilon$  increases).

in terms of distinct preferred quadratures for upconversion ( $I$ ) and downconversion ( $Q$ ) is still preserved (also see Fig. C.2 in Appendix C).

- *Case II*: On including one additional Josephson harmonic [ $K = 2$ ], we find that the presence of off-diagonal elements in  $Y$  leads to additional mixing of sidebands by the second Josephson harmonic [Fig. 3.6(a) lower panel] given by the matrix element

$$v_{\pm\mp} = \pm \frac{\varepsilon^2}{2\Omega_m} \sqrt{\frac{1 \pm \Omega_m}{1 \mp \Omega_m}}. \quad (3.37)$$

Furthermore, in this case, the scattering is nonreciprocal i.e.  $\mathbb{S}^T \neq \mathbb{S}$  [Fig. 3.6] as the matrix elements for up- and downconversion in a certain temporal

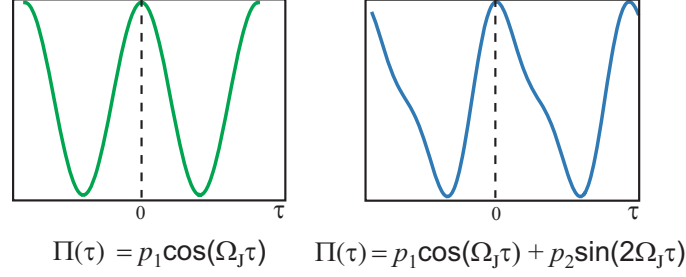


Figure 3.7: **Monochromatic vs colored (multiharmonic) pumps.** Pump configurations for the two cases discussed in Fig. 3.6, plotted as a function of dimensionless time  $\tau = \omega_B t$ . The presence of second Josephson harmonic ( $2\Omega_J$ ), phase shifted by 90 degrees with respect to the first harmonic ( $\Omega_J$ ), breaks the temporal symmetry of the pump  $\Pi(t)$  and makes it asymmetric about  $\tau = 0$ .

channel cease to be equal,

$$t_d \neq t_u; \quad s_d \neq s_u \quad (3.38)$$

with

$$t_d = \frac{-i\varepsilon}{\sqrt{\Omega_m(1 + \Omega_m)}} \left[ 1 + \frac{\varepsilon^2}{4} \left( \frac{1 - \Omega_m}{1 + \Omega_m} \right) \right] \quad (3.39a)$$

$$t_u = \frac{-i\varepsilon}{\sqrt{\Omega_m(1 + \Omega_m)}} \left[ 1 + \frac{\varepsilon^2}{4} \left( \frac{3 + \Omega_m^2}{1 - \Omega_m^2} \right) \right] \quad (3.39b)$$

$$s_d = \frac{i\varepsilon}{\sqrt{\Omega_m(1 - \Omega_m)}} \left[ 1 + \frac{\varepsilon^2}{4} \left( \frac{1 + \Omega_m}{1 - \Omega_m} \right) \right] \quad (3.39c)$$

$$s_u = \frac{i\varepsilon}{\sqrt{\Omega_m(1 - \Omega_m)}} \left[ 1 + \frac{\varepsilon^2}{4} \left( \frac{3 + \Omega_m^2}{1 - \Omega_m^2} \right) \right]. \quad (3.39d)$$

The scattering coefficients are correct up to  $\mathcal{O}(\varepsilon^4)$  and the  $\mathbb{S}$  matrix is symplectic up to  $\mathcal{O}(\varepsilon^5)$ . It is interesting to note that the reflection coefficients reported in Eqs. (3.36)[(a)-(c)] hold good up to  $\mathcal{O}(\varepsilon^4)$ . The essence of symmetry breaking in *case II* lies in the fact that the presence of second Josephson harmonic leads to a skewed effective pump seen by the junction, such that  $\Pi(t \pm T/2) \neq -\Pi(t)$

(Fig. 3.7). Systems exposed to such biharmonic drives ( $\xi = t$ ) and potentials ( $\xi = x$ ), popularly known as ratchets,

$$p^x \cos(\omega\xi) + p^y \sin(2\omega\xi) \quad (3.40)$$

have been shown to exhibit a variety of symmetry breaking phenomena such as rectification [Flach et al., 2000], directed electron or particle transport (see [Hanggi and Marchesoni, 2009] for a comprehensive review). Thus the preferred upconversion of photons from low to high frequency, as shown in Fig. 3.6(b) is an analogous demonstration of ratchet physics in frequency domain. The significance of higher pump harmonics in such symmetry breaking is also indicated by the degree of terms that contribute to asymmetry between up- and downconversion in Eq. (3.39); we see from Eqs. (3.39) that the leading order asymmetric term in matrix  $\mathbb{S}_a$  is of order  $\varepsilon^3$  — this originates from sideband mixing mediated by the second Josephson harmonic with strength  $\varepsilon^2$  [see Eq. (3.24)] combined with up/downconversion with strength  $\varepsilon$ .

### 3.3 Fluctuation Spectrum of the RSJ

In this section, we evaluate the noise spectrum of the RSJ. For this purpose, we consider the admittance matrix derived for the junction in Eq. (3.32). The total admittance matrix ( $\mathbb{Y}_T$ ) may be calculated as:

$$\mathbb{Y}_T = (1 + \mathbb{Y}_J) \quad (3.41)$$

where  $\mathbb{Y}_J$  is normalized with respect to the characteristic admittance  $Z_C^{-1} = R^{-1}$  corresponding to the shunt. We can, hence, obtain the total impedance matrix of

the RSJ,  $\mathbb{Z}_T$  as,

$$\mathbb{Z}_T = \frac{1}{\det[\mathbb{Y}_T]} \begin{pmatrix} 1 & \frac{-i\varepsilon}{2(1+\Omega_m)} & \frac{-i\varepsilon}{2(1-\Omega_m)} \\ \frac{-i\varepsilon}{2\Omega_m} & 1 & 0 \\ \frac{i\varepsilon}{2\Omega_m} & 0 & 1 \end{pmatrix}, \quad (3.42)$$

where we have only considered terms to first order in  $\varepsilon$ . We consider the first row of  $\mathbb{Z}_T$  which gives the impedance contribution at the signal frequency  $\omega_s$ . We note that

$$(\det[\mathbb{Y}_T])^{-1} = \left(1 - \frac{\varepsilon^2}{2(1 - \Omega_m^2)}\right)^{-1} \quad (3.43)$$

$$= 1 + \frac{\varepsilon^2}{2} + \mathcal{O}(\varepsilon^4), \quad (3.44)$$

which corresponds to the dynamic resistance across the junction. This can be seen from the fact that, up to the first order in perturbation, we have

$$\begin{aligned} R^{-1}R_{\text{Dyn}} &= R^{-1} \frac{d\omega_J}{d\omega_B} = R^{-1} \frac{d\omega_J}{d\varepsilon} \frac{d\varepsilon}{d\omega_B} \\ &= 1 + \frac{\varepsilon^2}{2}. \quad [\text{from Eq. (3.17)}], \end{aligned} \quad (3.45)$$

Thus, we can now write the spectrum of voltage fluctuations for the RSJ, in the limit of zero signal frequency ( $\Omega_m \rightarrow 0$ ) simply as:

$$\begin{aligned} S_{VV}[\omega_m] &= |z_{00}|^2 S_{II}[\omega_m] + |z_{0+}|^2 S_{II}[\omega_J + \omega_m] \\ &\quad + |z_{0-}|^2 S_{II}[-\omega_J + \omega_m] \end{aligned} \quad (3.46)$$

$$\begin{aligned} &= \left[ S_{II}[\omega_m] + \frac{\varepsilon^2}{4} (S_{II}[\omega_J] + S_{II}[-\omega_J]) \right] R_{\text{Dyn}}^2 \\ &= \left[ \frac{2k_B T}{R} + \frac{I_0^2}{I_B^2} \frac{\hbar\omega_J}{2R} \coth\left(\frac{\hbar\omega_J}{2k_B T}\right) \right] R_{\text{Dyn}}^2 \end{aligned} \quad (3.47)$$

where in the second step we have used the coefficients in the second row of  $Z_T$  calculated in Eq. (3.42) and the identity  $S_{II}[\omega] + S_{II}[-\omega] = 2\bar{S}_{II} = 2R^{-1}\hbar\omega \coth(\hbar\omega/2k_B T)$  [Clerk et al., 2010]. Equation (3.47) is a well known result which shows that the noise appearing near dc in the RSJ involves two contributions: (i) a direct contribution from the input Johnson noise of the resistor and, (ii) noise that is down-converted from the Josephson harmonics and appears at the input. The second contribution is appropriately weighted by a bias-dependent factor  $\varepsilon^2$ . This can be easily understood in the scattering formalism presented here: the strength of the internally generated Josephson frequency is solely determined by the bias condition [see Eq. (3.24)] and this acts as the pump used to perform the mixing down of the high frequency noise. The downconverted amplitude scales directly with the pump strength, a result well known in parametric literature, and hence the intensity of the noise fluctuations which scale as the square of the amplitude are weighted by  $\varepsilon^2$ . This is not a nonreciprocal effect, which would be of order  $\varepsilon^6$  [coming from the  $\varepsilon^3$  term in scattering coefficients calculated in Eq. (3.39)] and needs further investigation.

### 3.4 Discussion

In this chapter, we performed a first principles analysis of the rf properties of a resistively-shunted Josephson junction (RSJ) biased in the voltage state. This was accomplished by using a generalized input-output description that allowed us to self-consistently evaluate the Josephson oscillation and its harmonics as a series in a small external bias parameter (here  $\varepsilon = I_0/I_B < 1$ ). Using this method we first demonstrated that the series of Josephson harmonics generated in the voltage regime have alternate odd and even harmonics phase-shifted by  $\pi/2$ . On identifying this harmonic series as the effective ‘pump’ for usual parametric mixing of a small frequency signal performed by the junction, we established that the

presence of higher pump harmonics leads to a symmetry breaking in frequency conversion. The emergence of dynamical nonreciprocity in this regime for the RSJ has remained hitherto unexplored to the best of our knowledge.

Further, in analogy with ratchet physics, the preferred direction of frequency conversion (up- or down-) is governed by the relative phase between the successive harmonics and the fundamental pump tone (Josephson oscillation in our case). The maximum asymmetry in conversion is obtained when the relative phase between harmonics is  $\pi/2$ , as is shown to be the case for the RSJ. One way of understanding this phenomena is to note that the phase asymmetry in up- and downconversion prevalent at even first order in Eq. (3.36), when combined with a second order mixing process, can lead to an interferometric reinforcement of scattering into a preferential frequency channel as shown in Fig. 3.6(a). This generic protocol of phase-shifted biharmonic pumping can be employed in the conventional externally pumped parametric devices such as optomechanical devices [Teufel et al., 2008], optical parametric amplifiers, and MEMS to realize a new regime of nonreciprocal operation. The neat part about the nonreciprocal photon shuttling scheme discussed here is that it is *not* based on an symmetry in photon population at two different frequencies arising due to quantum mechanics but goes beyond it and can be implemented in a completely classical setting too.

We also derived the full fluctuation noise spectrum for the RSJ. This may prove to be important in designing future devices by filtering the spectrum appropriately to have maximum gain without introducing additional noise downconverted from higher harmonics. In addition, the device shows gain in reflection [ $r_m > 1$  in Eq. (3.35)] but with a concomitant increase in the voltage fluctuations; this is because the low frequency signal channel collects downconverted noise from modes near Josephson harmonics. It may be possible to route noise away from the desired frequency channels by exploiting asymmetric frequency conversion. Thus

realization of a finite gain with suppressed downconversion of noise appearing at the input, by imposing a definite phase relationship between various harmonics of the drive, may provide us a way to realize a reflection-based amplifier using the RSJ. For such a device, the reactance appearing at the RF needs to be carefully designed to ensure a small linewidth of the Josephson oscillations and hence minimize the contribution of the broadband noise floor.

---

# Directional Amplification: Nonreciprocity with gain

---

*“From error to error, one discovers the entire truth.”*

— Sigmund Freud

In the previous chapters, we considered the case of nonreciprocity in spatial channels (a.k.a circulator) or temporal channels (asymmetric frequency conversion such as that discussed in the context of a current biased RSJ). While a monochromatic pump tone with phase gradient in space is required for the former, the latter can be realized using a multi-tone carrier pumping the mixing medium. In this chapter, we will show how using both these ideas directional operation with gain can be realized. As a specimen of this confluence, we will analyze the microwave SQUID amplifier (MWSA) based on dc SQUID — a device ubiquitous in superconducting community for almost half a century. Besides providing the nucleus of the MWSA which we discuss in detail here, the dc SQUID (Superconducting QUantum Interference Device) has enabled a broad range of devices, including magnetometers, gradiometers, voltmeters and susceptometers [Clarke and Braginski, 2004, 2006]. Most of these devices are used at relatively low frequencies, and all have the common feature of offering extremely low noise operation [Tesche and

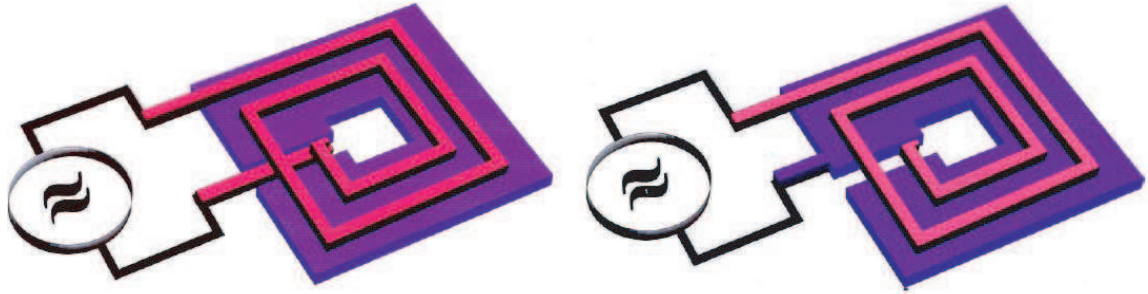


Figure 4.1: **Microstrip design of the SQUID.** (a) Conventional SQUID amplifier (b) Microstrip SQUID amplifier (MSA). The microstrip geometry in MSA helps prevent a reduction in gain due to parasitic capacitance.

[Clarke, 1977]. The fact that the dc SQUID is potentially a quantum limited amplifier in the microwave regime was recognized long ago [Koch et al., 1981], but not exploited in practice until the Axion Dark Matter eXperiment (ADMX) provided a powerful motivation [Bradley et al., 2003]. This need led to the development of the Microstrip SQUID Amplifier (MSA, Fig. 4.1) in which the input coil deposited on (but insulated from) the washer of a SQUID acts as a resonant microstrip [Mück et al., 1998]. Such amplifiers have achieved a noise temperature within a factor of two of the standard quantum limit [Caves, 1982; Mück et al., 2001; Kinion and Clarke, 2011]. More recently, new designs have appeared intended to extend the frequency of operation to frequencies as high as 10 GHz, aimed at the readout of superconducting qubits [Hoffman et al., 2011] and the detection of micromechanical motion [Etaki et al., 2008]. These include incorporation of a gradiometric SQUID at the end of a quarter wave resonator [Spietz et al., 2008] and the direct injection of the microwave signal from a quarter wave resonator into one arm of the SQUID ring [Ribeill et al., 2011; Hover et al., 2012].

Besides having desirable properties such as high gain, wide bandwidth and near quantum-limited operation, microwave SQUID amplifiers (MWSAs) — unlike conventional Josephson parametric amplifiers [Castellanos-Beltran and Lehnert, 2007; Yamamoto et al., 2008; Bergeal et al., 2010a; Vijay et al., 2009; Metcalfe

[et al., 2007](#)] — also offer an intrinsic separation of input and output channels of the signal that makes them unique among amplifiers based on Josephson tunnel junctions. They would be especially well suited as a preamplifier in the measurement chain for superconducting devices by eliminating the need for channel separation devices, such as circulators and isolators, between the sample under test and the first amplification stage. Although MWSAs have been successfully used experimentally, questions pertaining to their nonlinear dynamics and ultimate sensitivity as amplifiers have continued to remain challenging problems. Previous theories include quantum Langevin simulations [[Koch et al., 1981](#); [Danilov et al., 1983](#)] and treatment of the SQUID as an interacting quantum point contact [[Clerk, 2006](#)]. The ultimate exploitation of the amplifier, however, requires a deeper understanding of its behavior at the Josephson frequency and its harmonics. Besides being valuable for practical considerations, such understanding may help discern the cause of intrinsically nonreciprocal operation of the MWSA that has hitherto remained an open question. This concern is especially relevant to applications such as qubit readout where the amplifier backaction may prove to be the Achilles' heel. In this work, we develop an ab-initio theoretical framework to understand the high frequency dynamics of the SQUID in detail. In addition to giving us crucial insights into the amplifying mechanism of the MWSA and its nonreciprocal response between the input and output signal channels, this approach enables us to calculate the experimentally relevant quantities such as available gain, added noise and directionality at operating frequencies of interest. We will begin by reviewing the basics of the SQUID circuit.

## 4.1 Analytically Solvable Model for the dc SQUID

In this section we present the details of the harmonic balance treatment of the MWSA. The dc SQUID is biased in the voltage regime — in contrast to the usual

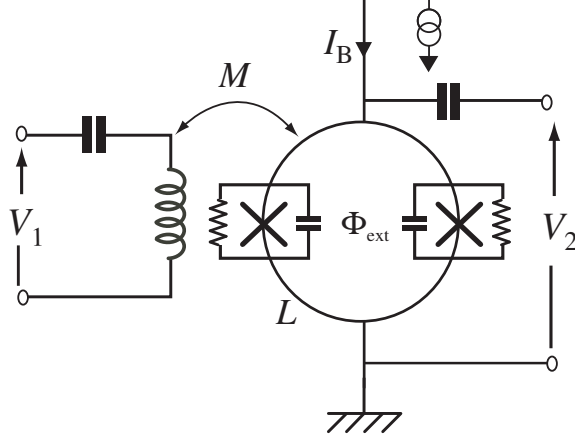


Figure 4.2: **Circuit schematic of a conventional MWSA.** The SQUID consists of two Josephson junctions, arranged in a superconducting loop, with inductance  $L$ . The loop is biased using a static current source  $I_B$  and an external flux  $\Phi_{\text{ext}}$ . An input voltage  $V^1$  generates an oscillating current in an input coil inductively coupled to the SQUID thus inducing a small flux modulation  $\delta\Phi$  of the flux enclosed by the loop. For optimal flux bias [ $\Phi_{\text{ext}} = (2n + 1)\Phi_0/4$ ] that maximizes the flux-to-voltage transfer coefficient  $V_\Phi \equiv (\partial V^2/\partial\Phi_{\text{ext}})_{I_B}$ , this causes a large output voltage  $V^2 = V_\Phi\delta\Phi$  to develop across the ring. Thus the device behaves as a low impedance voltage amplifier.

Josephson parametric amplifiers operated in the zero voltage state with the phase excursions of the Josephson junction confined to a single cosine well — and has the dynamics of a particle sampling various wells of a two-dimensional tilted washboard [Clarke and Braginski, 2004] which is kind of a *curved egg crate* (Fig. 4.3).

$$\frac{U_{\text{SQUID}}}{2E_J}(\varphi^D, \varphi^C) = \frac{1}{\pi\beta_L} \left( \varphi^D - \frac{\varphi_{\text{ext}}}{2} \right)^2 - \cos \varphi^D \cos \varphi^C - \frac{I_B}{2I_0} \varphi^C. \quad (4.1)$$

The presence of a dc bias current  $I_B$  greater causes a tilt while imposing an external flux in the loop  $\varphi_{\text{ext}} = 2\pi\Phi_{\text{ext}}/\Phi_0$  shifts the position of maxima and minima of the cosine term in the potential. Here  $I_0$  is the critical current of each junction,  $\beta_L \equiv 2LI_0/\Phi_0$  denotes a dimensionless parametrization of the SQUID loop inductance and  $\Phi_0 = h/2e$  is the flux quantum. Also  $E_J$  represents the Josephson energy and  $I_0$  denotes the critical current of each junction. We have introduced the common,  $\varphi^C = (\varphi^L + \varphi^R)/2$ , and differential,  $\varphi^D = (\varphi^L - \varphi^R)/2$ , mode combinations of

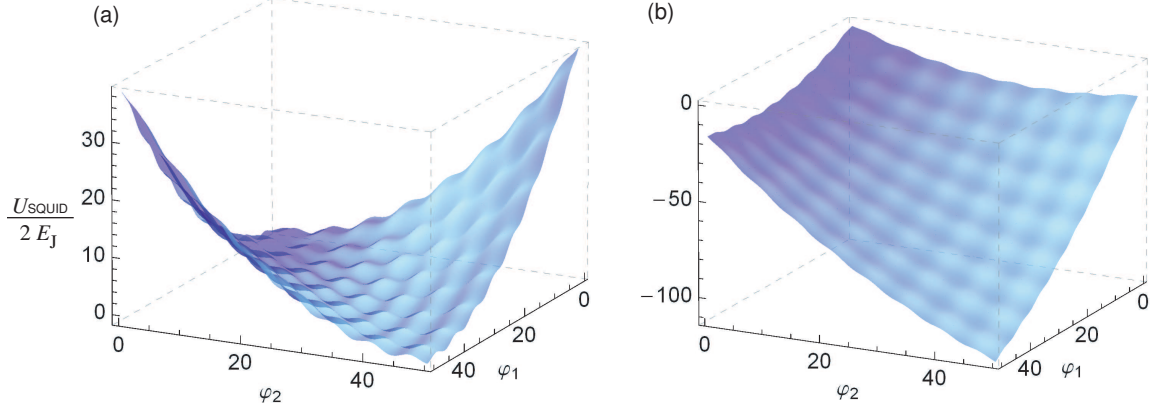


Figure 4.3: **SQUID potential profile.** The SQUID potential plotted as a function of phases of the two junctions  $\varphi^{L,R}$  for (a)  $I_B = 0$  and  $\varphi_{\text{ext}} = 0$ . (b)  $I_B = 2.2I_0$  and  $\varphi_{\text{ext}} = 0$ . Here  $\beta_L = 5$ .

the phases of two junctions that form the axes of the two-dimensional orthogonal coordinate system.

For the purpose of our analysis, we consider the circuit in Fig. 4.4(a). The key idea is to treat the SQUID like a parametric frequency converter, pumped by a carrier which is a combination of different Josephson harmonics generated due to the evolution of the “phase” particle in the running state of the device. We perform our analysis in the paradigm of input-output theory (Appendix B), generalized to take into account the phase running in the 2D tilted washboard. In the spirit of the input-output analysis of the circuit, we replace the resistive shunts across the junction with semi-infinite transmission lines [cf. Fig. 4.4(b)] of characteristic impedance  $Z_C = R$ , following the Nyquist model of dissipation. Thus the shunts play the dual role of dissipation as well as that of the ports (or channels) used to address and drive the device. This allows us to switch from a standing mode representation in terms of lumped element quantities such as voltages and currents to a propagating wave description in terms of signal waves travelling on the transmission lines. The amplitude of these waves is given by the

well known input-output relation [Yurke, 2004],

$$A_i^{\text{in/out}}(t) = \frac{V^i}{2\sqrt{Z_C}} \mp \frac{\sqrt{Z_C}I^i}{2}; \quad i \in \{L, R\}. \quad (4.2)$$

where  $V^i$  and  $I^i$  denote the voltage across the shunt resistance and current flowing in the shunt resistance respectively. From Eq. (4.1), we can write down the common mode current,  $I^C = (I^L + I^R)/2$ , and differential mode current,  $I^D = (I^L - I^R)/2$ , flowing in the shunts by identifying  $\varphi^{C,D}$  as the relevant position variables. The current in each mode can thus be interpreted as the “force” [Devoret, 1995] that follows directly from the Hamilton’s equation of motion as

$$\frac{I^{C,D}}{I_0} = \frac{\partial}{\partial \varphi^{C,D}} \left( \frac{U_{\text{SQUID}}}{E_J} \right), \quad (4.3)$$

which yields

$$\widehat{\omega}^C = \frac{\omega_B}{2} - \omega_0 \sin \varphi^C \cos \varphi^D \quad (4.4a)$$

$$\widehat{\omega}^D = \frac{\omega_0}{\pi\beta_L} (-2\varphi^D + \varphi_{\text{ext}}) - \omega_0 \cos \varphi^C \sin \varphi^D. \quad (4.4b)$$

Here we have expressed the currents in equivalent energy units,

$$\widehat{\omega}^C \equiv \frac{I^C R}{\varphi_0}; \quad \widehat{\omega}^D \equiv \frac{I^D R}{\varphi_0} \quad (\text{currents}) \quad (4.5)$$

$$\omega_B \equiv \frac{I_B R}{\varphi_0}; \quad \omega_0 \equiv \frac{I_0 R}{\varphi_0} \quad (\text{characteristic currents}), \quad (4.6)$$

with  $\varphi_0 = \Phi_0/(2\pi)$ . Including a capacitance across the junction gives an additional term, involving a second-order derivative of the common and differential mode fluxes, of the form  $-\omega_B \Omega_c \ddot{\varphi}^{C,D}$  with  $\Omega_c = 2\pi I_B R^2 C / \Phi_0$ , on the right-hand side of Eq. (4.4). This parametrization of capacitance, motivated by calculational simplicity, leads to a plasma frequency ( $\omega_{pl} \equiv (I_0/\varphi_0 C)^{1/2}$ ) that decreases with decreasing

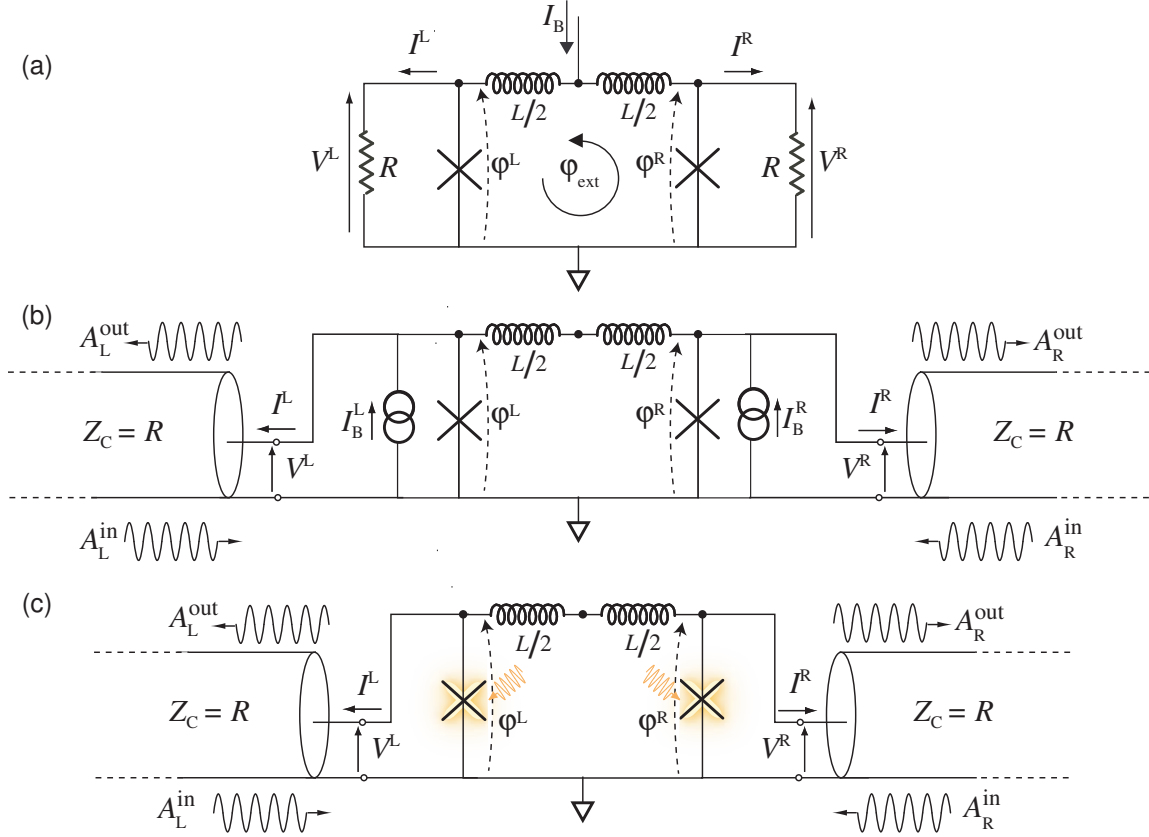


Figure 4.4: **Equivalent input-output model of the SQUID.** (a) The bare SQUID loop without the input coupling circuit. As noted in Fig. 4.2, the circuit has two static biases - a common mode bias current  $I_B$  and a differential mode external flux  $\Phi_{\text{ext}}$ . There is also a capacitance  $C$  across each junction, not shown here for simplicity. (b) Equivalent SQUID circuit under Nyquist representation of shunt resistances and separate static current biases  $I_B^L$  and  $I_B^R$  for each junction. The common mode bias current  $I_B$  now corresponds to the even combination of two external bias currents  $-(I_B^L + I_B^R)/2$  while the external flux  $\Phi_{\text{ext}}$  corresponds to the differential combination of the two current sources  $L(I_B^L - I_B^R)/2$ . The oscillating signals are modelled as incoming and outgoing waves travelling on semi-infinite transmission lines, representing the shunt resistances across the two junctions. (c) Effective junction representation for evaluating the signal response of the device. Here, we have replaced the junctions biased with a static current with effective junctions pumped by the Josephson harmonics (represented by a “glowing” cross with a pumping wave) generated by phase running in the voltage state of the junction.

bias current towards  $I_0$ . The more conventional parametrization which maintains a constant plasma frequency for all values of bias currents can be implemented in

a more comprehensive calculation aided by numerical techniques.

Equation (4.4) represents a subtle current-phase relationship for the two junction system, analogous to the first Josephson relation. We note that Eq. (4.4) can alternatively be derived using a first-principle Kirchhoff's law analysis of the circuit in Fig. 4.4(a). Similar to the currents, we can define the common and differential mode voltages as,

$$\check{\omega}^C \equiv \frac{V^C}{\varphi_0}; \quad \check{\omega}^D \equiv \frac{V^D}{\varphi_0}. \quad (4.7)$$

We note that the usual mode of operation of a dc SQUID involves an input flux inductively coupled using an input transformer of which the loop inductance forms one of the coils (Fig. 4.2). The input transformer, however, is an empirical artifact required to ensure the impedance matching with the input impedance of the SQUID at a desired frequency. It is not crucial from the point of view of device characteristics, however, as it is the SQUID which provides amplification and all the relevant nonlinear dynamics of the device. In the ensuing analysis we do not employ a separate input port, but rather consider a direct input coupling through the differential mode of the ring which couples to the flux in an analogous manner [Fig. 4.4(b)]. Such a scheme may also prove beneficial for a practical device to overcome the problem of low coupling at high signal frequencies, as recently shown experimentally using a SLUG (Superconducting low-inductance undulatory galvanometer) microwave amplifier [Ribeill et al., 2011; Hover et al., 2012]. We shall revisit the question of de-embedding the SQUID circuit impedance, as seen from a matched input port, while calculating the power gain of the device in sec. 4.3.

### 4.1.1 Harmonic balance treatment

Using the input-output relation of Eq. (4.2) with Eqs. (4.4) and (4.7), we obtain the equations

$$\check{\omega}^{C,D}(t) = \widehat{\omega}^{C,D}(t) + 2\omega^{\text{in}C,D}(t). \quad (4.8)$$

for common and differential mode circuit quantities. We perform our analysis in the paradigm of input-output theory and employ the method of harmonic balance to study the driven dynamics of the device. Since the dc SQUID is biased in the voltage regime — in contrast to the usual Josephson parametric amplifiers operated in the zero voltage state with the phase excursions of the Josephson junction confined to a single cosine well — the input-output analysis thus needs to be generalized to take into account phase running evolution in this two-dimensional potential. We account for the non-zero velocity of the phase particle by assuming two parts to its solution for each variable of interest ( $\varphi^C$  and  $\varphi^D$ ),

$$\varphi^C = \omega_J t + \delta\varphi^C(t) \quad (4.9)$$

$$\varphi^D = \phi_0 + \delta\varphi^D(t), \quad (4.10)$$

where  $\omega_J t$  and  $\phi_0$  represent the average static values of the common and differential mode phases [cf. Eq. (4.14)]. Just as in the case of RSJ discussed in section 3.2.1, we separate the time-varying perturbative components  $\delta\varphi^C(t)$  into two parts:

$$\delta\varphi^{C,D}(t) = \Pi^{C,D}(t) + \Sigma^{C,D}(t). \quad (4.11)$$

Here  $\Pi^{C,D}(t)$  refer to the components at Josephson frequency  $\omega_J$  and its harmonics associated with each of the spatial modes  $C$  and  $D$ . The term  $\Sigma^{C,D}(t)$  includes the components oscillating at signal frequency  $\omega_m$  and the resultant sidebands

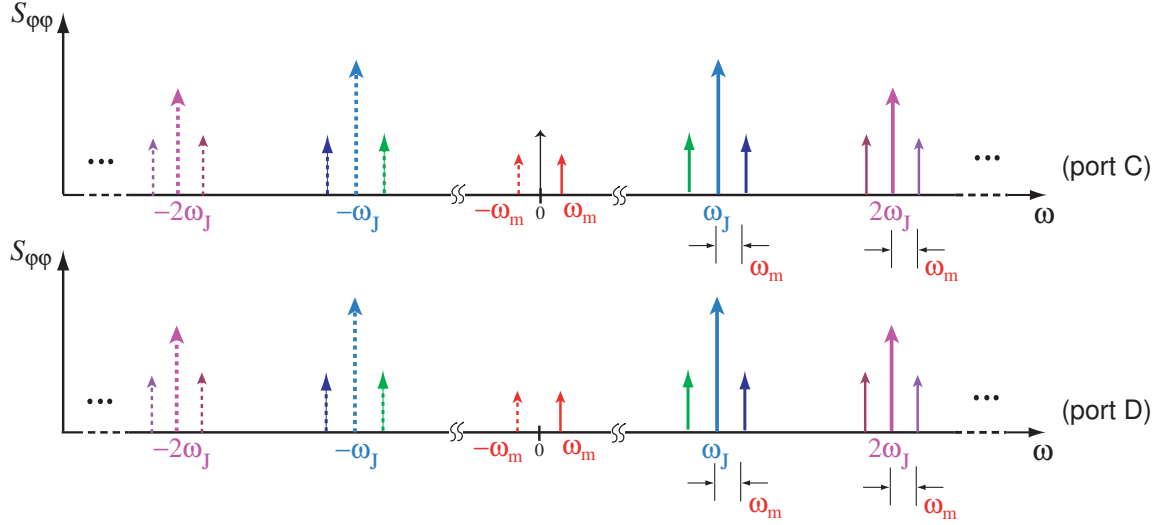


Figure 4.5: **Frequency landscape of common and differential modes of the SQUID.** The solid and the dashed arrows represent different frequencies and respective conjugates. The tall arrows show the Josephson harmonics generated internally in the running state of the device. The small input signal frequency  $\omega_m$  and different sidebands generated by mixing with Josephson harmonics are shown with shorter arrows. In the common mode the black arrow at zero frequency denotes the external dc bias.

$\omega_n = n\omega_J + \omega_m$  generated by wave mixing via the nonlinearity of the SQUID:

$$\Pi^{C,D} = \sum_{k=1}^K p_k^{x,(C,D)} \cos k\omega_J t + p_k^{y,(C,D)} \sin k\omega_J t \quad (4.12)$$

$$\Sigma^{C,D} = \sum_{n=-N}^{+N} s_n^{x,(C,D)} \cos(n\omega_J + \omega_m)t + s_n^{y,(C,D)} \sin(n\omega_J + \omega_m)t. \quad (4.13)$$

Such an approach allows us to perform a self-consistent determination of the working point of the device established by static bias parameters (the static bias current  $I_B$  and external flux  $\Phi_{\text{ext}}$  shown in Fig. 4.2). This involves deriving the response of the SQUID at zero frequency and at the Josephson oscillation frequency  $\omega_J$ , which are intimately related through the second Josephson relation

$$\langle \tilde{\omega}^C \rangle = V_{dc}/\varphi_0 = \omega_J, \quad (4.14)$$

where  $V_{dc}$  is the static voltage that develops across the SQUID loop biased in the running state. We note that the number of Josephson harmonics included in the analysis [i.e.  $K$  in Eq. (4.12)] is determined by the order of expansion of the junction nonlinearity in  $\delta\varphi$ . This in turn is determined by the bias condition of the device set by the bias current  $I_B$ . Analogous to the RSJ case (cf. Fig. 3.3), as  $I_B$  is reduced towards  $I_0$ , the characteristics of the device become increasingly nonlinear and higher Josephson harmonics become more significant. We can, therefore, calculate the response perturbatively by expanding each of the coefficients  $p$  and  $s$  in Eqs. (4.12)-(4.13) as a truncated power series in the reduced bias parameter

$$\varepsilon \equiv \frac{I_0}{I_B} = \frac{\omega_0}{\omega_B}. \quad (4.15)$$

The degree of the resultant polynomial evaluation of  $p$ ,  $s$  coefficients is set by the desired order of expansion in  $\delta\varphi$ . As  $\varepsilon \leq 0.5$  (or equivalently  $I_B > 2I_0$ ) for the SQUID to operate in the running state at any value of flux bias [Clarke and Braginski, 2004], which is the regime of interest for the SQUID to be operated as a voltage amplifier, it provides a convenient small parameter of choice ensuring rapid convergence of the perturbation series method. Furthermore this parameter serves as the effective strength of the different Josephson harmonics which play a role analogous to the strong “pump” tone of conventional parametric amplifiers [Bergeal et al., 2010a].

## 4.2 Calculation of SQUID Dynamics

### 4.2.1 Steady state response: I–V characteristics

We first derive the response at zero frequency and at the Josephson oscillation frequency  $\omega_J$  in a self-consistent manner. The analysis is exactly on the lines out-

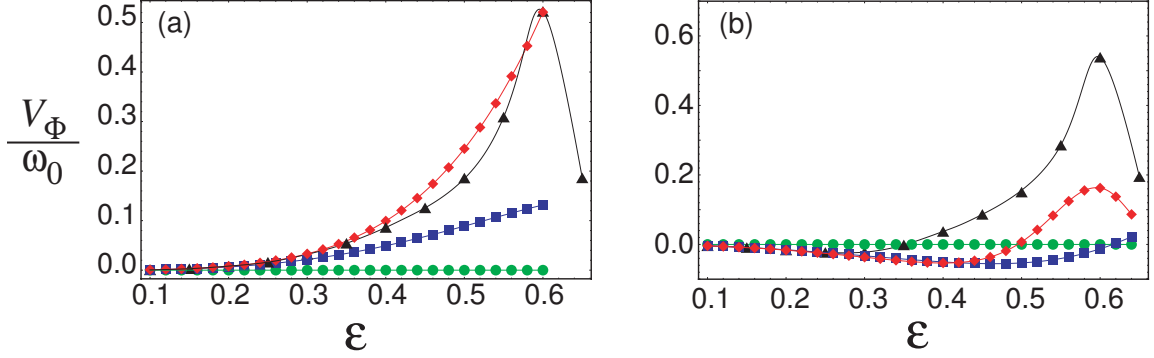


Figure 4.6: **Static transfer function of the SQUID** calculated as a function of two bias parameters  $\varepsilon = \omega_0/\omega_B$  at  $\varphi_{\text{ext}} = \pi/2$  ( $\Phi_{\text{ext}} = \Phi_0/4$ ) for (a) strongly overdamped ( $\Omega_C = 0$ ) and (b) intermediately damped junctions ( $\Omega_C = 1$ ). The (black) triangles represent the transfer function calculated from the exact numerical integration of the SQUID equations. The (green) circles correspond to the  $K = 1$  evaluation including only the Josephson frequency [ Eq. (4.12)]. This first order evaluation does not show any voltage modulation with flux as there is no coupling between the common and differential modes at this order. The (blue) squares and (red) diamonds correspond to an evaluation including the second ( $K = 2$ ) and third Josephson ( $K = 3$ ) harmonic respectively. The corresponding curves represent interpolating polynomials. In both plots, the agreement of the perturbative series with exact numerical solution improves on including higher order corrections corresponding to contributions of higher Josephson harmonics.

lined in section 3.2.1 but now instead of a single spatial mode we have two spatial modes — common and differential. As before, we self-consistently evaluate the working point of the SQUID in steady state along with the strength of the various Josephson harmonics. This is done assuming no oscillating input drive at the Josephson frequency and its harmonics. We obtain a set of boundary conditions of the form

$$\check{\omega}[k\omega_J] - \hat{\omega}[k\omega_J] = 0 \quad k \in [0, K]. \quad (4.16)$$

We solve this set of simultaneous equations to calculate the strength of the various Josephson harmonics generated internally from the static bias due to the junction nonlinearity along with the zero frequency characteristics. Figure 4.6 shows

a plot of static transfer function  $v_\Phi = \partial\langle\omega^C\rangle/\partial\varphi_{ext}$  obtained using perturbative series method to determine the coefficients  $p_k^{C,D}$  [Eq. (4.12)], as described in the section 3.2.1 for RSJ case. The agreement between the exact numerical calculation and perturbative analytical calculation improves on increasing the order of the perturbation series evaluation by including mixing processes mediated by higher Josephson harmonics. Further, from the differential mode dc calculation, we obtain a relation for the steady state phase angle between the two junctions in the ring as,

$$\phi_0 = \frac{\varphi_{ext}}{2} + \beta_L \sum_{k \geq 2}^K c_k \varepsilon^k \sin \varphi_{ext}, \quad (4.17)$$

where the coefficients  $c_k$  are of order unity. Thus, we see that the average values of both the explicit dc bias parameters namely  $\varepsilon$  (common) and  $\varphi_{ext}$  (differential) participate in establishing each of the implicit dc biases –  $V_{dc}$  (or equivalently  $\omega_J$ ) for the common mode and  $\phi_0$  for the differential mode. The contributions arising from the bias current, as shown in Eq. (4.17), lead to a rolling of the static phase difference along the SQUID loop that manifests itself as the change in curvature of the transfer function curves shown in Fig. (4.6). Furthermore we note that, as indicated by the steady state calculation, the flux dynamics of  $v_\Phi$  evaluated using the truncated harmonic series calculation are ‘slower’ or shift to higher values of bias with respect to the exact numerical results. Nonetheless, the predicted magnitudes are comparable and hence the theory is capable of making semi-quantitative predictions in an analytically tractable manner. The major merit of this approach over conventional methods lies in the natural extension offered for the study of higher frequency dynamics as discussed in the following sections.

## 4.2.2 Steady state response: Josephson harmonics

On solving the set of equations represented by Eq. (4.16) at Josephson frequency and its harmonics, we find that for zero (or integer) flux quanta in the loop,  $\Phi_{\text{ext}} = 0$ ,

$$\Pi^C(t) = \sum_{k=1}^K f^C(\varepsilon) \cos(k\omega_J t) + g^C(\varepsilon) \sin(k\omega_J t) \quad (4.18a)$$

$$\Pi^D(t) = 0, \quad (4.18b)$$

i.e. there is no coupling between the common  $C$  and differential  $D$  modes of the device, as also corroborated by Fig. 4.7(a) where no movement along the differential coordinate ( $2\varphi^D = \varphi^L - \varphi^R$ ) takes place as the particle moves along ( $2\varphi^C = \varphi^L + \varphi^R$ ). On the other hand, for  $\Phi_{\text{ext}} = \Phi_0/2$ , though the particle undergoes a zig-zag motion in the potential coupling  $C$  and  $D$ , due to symmetry of the trajectory shown in Fig. 4.7(c), only even harmonics of the Josephson oscillation are generated in the common ( $C$ ) mode and only odd harmonics are generated in the differential ( $D$ ) mode

$$\Pi^C(t) = \sum_{k=1}^K f^C(\varepsilon) \cos(2k\omega_J t) + g^C(\varepsilon) \sin(2k\omega_J t) \quad (4.19a)$$

$$\Pi^D(t) = \sum_{k=1}^K f^D(\varepsilon) \cos[(2k-1)\omega_J t] + g^D(\varepsilon) [\sin(2k-1)\omega_J t]. \quad (4.19b)$$

Here  $f^{C,D}(\varepsilon)$  and  $g^{C,D}(\varepsilon)$  are polynomial functions of reduced bias parameter  $\varepsilon$ . For quarter flux in loop,  $\Phi_{\text{ext}} = \Phi_0/4$ , in addition to coupling between the  $C$  and  $D$  modes, there is an asymmetry in the trajectory in the SQUID potential [reflected, for instance, in the relative size of contours around minima shown in Fig. 4.7(b)]. This leads to generation of both odd and even harmonics in each of the common

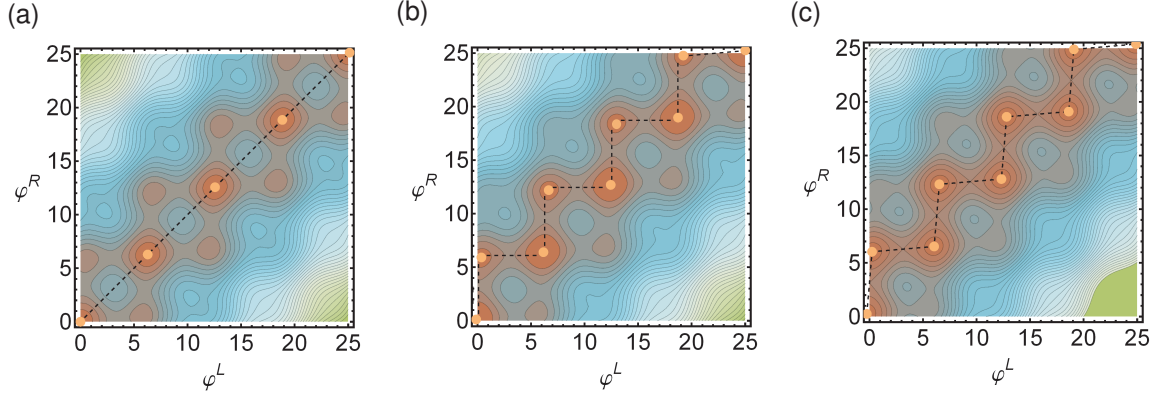


Figure 4.7: **Phase trajectory in 2D SQUID potential.** The two contour plots above show the projection of the tilted washboard potential calculated with  $I_B = 0$  and  $\beta_L = 5$  for different values of flux frustration in the loop (a)  $\varphi_{\text{ext}} = 0 \pmod{2n\pi}$ , (b)  $\varphi_{\text{ext}} = \pi/2 \pmod{2n\pi}$  and (c)  $\varphi_{\text{ext}} = \pi \pmod{2n\pi}$ . The pale orange points denote the positions of numerically evaluated potential minima, across which the phase particle hops charting out the trajectory shown with dashed black lines (adapted from [Clarke and Braginski, 2004]).

and differential modes.

$$\Pi^C(t) = \sum_{k=1}^K f^C(\varepsilon) \cos(k\omega_J t) + g^C(\varepsilon) \sin(k\omega_J t) \quad (4.20a)$$

$$\Pi^D(t) = \sum_{k=1}^K f^D(\varepsilon) \cos(k\omega_J t) + g^D(\varepsilon) \sin(k\omega_J t). \quad (4.20b)$$

We have already seen in chapter 3 that such pump configurations can implement asymmetric frequency conversion protocols<sup>2</sup>. In the following section we will see how they lead to directional gain in the SQUID amplifier.

### 4.2.3 RF response: Scattering Matrix

We now study the rf dynamics using a perturbative series expansion around the working point, established by static bias parameters (the static bias current  $I_B$  and

<sup>2</sup>It is instructive to note that the transfer function of SQUID is also maximum for  $\Phi_{\text{ext}} = \Phi_0/4$  (see Fig. 4.6 and [Clarke and Braginski, 2004]).

external flux  $\Phi_{\text{ext}}$  shown in Fig. 4.2), evaluated in the last section. The aim is to calculate signal amplitudes of the relevant modes, by including the  $\Sigma^{C,D}(t)$  term in our analysis and considering all the mixing processes with the pumps evaluated in the last section, permitted by the harmonic balance of Eqs. (4.4), (4.7) and (4.8). This is equivalent to the representation shown in Fig. 4.4(c), where we model the mixing of the input signal by the SQUID as a parametric interaction with different Josephson harmonics playing the role of an effective “colored” pump. In the limit of a small amplitude input signal, which is the relevant limit for most practical situations, we can then introduce a linear response description of the dynamics as an admittance matrix seen from the ports. This can be obtained from the current-phase and voltage-phase relationship [Eqs. (4.4),(4.7)] as

$$\begin{pmatrix} \boldsymbol{\mathcal{E}}^C \\ \boldsymbol{\mathcal{E}}^D \end{pmatrix} = \underbrace{\begin{pmatrix} \tilde{\mathbb{M}}^{CC} & \tilde{\mathbb{M}}^{CD} \\ \tilde{\mathbb{M}}^{DC} & \tilde{\mathbb{M}}^{DD} \end{pmatrix}}_{\tilde{\mathbb{M}}} \begin{pmatrix} \boldsymbol{\Sigma}^C \\ \boldsymbol{\Sigma}^D \end{pmatrix} \quad (4.21)$$

$$\begin{pmatrix} \hat{\boldsymbol{\mathcal{E}}}^C \\ \hat{\boldsymbol{\mathcal{E}}}^D \end{pmatrix} = \underbrace{\begin{pmatrix} \hat{\mathbb{M}}^{CC} & \hat{\mathbb{M}}^{CD} \\ \hat{\mathbb{M}}^{DC} & \hat{\mathbb{M}}^{DD} \end{pmatrix}}_{\hat{\mathbb{M}}} \begin{pmatrix} \boldsymbol{\Sigma}^C \\ \boldsymbol{\Sigma}^D \end{pmatrix} \quad (4.22)$$

yielding

$$\mathbb{Y} = \hat{\mathbb{M}}\tilde{\mathbb{M}}^{-1}. \quad (4.23)$$

The vectors in the equations above (bold letters) are defined in the basis of all signal and sideband frequencies of interest,  $(\Sigma^C[n\omega_J + \omega_m], \Sigma^D[n\omega_J + \omega_m])$ ,  $n \in [-N, +N]$  leading to a  $4(2N+1) \times 4(2N+1)$  admittance matrix. We further note that the matrix is block diagonal as harmonic balance leads to two disjoint manifolds, each of which forms a closed subspace of dimension  $2(2N + 1)$ .

From the admittance matrix of Eq. (4.23), we can evaluate the scattering matrix of the SQUID using the identity

$$\mathbb{S} = (\mathbb{U} + \mathbb{Y})^{-1}(\mathbb{U} - \mathbb{Y}). \quad (4.24)$$

Figure 4.8 shows the calculation for different orders in junction nonlinearity and the relevant forward ( $|s^{CD}|^2$ ) and backward scattering gain ( $|s^{DC}|^2$ ). The dispersive mixing between various temporal modes of the system at different orders is shown using grey arcs with the relevant Josephson harmonic acting as the pump indicated next to them. The relative strength of the different mixing processes is indicated by the respective widths of the arcs, with the strongest being denoted by the thickest arcs. Also shown are plots of  $\Pi(t)$ , the effective pumps in common (blue) and differential (red) modes at each order of the calculation. The first order calculation shown in Fig. 4.8(a), involving only the Josephson frequency  $\omega_J$ , shows no asymmetry between the forward and backward gains (blue and red surface plots respectively). As the nonlinearity of the device characteristics is increased by reducing  $I_B$  towards  $I_0$  (thus increasing the expansion parameter  $\varepsilon$ ), we extend the order of calculation by including higher order corrections due to higher Josephson harmonics which become significant due to rapid phase running of the junctions in the two-dimensional tilted washboard. This leads to a situation analogous to pumping of the SQUID by an effective multitone pump of the form  $\Pi(t) = \sum_{k=1}^K p_k \cos(\omega_J t + \phi_k)$  in both  $C$  and  $D$  modes (see  $\Pi(t)$  panels in Fig. 4.8), asymmetric about  $t = 0$  [shown in plots of  $\Pi(t)$  in Figs. 4.8(b) and (c)]. The dynamics of such a system include multi-path interference involving different Josephson harmonics. This scheme, analogous to symmetry breaking in ratchet physics [Hanggi and Marchesoni, 2009], implements an asymmetric frequency conversion protocol guided by relative phases  $\phi_k$  of different Josephson harmonics driving the junctions [Kamal et al., 2012]. The signal in the differential

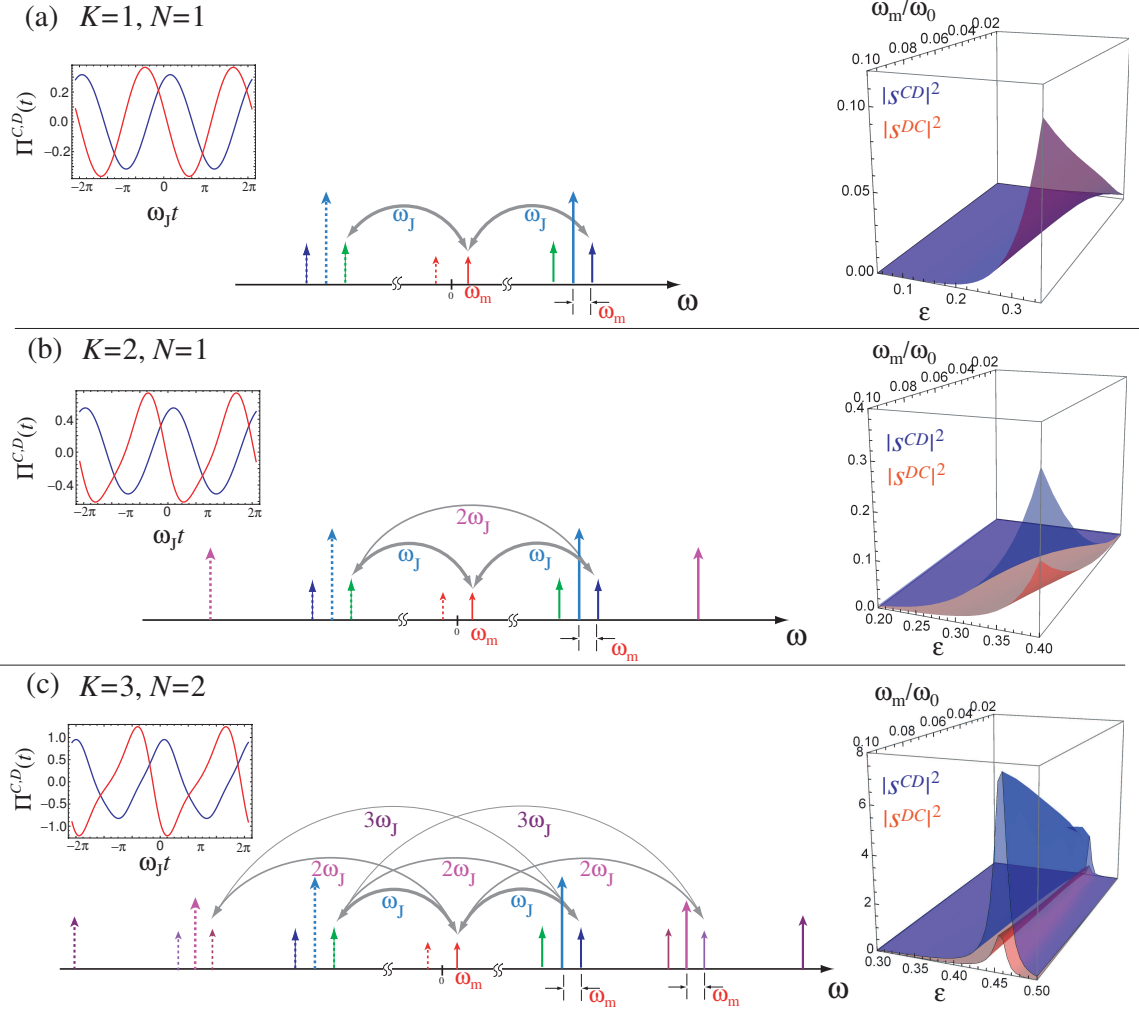


Figure 4.8: **RF scattering response of the SQUID.** Josephson harmonics and small signal scattering gain of the SQUID calculated using harmonic balance with expansion of the  $\sin \varphi$  nonlinearity to (a) first, (b) third and (c) fifth order respectively. Each panel shows the relevant modes of the frequency spectrum included in the calculation at that order [Eqs. (4.12)-(4.13)]. The box panels show the respective forward ( $|s^{CD}|^2$ ) and backward ( $|s^{DC}|^2$ ) scattering gains for a small signal of frequency  $\omega_m$  processed by the SQUID. The asymmetry between forward and backward scattering gains increases on increasing the order of calculation by including higher Josephson harmonics and finally peaks at an optimal value of bias parameter  $\epsilon = 0.455$ .

mode is preferentially upconverted, coupled through higher order mixing processes into the common mode and then preferentially downconverted into the common mode, yielding a net forward gain from the differential mode to the com-

mon mode. The reverse gain process from  $C$  to  $D$  is disfavored by the same reasoning leading to the nonreciprocal operation of the SQUID amplifier, enabling a two-port operation for the MWSA unlike conventional paramps.

### 4.3 Power Gain of the SQUID

The dc SQUID operated as a two-port voltage amplifier resembles the configuration of a semiconductor, operational amplifier as opposed to that of a conventional parametric amplifier which is a matched device. (That is, the input and output impedances are identical to the impedances of the transmission lines or coaxial cables). In this sense the MWSA is the magnetic dual of the rf SET (single electron transistor) [Devoret and Schoelkopf, 2000]. The dc SQUID amplifies an input current (directly coupled as in this analysis or coupled as a flux via an input transformer), and has a much lower impedance than the electromagnetic environment in which it is embedded. Conversely, the rf SET amplifies an input voltage, and has a much higher impedance than the electromagnetic environment in which it is embedded. The true power gain of either device, as seen from the ports, thus involves a de-embedding of the device characteristics. In the case of the SQUID, this requires a translation from the matched (or scattering) description based on the input-output theory considered in this paper to the operational amplifier (op-amp) or hybrid representation that is well suited for describing an unmatched amplifier such as the microwave MWSA.

The hybrid matrix describing a two-port amplifier is of the form [Clerk et al., 2010]

$$\begin{pmatrix} V^{(2)} \\ I^{(1)} \end{pmatrix} = \begin{pmatrix} \lambda_V & Z_{\text{out}} \\ Y_{\text{in}} & \lambda'_I \end{pmatrix} \begin{pmatrix} V^{(1)} \\ I^{(2)} \end{pmatrix}. \quad (4.25)$$

The power gain for such an amplifier is given by

$$\begin{aligned}
 G_P = \frac{P^{\text{out}}}{P^{\text{in}}} &= \frac{(V^{(2)})^2 / \text{Re}[Z_{\text{out}}]}{(V^{(1)})^2 / \text{Re}[Z_{\text{in}}]} \\
 &= \frac{\lambda_V^2}{\text{Re}[Y_{\text{in}}] \text{Re}[Z_{\text{out}}]}, \tag{4.26}
 \end{aligned}$$

where  $\lambda_V$  represents the voltage gain of the amplifier,  $Y_{\text{in}}$  is the input admittance and  $Z_{\text{out}}$  is the output impedance. Equation (4.26) calculates the effective gain of an equivalent “matched” device accounting for the impedance mismatch at the input and output ports.<sup>3</sup>

In principle, the calculation of quantities in Eq. (4.25) can be performed using the scattering matrix evaluated in Eq. (4.24) [Clerk et al., 2010], nonetheless it is advantageous to transform to a description that is more natural in describing the relationship between standing mode current and voltage variables. We find that an impedance matrix ( $\mathbb{Z}$ ) representation is well suited for such a purpose due to its rather straightforward mapping to the standing mode quantities of Eq. (4.25). Using the  $\mathbb{Y}$ -matrix derived in Eq. (4.23), we can write the impedance matrix  $\mathbb{Z}$  of the dc SQUID as

$$\mathbb{Z} = (\mathbb{U} + \mathbb{Y})^{-1} \tag{4.27}$$

with

$$\begin{pmatrix} \check{\omega}^C \\ \check{\omega}^D \end{pmatrix} = \begin{pmatrix} z^{CC} & z^{CD} \\ z^{DC} & z^{DD} \end{pmatrix} \begin{pmatrix} \hat{\omega}^C \\ \hat{\omega}^D \end{pmatrix}. \tag{4.28}$$

---

<sup>3</sup>One way to see this is that, in the zero reverse gain limit, Eq. (4.26) translated in scattering language gives us  $\frac{|S^{21}|^2}{(1-|s^{11}|^2)(1-|s^{22}|^2)}$ . Here  $|S^{21}|^2$  is the usual forward scattering gain from a signal entering port 1 and leaving port 2, while the denominator is normalization to account for actual power that enters and leaves the device after reflections at the input and the output. In Ref. [Spietz et al., 2008], they calculate the power gain of a microwave SQUID amplifier using these arguments.

Here, as before,  $\check{\omega}$ ,  $\hat{\omega}$  are vectors defined in the space of all signal and sideband frequencies of interest. Also  $\mathbb{U}$  is an identity matrix of appropriate dimensions and corresponds to the admittance contribution due to resistive shunts across the junctions.

The next step is to make the translation from the impedance matrix derived in the common and differential mode basis to the two-port description of Eq. (4.25). This requires an identification of the correct “input” and “output” voltages and current for the circuit in Fig. 4.4(a). As the SQUID readout involves measurement of the voltage developed across it, the relevant output quantities are related to the common mode quantities as  $V^{(2)} = V^C$  and  $I^{(2)} = 2I^C$ . The translation to the input variables of the hybrid representation is more subtle. For this purpose, we first note that in the conventional SQUID operation, the input flux coupled into the ring modulates the circulating current  $J$  which is, thus, the relevant input current of the device. The equivalent input voltage that causes the flux modulation of the circulating current can be represented by a voltage source  $V_J$  in series with the inductance of the loop. Figure 4.9 gives a summary of the different possible two-port representations of the SQUID used in this paper.

On interpreting the loop variables  $(V_J, J)$  described above in terms of the differential mode voltage  $V^D$  and current  $I^D$  (see appendix E for details), we obtain the following equivalence between the coefficients of the hybrid matrix in Eq. (4.25) and the  $\mathbb{Z}$ -matrix of Eq. (4.28):

$$\lambda_V = \left( \frac{R}{i\omega_m L} \right) z^{CD}[\omega_m] \quad (4.29)$$

$$\lambda_I = \left( \frac{R}{i\omega_m L} \right) z^{DC}[\omega_m] \quad (4.30)$$

$$Z_{\text{out}} = \left( \frac{R}{2} \right) z^{CC}[\omega_m] \quad (4.31)$$

$$Y_{\text{in}} = (i\omega_m L)^{-1} + \left( \frac{2R}{\omega^2 L^2} \right) z^{DD}[\omega_m]. \quad (4.32)$$

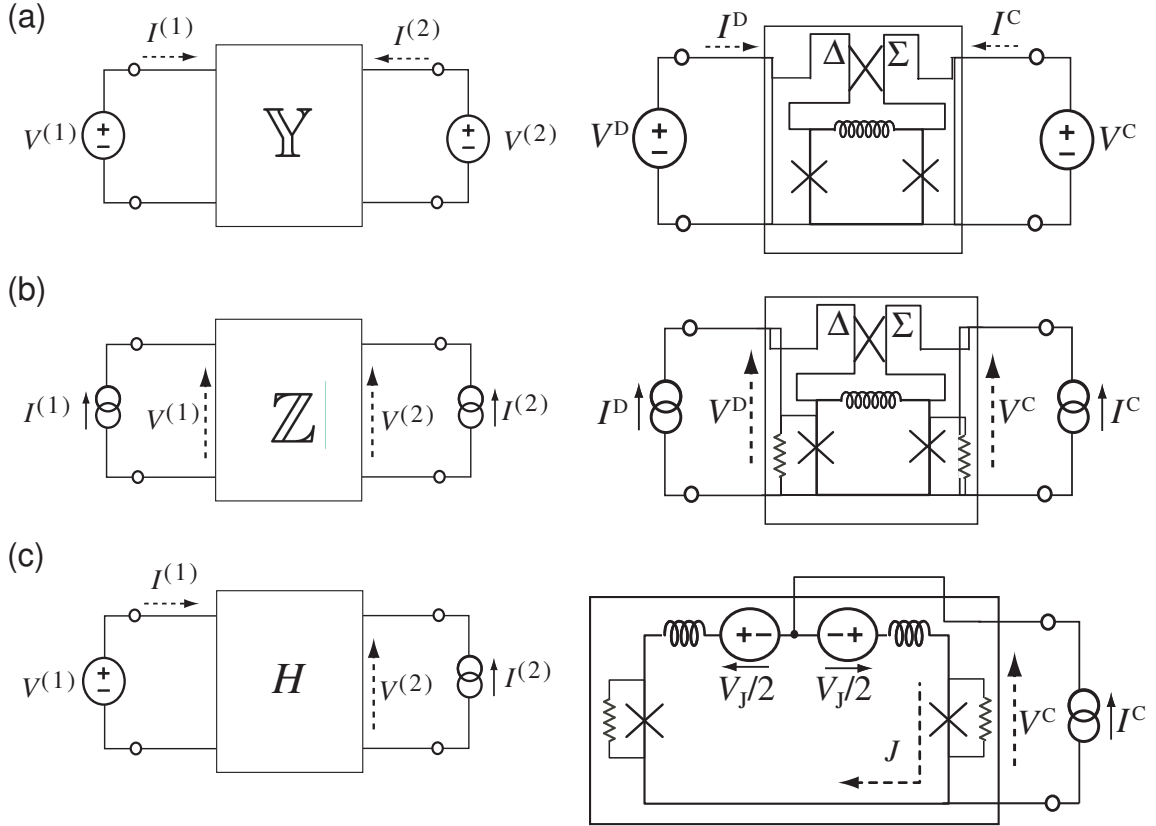


Figure 4.9: **Different representations of a two-port network and analog configurations for the dc SQUID.** (a)  $\mathbb{Y}$ -matrix representation defined for closed boundary conditions  $Y^{ij} = dI^i/dV^j|_{V^{k \neq j}=0}$  for the junctions and inductance, omitting the shunts [Eq. (4.23)]. (b)  $\mathbb{Z}$ -matrix representation defined for open boundary conditions  $Z^{ij} = dV^i/dI^j|_{I^{k \neq j}=0}$  including the shunts [Eq. (4.27)]. (c) (Hybrid)  $\mathbb{H}$ -matrix or Op-amp representation defined with mixed boundary conditions [Eq. (4.25)]. In effective matrices for the SQUID, the common mode (C) and differential mode (D) excitations of the ring play the role of ports 1 and 2, if the SQUID is addressed using hybrids. In each panel, the quantities shown with solid arrows represent the stimulus while those shown with dashed arrows represent the corresponding response of the network.

Using the above translation in Eq. (4.26), we find an expression for the power gain purely in terms of  $\mathbb{Z}$ -matrix coefficients,

$$G_P[\omega_m] = \frac{|z^{CD}[\omega_m]|^2}{\text{Re}[z^{CC}[\omega_m]]\text{Re}[z^{DD}[\omega_m]]}. \quad (4.33)$$

Figure 4.10 shows the power gain of the device as a function of bias and in-

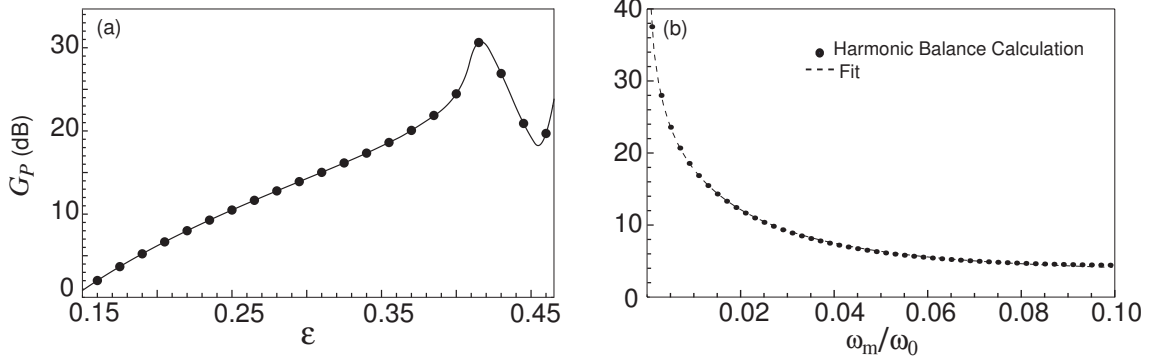


Figure 4.10: **Power gain of the MWSA** calculated with  $K = 3$ ,  $N = 2$ , taking into account the modification of the input and output impedances of the device by matched loads. The parameters are  $\Phi_{\text{ext}} = \Phi_0/4$ ,  $\beta_L = 1$  and  $\Omega_C = 1$ . (a) Power gain versus bias parameter  $\varepsilon = \omega_0/\omega_B$  calculated for a fixed input frequency  $\omega_m = 0.01 \omega_0$ . The solid curve is an interpolating polynomial of degree two. (b) Power gain versus input frequency  $\omega_m/\omega_0$  calculated with bias parameter fixed at  $\varepsilon = 0.455$ , the optimum value for attaining minimum noise temperature [see Fig. 4.12(a)] at low frequencies ( $\omega \ll \omega_0$ ). The fit is of the form  $G_P(\text{linear units}) = [0.006/(\omega_m/\omega_0)^2] + 2$ .

put frequency, calculated using Eq. (4.33). The power gain increases quadratically with decreasing input signal frequency, a result corroborated by a simple quasistatic treatment presented in Appendix F. This result also agrees well with that derived for generic quantum-limited linear detectors in Ref. [Clerk et al., 2010] where it was shown that power gain scales as  $(k_B T_{\text{eff}}/\hbar\omega_m)^2$ . Here,  $T_{\text{eff}}$  is the effective temperature of the detector. The characteristic Josephson frequency,  $\omega_0 = 2eI_0R/\hbar = k_B T_{\text{eff}}/\hbar$ , thus sets the effective temperature of the MWSA and the scale of power gain.

The reverse power gain of the device be calculated in a similar manner as [cf. Eq. (4.25)]

$$\begin{aligned}
 G_P^{\text{rev}} &= \frac{(I^{(1)})^2 \text{Re}[Z_{\text{in}}]}{(I^{(2)})^2 \text{Re}[Z_{\text{out}}]} = \frac{\lambda_I^2}{\text{Re}[Y_{\text{in}}] \text{Re}[Z_{\text{out}}]} \\
 &= \frac{|z^{DC}[\omega_m]|^2}{\text{Re}[z^{CC}[\omega_m] \text{Re}[z^{DD}[\omega_m]]]}. \tag{4.34}
 \end{aligned}$$

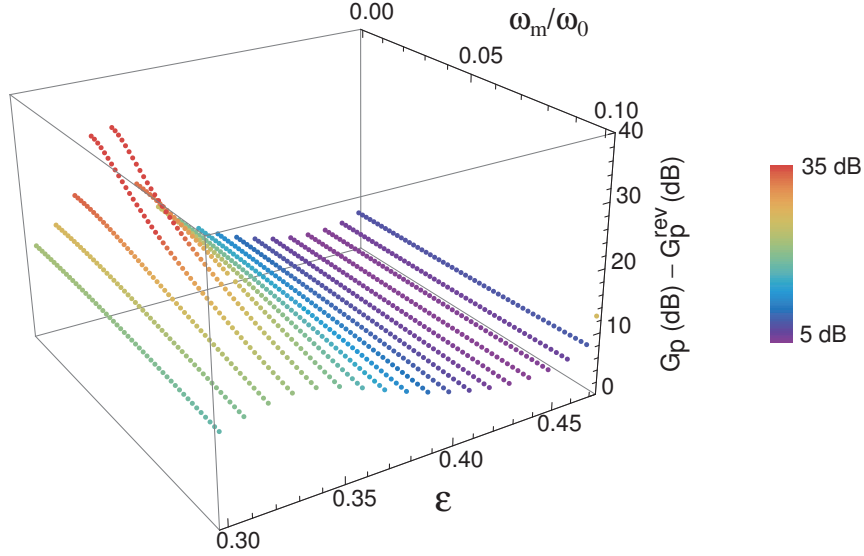


Figure 4.11: **Directionality of the MWSA.** Directionality (in dB) a function of bias parameter  $\varepsilon$  and reduced input frequency  $\omega_m/\omega_0$ . The red dots represent high directionality and blue dots represent low directionality. The parameters used were the same as those in Fig. 4.10.

The asymmetry between forward and reverse gain, which follows directly from the asymmetric scattering gain discussed in the previous section, is a strong function of the bias  $\varepsilon$  (cf. Fig. 4.11); furthermore we see that the optimal bias for maximum power gain is not the same as that for maximal directionality. We note that the results presented here have been obtained with a truncated harmonic series excluding all Josephson harmonics above  $3\omega_J$ . In a real device, the achievable isolation between forward (differential-to-common) and backward (common-to-differential) gain channels maybe quantitatively different due to the presence of the neglected higher order interferences.

## 4.4 Noise Temperature

In this section, we evaluate the noise added by the dc SQUID operated as a voltage amplifier. The noise added by a system can be quantified by its noise temperature,

$T_N$ , defined as

$$T_N = A_N \frac{\hbar\omega}{k_B} \quad (4.35)$$

where  $A_N$  represents the Caves added noise number [Caves, 1982]. This noise temperature corresponds to the effective input temperature of the amplifier obtained by referring the added noise measured at the output to the input, and is quantified in terms of energy quanta per photon at signal frequency. For a phase preserving amplifier, such as the MWSA, the minimum possible noise temperature corresponds to half a photon of added noise, that is,  $A = 0.5$ .

Using the hybrid representation developed in the previous section and Appendix E, we write the noise inequality for the MWSA as,

$$k_B T_N \geq \frac{\sqrt{\bar{S}_{VcVc}\bar{S}_{JJ} - \text{Re}[\bar{S}_{VcJ}]^2} - \text{Im}[\bar{S}_{VcJ}]}{\lambda_V}, \quad (4.36)$$

where  $\bar{S}_{VV}$  represents the spectral density of the voltage fluctuations at the output,  $\bar{S}_{JJ}$  represents the spectral density of the circulating current fluctuations and  $\bar{S}_{VJ}$  is the cross-correlation between the voltage and current fluctuations.

As in the case of power gain, we can evaluate the spectral densities in Eq. (4.36) from the  $\mathbb{Z}$  matrix of the SQUID derived in Sec. 4.3. This exercise is enabled by the fact that the input-output theory treats the deterministic signal input and noise of the system on equal footing. We note that this is equivalent to the assumption that the response of the system to input noises is linear, i.e., the fluctuations of  $I$  and  $V$  are linear in the fluctuations of the input noise operators. This is not a priori obvious for a nonlinear system such as the SQUID. Linear response can always be justified when calculating response coefficients such as the power gain, as one could in principle always make the input signal (or the perturbation) arbitrarily small. In contrast one cannot, in general, make the magnitude of the input noise

operators arbitrarily small. However, we can justify such a small-signal linearized approach for noise analysis of the SQUID as the typical photon energy at the frequencies of interest, the Josephson frequency and its first few harmonics, is much smaller than the energy dissipated per turn of the SQUID running phase because of the low  $Q$  of the Josephson oscillations. We can illustrate this, heuristically, by estimating the magnitude of the voltage fluctuations about the working point in the running regime of the junctions. For this purpose, we evaluate the zero-point fluctuations of the common mode voltage as

$$\begin{aligned}\langle \Delta V_{ZPF}^C \rangle &= \omega_J \langle \Phi_{ZPF}^C \rangle \\ &= \omega_J \sqrt{\frac{\hbar Z_0}{2}}\end{aligned}\quad (4.37)$$

where  $Z_0$  represents the device impedance. Using the above relation, in conjunction with Eq. (4.14) to fix the value of  $\langle V^C \rangle$ , we obtain

$$\left\langle \frac{\Delta V_{ZPF}^C}{V^C} \right\rangle = \sqrt{\frac{Z_0}{2R_q}} \ll 1. \quad (4.38)$$

Thus, due to SQUID being a low impedance device, with impedance  $Z_0$  much less than the reduced superconducting resistance quantum  $R_q \simeq 1 \text{ k}\Omega$ , the mean voltage fluctuations are much smaller than the average voltage across the device making the linear response a valid approximation even when one takes quantum fluctuations into account. In light of the above argument we can calculate the SQUID response to noise, both in the thermal and quantum regimes, simply by replacing the input current signal with a noise signal described by a spectral density of the form

$$\bar{S}_{II}[\omega] = 2\hbar\omega \text{Re}[Y[\omega]] \coth\left(\frac{\hbar\omega}{2k_B T}\right). \quad (4.39)$$

Treating the noise and deterministic signal on the same footing, we can then use the  $\mathbb{Z}$  matrix to write the voltage noise spectral density in the common mode as

$$\bar{S}_{V_C V_C} = \sum_{n=-N}^N |z_{0n}^{CC}|^2 \bar{S}_{I_C I_C}[n\omega_J + \omega_m] + \sum_{n=-N}^N |z_{0n}^{CD}|^2 \bar{S}_{I_D I_D}[n\omega_J + \omega_m]. \quad (4.40)$$

Here, the first sum accounts for the contribution to the noise arising from the common mode signal ( $n = 0$ ) and sidebands about the Josephson harmonics ( $n = \pm 1, \pm 2$ ) included in the calculation; the second sum accounts for the noise generated in the common mode output signal by the differential mode signal and sidebands, arising from coupling between  $C$  and  $D$  modes. Similarly, we can calculate  $\bar{S}_{J J}$  as

$$\bar{S}_{J J} = \frac{4}{\omega_m^2 L^2} \bar{S}_{V_D V_D}, \quad (4.41)$$

by making the identification  $J = 2V^D/(i\omega L)$ . Here, as before, we calculate  $S_{V_D V_D}$  from the  $Z$  matrix:

$$\bar{S}_{V_D V_D} = \sum_{n=-N}^N |z_{0n}^{DC}|^2 \bar{S}_{I_C I_C}[n\omega_J + \omega_m] + \sum_{n=-N}^N |z_{0n}^{DD}|^2 \bar{S}_{I_D I_D}[n\omega_J + \omega_m]. \quad (4.42)$$

Finally, for  $S_{V J}$  we have

$$\bar{S}_{V_C J} = \frac{-2}{i\omega_m L} \left( \sum_{n=-N}^N z_{0n}^{CC} z_{0n}^{DC*} \bar{S}_{I_C I_C}[n\omega_J + \omega_m] + \sum_{n=-N}^N z_{0n}^{CD} z_{0n}^{DD*} \bar{S}_{I_D I_D}[n\omega_J + \omega_m] \right). \quad (4.43)$$

Figure 4.12 shows plots of the Caves noise number  $A_N$  of the device, calculated in

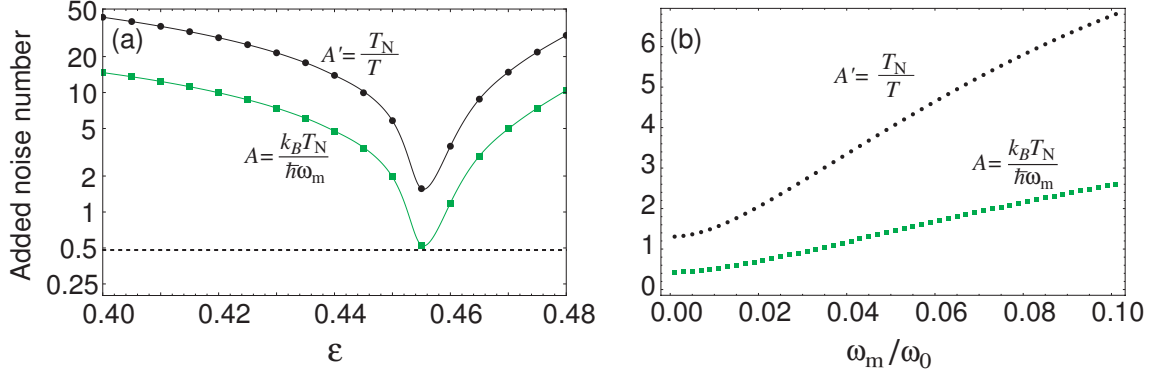


Figure 4.12: **Caves added noise number for the MWSA.** calculated using the harmonic balance analysis with  $K = 3$ ,  $N = 2$  as a function of (a)  $\varepsilon = \omega_0/\omega_B$  for  $\omega_m = 0.01 \omega_0$  and (b) reduced input frequency  $\omega_m/\omega_0$  with  $\varepsilon = 0.455$ . In both plots, (round) black markers show the noise number  $A'_N = T_N/T$  obtained in the thermal regime  $k_B T \gg \hbar \omega_m$ , while (square) green markers show the noise number  $A_N = k_B T_N / \hbar \omega_m$  calculated in the quantum regime  $k_B T \ll \hbar \omega_m$ . The solid curves represent interpolating polynomials. The quantum calculation gives a minimum value for  $A_N = k_B T_N / \hbar \omega_m \approx 0.5$ , attained at  $\varepsilon = 0.455$ , corresponding to one-half photon of added noise (shown using dashed line). The optimal value of bias current for minimum added noise does not coincide with that for achieving the maximum power gain [Fig. 4.10(a)] or directionality (Fig. 4.11).

both the thermal regime [ $k_B T \gg \hbar \omega_m$  and hence all the terms in Eqs. (4.40)-(4.43) contribute equal amount of noise power] and quantum regimes [ $k_B T \ll \hbar \omega_m$  and hence each term in Eqs. (4.40)-(4.43) contributes an amount proportional to its frequency in accordance with Eq. (4.39)].

The optimum bias point for minimum noise corresponds to the bias for maximum scattering gain [Fig. 4.8(c)] rather than for the maximum power gain [Fig. 4.10(a)]. This result follows from the fact that the added noise is a property of the bare SQUID without any matching to input and output loads. In the case of conventional parametric amplifiers, the minimum noise indeed occurs at the maximum scattering gain. Furthermore, the partial cross-correlation between the output voltage noise across the SQUID and the supercurrent noise circulating in the loop is crucial to minimizing the noise in both thermal and quantum regimes. We also note that for low enough signal frequencies, the calculated added noise number is

found to saturate at a value slightly below the quantum limit of one half-photon at the signal frequency. This result, we suspect, is due to the fact that at the bias for minimum noise, the reverse gain is substantial and hence the isolation is not perfect (Fig. 4.11). The quantum limit of one half-photon is a limiting value calculated for ideal detectors with zero reverse gain and high forward gain [Clerk et al., 2010], a condition which is not satisfied at the optimal noise bias in our calculation. Finally, our calculation shows that the minimum noise number is achieved only when the signal frequency is much lower than the characteristic Josephson frequency  $\omega_0 = 2\pi I_0 R / \Phi_0$ , and increases significantly with increasing signal frequency.

## 4.5 Discussion

SQUID as a measurement amplifier for superconducting qubit readout offers the benefit of nonreciprocal amplification over conventional reflection-based paramps. This property besides being most desirable has also been the least understood characteristic of MWSAs. By a rather straightforward generalization of input-output theory, we perform a first-principles analysis of the microwave SQUID amplifier (MWSA). In this paradigm we treat the SQUID biased in its running state as a parametric amplifier pumped by a combination of Josephson harmonics generated internally by the motion of the phase of the junctions, which allows a fully self-consistent description of both the static and rf dynamics of the device. The scattering matrix calculation helped us to derive the nonreciprocal gain characteristics from first principles and showed the crucial role played by the higher Josephson harmonics in nonreciprocal operation of MWSA. It can be thought as a consequence of two-stage parametric frequency conversion, with preferential upconversion in the differential (input) mode followed by a preferential downconversion in the common (output) mode.

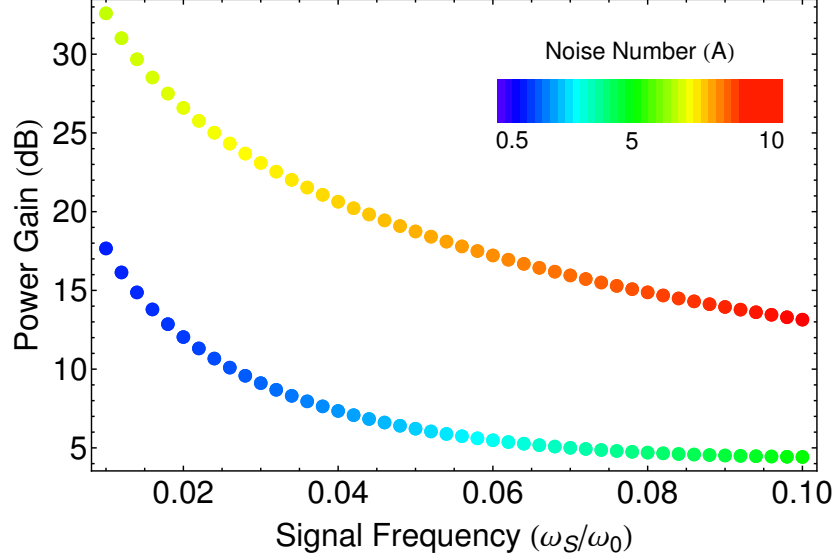


Figure 4.13: **SNR deterioration in MWSA with signal frequency.** Calculated power gain of a microwave SQUID amplifier as a function of signal frequency (normalized by a characteristic Josephson frequency  $\omega_0 = 2\pi I_0 R / \Phi_0$ ) for two bias currents. The color of the respective dots represents the calculated noise temperature. Signal to noise ratio deteriorates with increase in signal frequency for a fixed bias with the minimum noise temperature corresponding to noise number of 0.5 (half-a-photon of added noise) achieved only at low frequencies for an optimal bias ( $\varepsilon = 0.455$  according to Fig. 4.12). Also, as we demand higher power gain by changing the bias, the noise number deteriorates for a given frequency.

One of the most important insights offered by this analysis is the deterioration of signal-to-noise ratio of the MWSA with increase in signal frequency  $\omega_m$ , best depicted by a plot shown in Fig. 4.13. We find that the power gain of the matched SQUID amplifier decreases quadratically with reduced signal frequency  $\omega_m/\omega_0$ . Further, though the MWSA achieves quantum-limited noise performance for optimal flux and current biases and for signal frequencies significantly lower than the characteristic Josephson frequency  $\omega_0 = 2\pi I_0 R / \Phi_0$ , the added noise increases significantly with increasing frequency. In addition, the simultaneous optimization of gain, directionality and noise is a delicate operation since the optimal biases for these three properties do not coincide; for instance optimal bias for minimum noise does not necessarily translate into maximum power gain.

The SNR deterioration with frequency can be alleviated by using junctions with higher values of critical currents. With the present technology for niobium junctions, critical current densities of tens of microamperes per square micron are readily achievable. This translates into characteristic frequencies of about 100 GHz, which should be sufficient to achieve lower noise at GHz frequencies provided hot electron effects due to dissipation in the shunts are mitigated [Wellstood et al., 1994]. Based on our calculation, at the working point for minimum added noise,  $A \approx 0.5$ , power gains of 15 – 18 dB and directionality of around 5 – 8 dB are obtained. However, higher power gains of 20 – 30 dB and directionality of 10 – 12 dB can be realized by permitting a higher noise number  $A \approx 5 – 10$ . Though the predicted directionality is still modest, it suffices to reduce the number of nonreciprocal elements (circulators, isolators) in the measurement chain typically employed for the readout of superconducting qubits. Moreover, the noise penalty incurred with MWSAs compares very well to standard cryogenic amplifiers such as HEMTs whose typical noise numbers lie in the range 40 – 50 for microwave frequencies. As far as bandwidth considerations are concerned, though the direct coupled design analyzed here shows a steeper decrease in gain with frequency as compared to the usual SQUID operation with a matched input coil (where gain scales as  $1/\omega_m$  [Clarke et al., 2011]), a recently reported dc SQUID amplifier [Hover et al., 2012] using the direct coupling method demonstrated a bandwidth of several hundred MHz for an operating frequency of a few GHz.

The results presented here are semi-quantitative, as we have performed a truncation of the harmonic series at fifth order in junction nonlinearity. Nonetheless we believe that extension of the analysis to higher orders, in conjunction with numerical optimization techniques, can be a useful tool to analyze SQUID-based devices due to rapid convergence offered by the harmonic series method. This approach would allow one to evaluate the appropriate parameters, depending on

the intended application, that yield the best compromise between gain and noise properties.

---

# Conclusions

---

*“In physics, you don’t have to go around making trouble for yourself.*

*Nature does it for you.”*

– Frank Wilczek

*“I am not always good and noble.*

*I am the hero of this story, but I have my off moments.”*

– P. G. Wodehouse in *Love Among the Chickens*

In this concluding chapter, we reflect on some open questions and future directions that may emerge from this research.

### **5.1 Tunable nonreciprocity with photons**

This thesis work explored the phenomenon of nonreciprocal dynamics of electromagnetic fields using active Josephson parametric devices as the preferred framework for implementation. The crux of the ideas presented here rested on the fact that in parametric frequency conversion, the phase of the carrier (or local oscillator) sets the phase of the modulated signal. Further the phases associated with up- and downconversion between two frequency channels are equal and opposite

(phase nonreciprocity). This phase-sensitivity of parametric frequency conversion was employed to show that we can achieve nonreciprocity in amplitude in both spatial channels (preferred direction for transmission) and/or temporal channels (preferred direction for frequency conversion) by arranging successive parametric stages performing frequency mixing. Further, we showed, through the example of microwave SQUID amplifier, that by combining such ideas it is possible to achieve nonreciprocity with gain at a given signal frequency (or directional amplification). It is worthwhile to note that in both the gain-less and with-gain proposals, circulation/transmission direction can be reversed by varying the relative phase difference between the drive tones pumping the parametric stages. This may be exploited as an unprecedented in-situ knob for controlling/steering light at single-photon level.

In chapter 2, we proposed a scheme based on two-stage parametric up/down conversions which breaks reciprocal symmetry of transmission and realizes a circulator. Preliminary experiments with lossy mixers seem to confirm the viability of this design and it is exciting to see that experiments with JJ-based quantum-limited mixers have already been initiated (see Fig. 5.1). As quantum information experiments move towards more complicated multi-qubit setups, the ‘real estate’ inside cryostats can get prohibitively expensive. In such a scenario, non-magnetic on-chip versions of crucial, but unfortunately bulky, components like circulators would evolve from being an interesting intrigue to a practical necessity.

In chapters 3 and 4 we extended the interferences based on phase sensitive parametric rotations by including higher order mixing processes. Such schemes promise to exhibit gain accompanying nonreciprocity, with (RSJ) and without frequency conversion (SQUID). This leads to several theoretical and experimental opportunities. For instance, it will be interesting to investigate the minimality/sufficiency of such schemes of directional amplification, guided by the phases

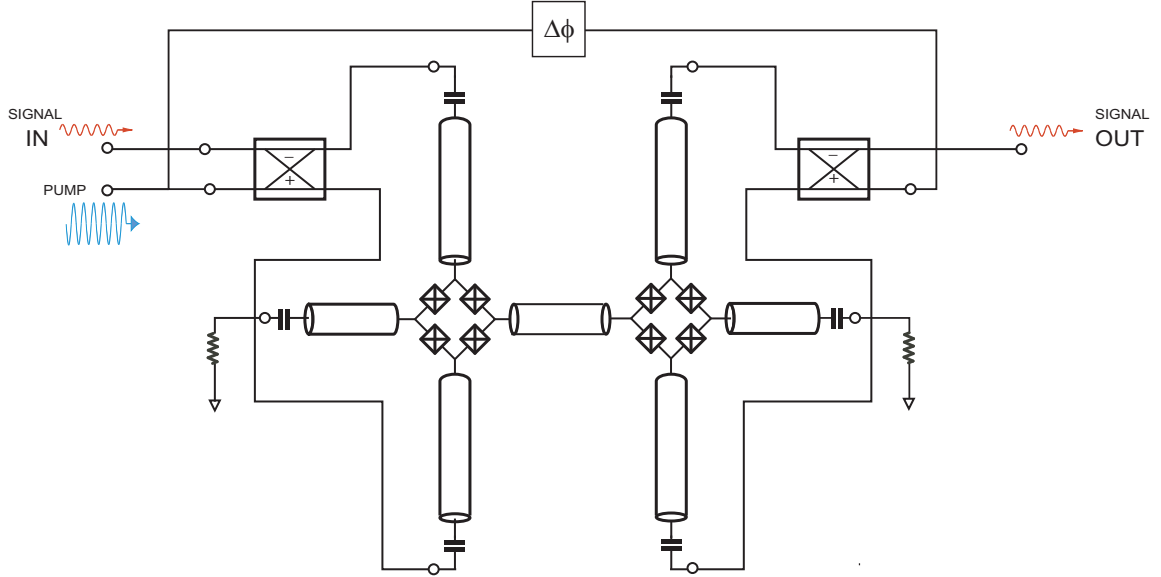


Figure 5.1: **Double JRM based active circulator design.** Circuit schematic of a JRM based design that implements the two-stage active circulator idea presented in chapter 2. The input signal (red) coupled to  $Y$  mode of the left JRM is first upconverted by means of a pump (blue) coupled to its  $Z$  mode. The generated sidebands are collected in the spatially distinct  $X$  mode which is shared with a second JRM. The second JRM on the right downconverts the sidebands to the original input signal frequency, using a pump phase shifted ( $\Delta\phi$ ) with respect to the first pump. The output signal is collected in the  $Y$  mode of the second JRM. For appropriate value of phase shift  $\Delta\phi$  the signal should be transmitted only from left to right and transmission in reverse should be suppressed.

of multi-tone pumps on multiple stages. Such an exercise will be crucial for the realization of an on-chip directional Josephson amplifier with minimal noise.

## 5.2 Novel dynamical cooling protocols

Another area to harness controlled non-reciprocity lies in the frequency domain with applications such as dynamical/sideband cooling of quantum systems. Usual schemes of dynamical cooling employ symmetric frequency conversion between two coupled oscillators with the high frequency oscillator (which is in the ground state at ambient temperature) acting as a reservoir for dumping excitations. This protocol mainly relies on a large difference between photon lifetimes of the os-

cillators to achieve ground state cooling of the low frequency oscillator. If, on the other hand, we can implement an asymmetric frequency conversion scheme by tuning the relative phase between successive harmonics in a colored drive, it should be possible to preferentially shuttle photons from a low frequency oscillator to a high frequency one (or vice versa!). This can lead to more efficient cooling schemes indifferent to relative frequency and lifetime differences between the two coupled systems. Besides superconducting qubits, such a protocol can find tremendous applications in a host of architectures which share the underlying physics of nonlinear interactions with JJ circuits, for example, optomechanical systems [Teufel et al., 2011], trapped ions [Leibbrandt et al., 2009], or nuclear spins in single/double quantum dots [Maletinsky et al., 2007]. Further, there will be several interesting theoretical questions to answer such as what is the ultimate efficiency of such cooling mechanisms, how is the backaction physics [Clerk et al., 2010] modified and what are the fundamental limits on quantum measurements in the presence of such modified coupling. A long term future direction can include the implementation of high fidelity state transfer between coupled quantum systems for quantum communication, based on such nonreciprocal protocols.

### 5.3 Artificial magnetic fields

The idea of replacing magnetic fields by light fields with phase gradients, as exploited in this thesis work for nonreciprocity, can find very interesting applications in conjunction with lattices of cold neutral atoms (real or artificial) as quantum simulators of strongly correlated matter. The electrons on a lattice in the presence of strong magnetic fields are a hotbed for rich physical phenomenon like quantum hall (QH) physics that allow a dissipationless transport mechanism even in the presence of strong disorder. For a particle of charge  $q$  on a 2D lattice, “high” implies fields that translates into a flux  $\hbar\pi/q$  through a unit cell area (or equiv-

alently and Aharonov-Bohm phase shift of  $\pi$  per unit cell) . For real electrons on atomic dimensions, this translates into fields of the order  $10^3$  tesla. The need for such high magnetic fields severely limits the application potential of usual QH systems based on electrons. On the other hand, implementing such a phase shift using light waves is entirely feasible by tuning the relative phase of the light beams driving different sites to induce nontrivial phases in photon hopping terms across different sites. Simulators employing networks of quantum wires, based on JJ arrays [Masluk et al., 2012] and coupled to a light field with a phase gradient along the wire, can be used to realize novel states such as topologically protected chiral photonic states [Wang et al., 2008] (analogous to edge states in QH effect) or even fractional QH states [Kane et al., 2002].

---

## Faraday Rotation vs Optical Activity

---

Both Faraday rotation and optical activity are seemingly similar phenomena involving rotations of polarization of light wave propagating through a medium. Nonetheless, while optically active materials implement reciprocal rotations which cancel themselves on a reverse pass through the medium, Faraday rotation is non-reciprocal and leads to a doubling of angle of rotation after a reverse pass through the medium, as shown in Fig. 1.3. To understand this difference in greater detail, let us briefly consider the propagation of electromagnetic waves in birefringent media.

The two different circular polarizations of an electric field vector  $\mathbf{E}$  can be expressed as  $\mathbf{e}_+ = \hat{x} - i\hat{y}$  and  $\mathbf{e}_- = \hat{x} + i\hat{y}$  denoting the right-circularly polarized or RCP (clockwise rotation of  $\mathbf{E}$  in the plane of polarization) and left-circularly polarized or LCP (anticlockwise rotation of  $\mathbf{E}$  in the plane of polarization) components respectively. Here we have assumed  $\hat{z}$  to be the direction of propagation of the wave. Using these circular basis vectors we can write  $\mathbf{E}$  as,

$$\mathbf{E} = \hat{x}E_x + \hat{y}E_y \tag{A.1}$$

$$= \hat{e}_+E_+ + \hat{e}_-E_- \tag{A.2}$$

with  $E_{\pm} = 1/2(E_x \pm iE_y)$ . In the following sections, we will derive expressions for  $E_{\pm}$  components of the field propagating through an optically active and Faraday medium respectively, elucidating the difference between the two phenomenon.

## A.1 Optical Activity

Usual optically active media include chiral materials like sugar solution, or the more famous double-helical DNA molecule. The common characteristic of such substances is the lack of structural inversion symmetry. A useful way of expressing the constitutive relationships between the displacement field  $\mathbf{D}$  and electric field  $\mathbf{E}$  is to model them as bi-isotropic materials which have a coupling between electric and magnetic fields as,

$$\mathbf{D} = \epsilon\mathbf{E} - i\chi\mathbf{H}, \quad (\text{A.3})$$

$$\mathbf{B} = \mu\mathbf{H} + i\chi\mathbf{E} \quad (\text{A.4})$$

where  $\chi$  describes the chiral properties of the medium. We note that bi-isotropy is not a necessary condition for a material to possess optical activity but such a model for chiral media, at a single frequency, can be used to describe the properties of general optically active media. For a lossless birefringent media use of Eq. (A.4) in third and fourth Maxwell's equations,

$$\hat{z} \times \partial_z \mathbf{E} = -i\omega\mathbf{B}$$

$$\hat{z} \times \partial_z \mathbf{H} = i\omega\mathbf{D}$$

leads to a set of equations that can be diagonalized by defining following linear combinations of circular  $E_+$  and  $H_+$  components

$$E_{\pm}^R = E_{\pm} - i\sqrt{\frac{\mu}{\epsilon}}H_{\pm} \quad (\text{A.5})$$

$$E_{\pm}^L = E_{\pm} + i\sqrt{\frac{\mu}{\epsilon}}H_{\pm}.^1 \quad (\text{A.6})$$

In this basis, propagation equations assume the form

$$\frac{\partial}{\partial z} \begin{pmatrix} E_{\pm}^R \\ E_{\pm}^L \end{pmatrix} = \begin{pmatrix} \mp ik_+ & 0 \\ 0 & \pm ik_- \end{pmatrix} \begin{pmatrix} E_{\pm}^R \\ E_{\pm}^L \end{pmatrix}$$

which give us the following relations for circular-basis fields

$$E_+(z) = E_+^R(z) + E_+^L(z) = A_+e^{-ik_+z} + B_+e^{ik_-z} \quad (\text{A.7a})$$

$$E_-(z) = E_-^L(z) + E_-^R(z) = A_-e^{-ik_-z} + B_-e^{ik_+z} \quad (\text{A.7b})$$

where  $k_{\pm} = \omega(\sqrt{\mu\epsilon} \pm \chi)$  are the wave-vectors. Here

$$E_{\pm}^R = \frac{1}{2} \left( E_{\pm} - i\sqrt{\frac{\mu}{\epsilon}}H_{\pm} \right) \quad (\text{A.8a})$$

$$E_{\pm}^L = \frac{1}{2} \left( E_{\pm} + i\sqrt{\frac{\mu}{\epsilon}}H_{\pm} \right). \quad (\text{A.8b})$$

with subscripts  $\pm$  denoting the forward or backward propagation and superscripts  $R$ ,  $L$  denote right- or left-polarization. Thus, as seen from Eq. (A.7)  $E_+(z)$  circular component propagates forward with  $k_+$  and backward with  $k_-$ . Furthermore, the forward moving component of  $E_+$  and the backward moving component of  $E_-$  i.e.  $E_+^R$  and  $E_-^R$  are both right polarized and propagate with same wave number  $k_+$ . Similarly, left-polarized waves  $E_+^L$  and  $E_-^L$  propagate with wave vec-

---

<sup>1</sup>See Ref. [Orfanidis, 2008] for additional calculational details.

tor  $k_-$ . Thus, a wave of given circular polarization (left or right) propagates with the same wavenumber regardless of its direction of propagation. This is a characteristic difference of chiral versus gyrotropic media in external magnetic fields (see below).

Thus, propagating a linearly polarized light  $\mathbf{E} = \hat{e}_+ A_+ + \hat{e}_- A_-$  at  $z = 0$  by a distance  $l$  according to Eq. (A.8), we obtain

$$\begin{aligned} \mathbf{E}(l) &= \hat{e}_+ A_+ e^{-ik_+ l} + \hat{e}_- A_- e^{-ik_- l} \\ &= [\hat{e}_+ A_+ e^{-i\phi} + \hat{e}_- A_- e^{i\phi}] e^{-i(k_+ + k_-)l/2} \end{aligned} \quad (\text{A.9})$$

where

$$\phi = \frac{1}{2}(k_+ - k_-)l. \quad (\text{A.10})$$

Eq. (A.9) represents a linearly-polarized wave with plane of polarization rotated by  $\phi$ . It is straightforward to see from Eq. (A.8) that on reversing the direction of propagation the role of  $k_+$  and  $k_-$  are interchanged and hence  $\phi \rightarrow -\phi$ . This leads to zero rotation for a roundtrip (outbound+reflection+inbound) pass of the wave.

## A.2 Faraday Rotation

Gyrotropic media such as ferrites, in the presence of a constant external magnetic field, have the constitutive relationships such as that shown in Eq. (1.14). In conjunction with the  $\mathbf{D} = \epsilon\mathbf{E}$ , it leads to relationships of the form

$$E_+(z) = E_+^R(z) + E_+^L(z) = A_+ e^{-ik_+ z} + B_+ e^{ik_+ z} \quad (\text{A.11a})$$

$$E_-(z) = E_-^L(z) + E_-^R(z) = A_- e^{-ik_- z} + B_- e^{ik_- z}, \quad (\text{A.11b})$$

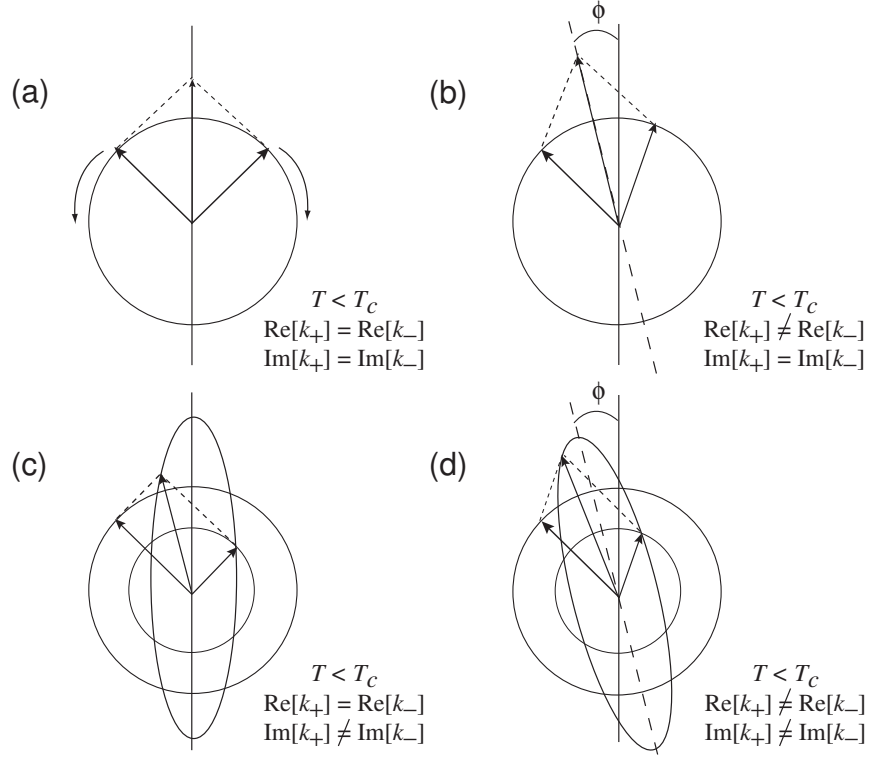


Figure A.1: **Faraday effect.** (a) Ferrite above its curie temperature does not affect the RCP (+) and LCP (-) circularly polarized components. (b) Faraday rotation when ferrite below Curie temperature induces an asymmetry between propagation velocities. (c) Faraday ellipticity when ferrite attenuates the RCP and LCP components by different magnitudes. (d) Faraday effect – a combination of (b) and (c) (adapted from [Shinagawa, 2000]).

where, as in the case of optically active media discussed in the previous section, we have diagonalized the electric field  $\mathbf{E}$  in circular basis by defining

$$E_{\pm}^R = \frac{1}{2} \left( E_{\pm} - i \sqrt{\frac{\mu_{\pm}}{\epsilon}} H_{\pm} \right), \quad (\text{A.12a})$$

$$E_{\pm}^L = \frac{1}{2} \left( E_{\pm} + i \sqrt{\frac{\mu_{\pm}}{\epsilon}} H_{\pm} \right). \quad (\text{A.12b})$$

Here, in addition, we have defined a left/right circular permeability ( $\mu_{\pm} = \mu_1 \pm \mu_2$ ) and accordingly  $k_{\pm} = \omega \sqrt{\mu_{\pm} \epsilon}$ .

According to Eq. (A.11) the  $E_{\pm}^L(z)$  circular component propagates in forward

and backward with different wavenumbers  $k_+$  and  $k_-$  respectively (same for  $E_{\pm}^R(z)$ ). In contrast, in case of optical activity, Eq. A.9 showed us that  $E^{L,R}(z)$  components propagated with same wavenumbers irrespective of propagation direction. Thus, in a Faraday medium, a wave of given circular polarization (left or right) propagates with different wavenumbers depending on its direction of propagation. Doing the same analysis, as in the case of optical activity, using Eq. (A.11) we find that the roles of  $k_+$  and  $k_-$  remain unchanged on reversing the propagation and hence the rotation angle doubles after a roundtrip through a Faraday medium, i.e.  $2\phi = (k_+ - k_-)l$ .

If the RCP or LCP waves experience different attenuation coefficients (i.e.  $\text{Im}[k_+] \neq \text{Im}[k_-]$ ), it gives rise to *Faraday ellipticity* where the transmitted light is elliptically polarized with the major axis of the ellipse pointing defined by the rotated polarization vector <sup>2</sup>.

---

<sup>2</sup>Similar to Faraday rotation which is a nonreciprocal rotation on transmission through a ferrite, there exists a nonreciprocal effect exhibited in reflection from ferromagnetic materials known as *polar Kerr effect*. Besides ferrites, it has been reportedly seen in high-temperature superconductors [Kapitulnik et al., 2009] and has recently been predicted for bilayer graphene [Nandkishore and Levitov, 2011].

---

## Input-output theory

---

Input-output theory (IOT) is a paradigm in scattering formalism (S-matrix theory) which applies to a system coupled to a heat bath. It is well documented in the literature [Yurke, 2004] but we include a brief description here for the help of the readers and consistency of notation. For the analysis via IOT, the resistance ( $R$ ) of a circuit is replaced with a transmission line of characteristic impedance  $Z_c (= R)$  and the voltage and the current along the line are expressed in terms of superposition of incoming and outgoing waves (Fig. B.1). The waves represent either a signal launched on the line to drive the oscillator (pumps, signal) or the thermal/quantum fluctuations in the line (e.g. Nyquist noise of the resistor). The power of this semiclassical technique, apart from its calculational advantage, lies in the provision of simple physical insights into the link between the noise sources and dissipation. The voltages ( $V$ ) and currents ( $I$ ) are expressed in terms of incoming and outgoing field amplitudes ( $A$ ) are expressed as:

$$\begin{aligned} V(z, t) &= \sqrt{Z_c} (A^{\text{out}}(z, t) + A^{\text{in}}(z, t)) \\ I(z, t) &= \frac{1}{\sqrt{Z_c}} (A^{\text{out}}(z, t) - A^{\text{in}}(z, t)) \end{aligned} \quad (\text{B.1})$$

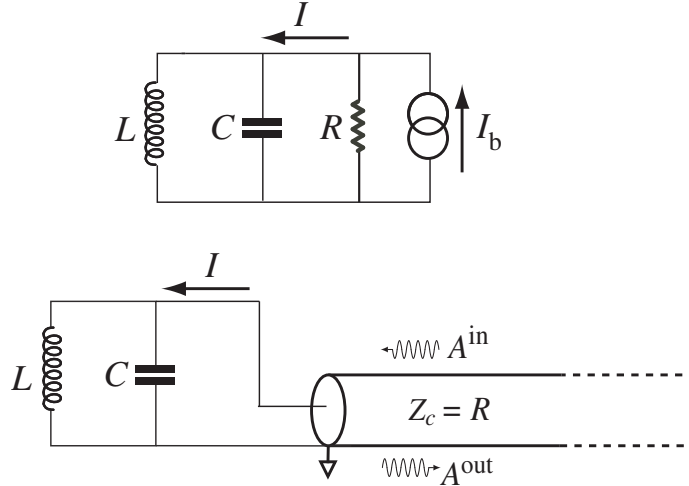


Figure B.1: **Input-output theory.** Top panel shows a damped LC oscillator driven by an RF current source. Bottom panel shows the equivalent circuit in which the current source and its internal resistance have been replaced by a semi-infinite transmission line (input output analog). The two cases are equivalent from the point of view of the LC oscillator if we make the identification  $Z_C = R$  and  $A^{\text{in}} = \sqrt{R}I_b/2$ .

It is straightforward to obtain constitutive relations linking input, output and internal fields of the amplifier by imposing the appropriate boundary conditions at the termination of the line ( $z=0$ )

$$V(t) = V^{\text{in}}(t) + V^{\text{out}}(t); \quad I(t) = I^{\text{in}}(t) - I^{\text{out}}(t) \quad (\text{B.2})$$

where we have used the relation  $V^{\text{in/out}} = \sqrt{Z_c}A^{\text{in/out}}$  and  $I^{\text{in/out}} = \frac{A^{\text{in/out}}}{\sqrt{Z_c}}$ .

It is useful to define the quantities  $a[\omega]$  as

$$\sqrt{\frac{\hbar|\omega|}{2}}a[\omega] = A[\omega] \quad (\text{B.3})$$

where  $A[\omega] = \frac{1}{\sqrt{2\pi}} \int dt A(t) \exp(i\omega t)$ . Here the square brackets imply that the frequency  $\omega$  can be either positive or negative. The dynamics of any system can be,

thus, written down as a matrix equation of the form <sup>1</sup>,

$$a^{\alpha,\text{out}}[\omega] = \int \sum_{\beta} \mathbb{S}^{\alpha\beta}(\omega, \omega') a^{\beta,\text{in}}[\omega'] d\omega', \quad (\text{B.4})$$

where  $\mathbb{S}$  denotes the *scattering matrix* describing the relationship between different incoming and outgoing modes. The participating modes of the system are indexed by  $(\alpha, \beta)$  and are distinct from each other spatially (i.e. leaving or entering the system on different ports). In case the device is time-translation invariant, the element  $S^{\alpha\beta}(\omega, \omega') = S^{\alpha\beta}(\omega)\delta(\omega - \omega')$  and can be interpreted directly using the formula,

$$\mathbb{S}^{\alpha\beta}(\omega) = \left. \frac{a^{\alpha,\text{out}}[\omega]}{a^{\beta,\text{in}}[\omega]} \right|_{a^{\gamma,\text{in}}=0 \forall \gamma \neq \beta} \quad (\text{B.5})$$

which leads to

$$a^{\gamma,\text{in}} = 0 \Rightarrow V^{\gamma} + Z_c I^{\gamma} = 0 \quad [\text{Eqs. (B.1) and (B.3)}] \quad (\text{B.6})$$

$$\Rightarrow \frac{V^{\gamma}}{I^{\gamma}} = -Z_c, \quad (\text{B.7})$$

i.e. all other ports are terminated with an impedance equal to the characteristic impedance of the line  $Z_c$  (or *matched*).

In case the device mixes discrete frequencies or temporal channels, we can consider the scattering as mixing of distinct tones each represented as a dirac-delta function in the spectrum,  $a^{\text{in}}[\omega'] = \sum_j a_j^{\text{in}} \delta(\omega' - \omega_j)$ . In this case Eq. (B.4) simplifies to

$$a_i^{\alpha,\text{out}} = \sum_{\beta} \sum_j \mathbb{S}_{ij}^{\alpha\beta} a_j^{\beta,\text{in}}, \quad (\text{B.8})$$

---

<sup>1</sup>There is an underlying assumption of linear response here which means that the output field depends linearly on the input fields  $A^{\text{out}}(t) = \int_{-\infty}^t S(t, t') A^{\text{in}}(t') dt'$ .

where the subscripts index temporal channels and superscripts index spatial ports. We note that in case of a dispersive process *without* gain, the scattering is restricted to positive frequencies alone while in the case *with* gain the scattering mixes positive and negative frequency components.

Besides being a gauge-independent choice, unlike the Hamiltonian description, the scattering formalism also offers a natural generalization to a quantum mechanical description as the normalized wave amplitudes  $a_{[\mp|\omega]}$  in Eq. (B.3) play the role of bosonic creation and annihilation operators, as defined for a harmonic oscillator, respectively. The input-output scattering amplitudes obey the following well-known field theoretical commutation relation [Courty et al., 1999]

$$[\hat{a}^{\text{in/out}}[\omega], \hat{a}^{\text{in/out}}[\omega']] = \text{sgn}[\omega] \delta(\omega + \omega'). \quad (\text{B.9})$$

The fluctuations of field creation and annihilation operators is characterized by the corresponding noise spectrum in thermal equilibrium

$$\begin{aligned} \langle \{ \hat{a}^{\text{in}}[\omega], \hat{a}^{\text{in}}[\omega'] \} \rangle_T &= 2S_{aa}[\omega] \delta(\omega + \omega') \\ S_{aa}[\omega] &= \text{sgn}(\omega) \left[ \frac{1}{\exp(\frac{\hbar\omega}{k_B T}) - 1} + \frac{1}{2} \right] = \frac{1}{2} \coth \frac{\hbar|\omega|}{2k_B T}. \end{aligned} \quad (\text{B.10})$$

The quantity  $\hbar\omega S_{aa}^{\text{in}}$  denotes the total energy per mode and reduces to  $\frac{\hbar\omega}{2}$  in the limit of zero temperature (vacuum fluctuations) and the classical limit of  $k_B T$  in the limit of high temperature. Eqs. (B.9) and (B.10) are valid over the entire frequency range, including the negative frequencies. We can return to the conventional description restricted to only positive frequencies by the identification<sup>2</sup>

$$\hat{a}[-\omega] \rightarrow \hat{a}^\dagger[\omega].$$

---

<sup>2</sup>This follows from the fact that the corresponding time domain amplitude  $A(t)$  in Eq. (B.3) is real valued.

The preceding equations lead us to define the ordered spectral density

$$\langle \hat{A}[\omega] \hat{A}[\omega'] \rangle = \frac{\hbar\omega}{4} \left[ \coth \left( \frac{\hbar\omega}{2k_B T} \right) + 1 \right] \delta(\omega + \omega'). \quad (\text{B.11})$$

Thus, we can easily write the fluctuations of the voltage across the resistor

$$\langle \hat{V}[\omega] \hat{V}[\omega'] \rangle = \frac{Z_c \hbar\omega}{4} \left[ \coth \left( \frac{\hbar\omega}{2k_B T} \right) + 1 \right] \delta(\omega + \omega') \quad (\text{B.12})$$

which follows from  $V^{\text{in/out}} = \sqrt{Z_c} A^{\text{in/out}}$ .

The validity of this crossover to quantum description lies in the fact that in case of parametric interaction, the difference between the classical and quantum evolution vanishes when the number of photons in the line is large or the coupling of the system to reservoir is weak [[Courty and Reynaud, 1992](#)]. We can then regard the quantum fluctuations to be driven by classical random fields, obeying classical equations of motion.

---

## Modulation ellipse

---

This scheme provides a geometrical visualization of superposition of two sinusoidal signals as an ellipse in the plane defined by the quadratures  $I$  and  $Q$ . In general for any two complex phasors  $\vec{a}$  and  $\vec{b}$  rotating in opposite directions

$$\begin{aligned}
 \vec{a}e^{i\omega t} + \vec{b}e^{-i\omega t} &= (a_1 + ia_2)e^{i\omega t} + (b_1 + ib_2)e^{-i\omega t} \\
 &= (a_1 + ia_2)(\cos \omega t + i \sin \omega t) + (b_1 + ib_2)(\cos \omega t - i \sin \omega t) \\
 &= [a_1 \cos \omega t - a_2 \sin \omega t + i(a_2 \cos \omega t + a_1 \sin \omega t)] \\
 &\quad + [b_1 \cos \omega t + b_2 \sin \omega t + i(b_2 \cos \omega t - b_1 \sin \omega t)] \\
 &= [a_1 \cos \omega t - a_2 \sin \omega t + b_1 \cos \omega t + b_2 \sin \omega t] \\
 &\quad + i[a_2 \cos \omega t + a_1 \sin \omega t + b_2 \cos \omega t - b_1 \sin \omega t] \\
 &= \underbrace{\text{Re}[(\vec{a} + \vec{b}^*)e^{i\omega t}]}_I + i \underbrace{\text{Im}[(\vec{a} - \vec{b}^*)e^{i\omega t}]}_Q. \tag{C.1}
 \end{aligned}$$

The magnitudes and phases of the two complex signals (4 quantities in total) are encoded as properties of a colored ellipse in the  $I - -Q$  plane: the semi-major axis of the ellipse equals  $\rho_+ = |a| + |b|$  while the semi minor axis equals  $\rho_- = ||a| - |b||$ , the angle with the  $I$  axis equals  $(\theta_a - \theta_b)/2$  and the location of the colors on the ellipse represents the phase angle  $(\theta_a + \theta_b)/2$ .

Now we present examples of two different kinds of phase rotations and the resultant transformations (“rotations”) of the modulation ellipse (see Fig. C.1(a)-(d) for additional examples clarifying the modulation ellipse representation).

- *Phase shift* The action of a phase shifter which performs frequency independent phase rotations of both the phasors can be described using the transformations:

$$a \mapsto ae^{i\theta} \quad \text{and} \quad b \mapsto be^{i\theta}. \quad (\text{C.2})$$

On using the above and performing the analysis in the  $IQ$  plane, we obtain the expressions for new coordinates as

$$I = \text{Re}[ae^{i(\omega t + \theta)} + b^*e^{i(\omega t - \theta)}], \quad (\text{C.3})$$

$$Q = \text{Im}[ae^{i(\omega t + \theta)} - b^*e^{i(\omega t - \theta)}]. \quad (\text{C.4})$$

The action of such an operation can be easily visualized using the modulation ellipse, as shown in Fig. C.1(e).

- *Free evolution* In contrast to the transformation described above, we now consider the rotation performed by a mere time evolution of the two counter-rotating phasors (say by passage through a transmission line). In such a case, the phases of the two signals continue to evolve in opposite directions collecting a phase  $\delta$  in time  $t$  ( $\delta = \omega t$ ),

$$a \mapsto ae^{+i\delta} \quad \text{and} \quad b \mapsto be^{-i\delta}. \quad (\text{C.5})$$

The  $IQ$  coordinates are calculated as

$$I = \text{Re}[(a + b^*)e^{i(\omega t + \delta)}], \quad (\text{C.6})$$

$$Q = \text{Im}[(a - b^*)e^{i(\omega t + \delta)}]. \quad (\text{C.7})$$

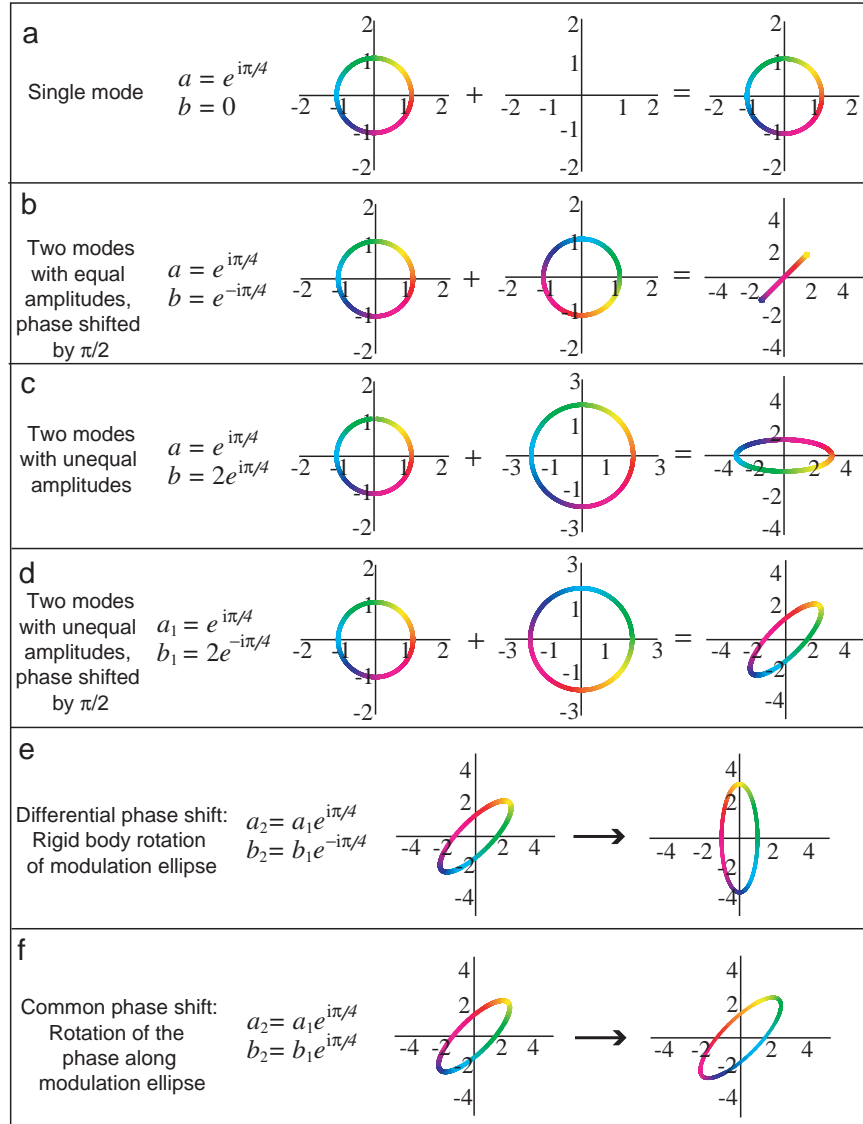


**Figure C.1: Modulation ellipse representation of two phasors.** In each of the panels, the first column describes the phasors under consideration, the second column gives a precise mathematical formula for them and the third column shows the corresponding modulation ellipse. In **a-d**, we show both the input modes and the resultant modulation ellipse. The tilt of the ellipse with respect to the  $I$  axis represents the relative phase between the two modes  $[(\theta_a - \theta_b)/2]$  while the color along the ellipse represents the average initial phase of the two modes  $[(\theta_a + \theta_b)/2]$ , with yellow representing the position of 0 (or  $2\pi$ ). Figs. **(e)** and **(f)** represent the resulting ellipses on performing the indicated transformations on the ellipse in **(d)**.

It is immediately evident that, under time evolution, there is only a trivial phase accumulation leading to change of relative positions of the two phasors along the circumference of the modulation ellipse with no rigid rotation of the ellipse, Fig. C.1(f).

## Representation of modulation schemes

Modulation ellipse representation also finds itself useful as a concise representation of different modulation schemes such as amplitude modulation and frequency (or phase) modulation. To elaborate on how amplitude and frequency modulation map on an  $I - Q$  plane, let us do the following brief exercise:

- Double sideband Amplitude Modulation (AM): In AM the signal amplitude of a high frequency carrier is modulated by a small low frequency signal as

$$\begin{aligned}
 A_c(t) \cos(\omega_c t + \phi) &= [A_0 + a_m \cos \omega_m t] \cos(\omega_c t + \phi) \\
 &= A_0 \cos(\omega_c t + \phi) + a_m \cos(\omega_c t + \phi) \cos \omega_m t \\
 &= A_0 \cos(\omega_c t + \phi) + \frac{a_m}{2} (\cos[(\omega_c + \omega_m)t + \phi] + \cos[(\omega_c - \omega_m)t + \phi]) \\
 &\xrightarrow[\text{and } -\omega_- \text{ components}]{\text{collecting } \omega_+} e^{i(\omega_+ t + \phi)} + e^{-i(\omega_- t + \phi)} \tag{C.8}
 \end{aligned}$$

- Double sideband Frequency Modulation (FM): In FM the frequency of a high frequency carrier is modulated by a small low frequency signal as

$$\begin{aligned}
 A_c \cos(\omega_c t + \phi) &= A_0 \cos(\omega_c t + \phi + a_m \cos \omega_m t) \\
 &= A_0 \cos(\omega_c t + \phi) + a_m A_0 \sin(\omega_c t + \phi) \cos \omega_m t \\
 &= A_0 \cos(\omega_c t + \phi) + \frac{a_m A_0}{2} (\sin[(\omega_c + \omega_m)t + \phi] + \sin[(\omega_c - \omega_m)t + \phi]) \\
 &\xrightarrow[\text{and } -\omega_- \text{ components}]{\text{collecting } \omega_+} e^{i(\omega_+ t + \phi)} - e^{-i(\omega_- t + \phi)} \tag{C.9}
 \end{aligned}$$

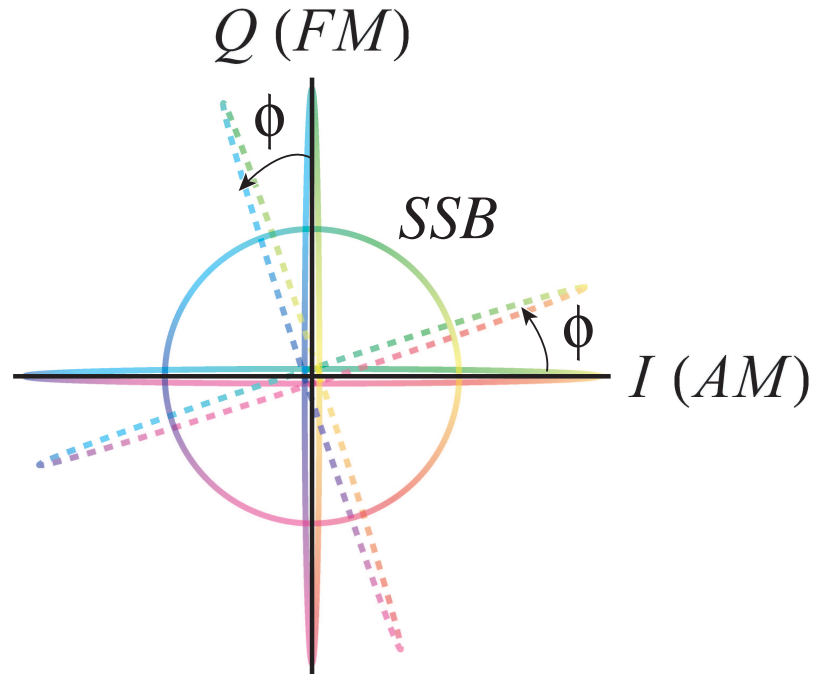


Figure C.2: Representation of different modulation schemes. Double sideband AM ( $I$ -axis), double sideband FM ( $Q$ -axis) and single sideband modulation (circle). The carrier phase  $\phi$  rotates the ellipses in the  $I - Q$  plane.

Eqs. (C.8) and (C.9), in conjunction with Eq. (C.7) show that an AM signal is encoded along the  $I$ -axis while an FM signal is encoded along the  $Q$ -axis in the modulation ellipse representation. Further, any single side band modulation scheme will be encoded as a circle, similar to that shown in Fig. C.1(a).

---

## Derivation of the JRM eigenmodes

---

For complicated networks such as the Josephson ring modulator (JRM) depicted in Fig. 1.10, it is advantageous to work with the eigenmodes of the system as they constitute the simplest irreducible basis describing the dynamics of such complicated networks. In other words, the resultant dynamical equations are the simplest in this representation.

We derive the eigenmodes of the JRM using a method based on Kirchhoff's current and voltage laws. We consider the JRM circuit shown in Fig. D.1, where the capacitance  $C$  connected to each node provides a simple model for the environment in each arm of the ring modulator. Note that the circuit has 4 independent, fully dynamic loops and 4 independent, fully dynamic nodes. Neither the degrees of freedom of the loops or the degrees of freedom are normal modes. They are all coupled to each other, even if we linearize the current-flux relationship of the junctions. We will focus on the node degrees of freedom, but a similar analysis could be developed using the loops of the circuits. The currents flowing through the capacitances  $C$  connected to the nodes  $\{1, 2, 3, 4\}$  are denoted as  $\mathbf{I}_C = (I^{(1)}, I^{(2)}, I^{(3)}, I^{(4)})$  and the respective voltages across the capacitances are denoted as  $\mathbf{V}_C = (V^{(1)}, V^{(2)}, V^{(3)}, V^{(4)})$ , with the usual sign convention imposed by the direction of current. We write the equations for voltage across the capacitance

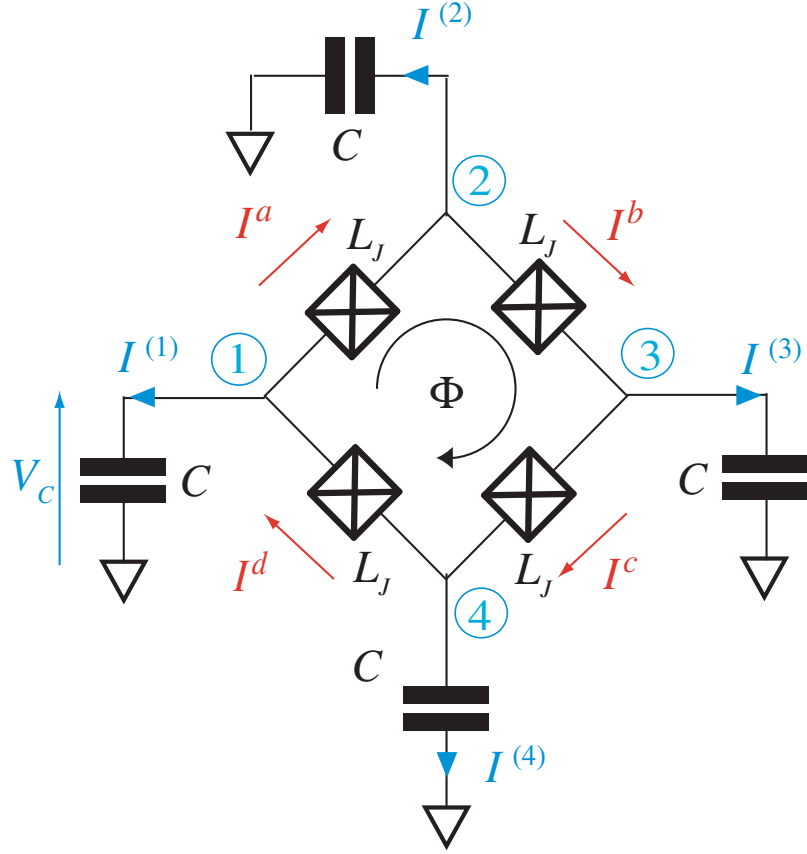


Figure D.1: **Simplified circuit model for the Josephson Ring Modulator (JRM).** Josephson Ring Modulator with capacitances to ground in each arm. All capacitances are connected to a common RF ground. We ignore the capacitance of the junction here.

at each node as

$$\mathbf{V}_C = \mathbb{Z}\mathbf{I}_C. \quad (\text{D.1})$$

Here  $\mathbf{V}_C$ ,  $\mathbf{I}_C$  represent column vectors with different components referring to the respective nodes. The capacitance matrix  $\mathbb{Z}$  of the network,

$$\mathbb{Z} = (j\omega C)^{-1}\mathbb{U}, \quad (\text{D.2})$$

is diagonal in this node representation ( $\mathbb{U}$  represents the unit matrix of proper dimensions, here  $4 \times 4$ ).

Similarly, for the four inductive branches  $\{a, b, c, d\}$ , a constitutive relation can be written as,

$$\mathbf{I}_{\mathbf{L}} = \mathbb{Y}\mathbf{V}_{\mathbf{L}}, \quad (\text{D.3})$$

with  $\mathbf{I}_{\mathbf{L}} = (I^a, I^b, I^c, I^d)$ ,  $\mathbf{V}_{\mathbf{L}} = (V^a, V^b, V^c, V^d)$  and

$$\mathbb{Y} = (j\omega L_J)^{-1}\mathbb{U}. \quad (\text{D.4})$$

It must be noted from Eq. (D.4) that we consider only the linear part of the inductance of the Josephson junctions for the purpose of deriving normal modes of the JRM. In case the effective nonlinearity is perturbative in nature (as is the case for most of the devices), this should not modify the mode structure of the ring considerably.

We now define the matrices  $\mathbb{H}$  and  $\mathbb{W}$  for the JRM circuit, using Kirchhoff's current and voltage laws:

$$\begin{aligned} \begin{pmatrix} I^{(1)} \\ I^{(2)} \\ I^{(3)} \\ I^{(4)} \end{pmatrix} &= \begin{pmatrix} -1 & 0 & 0 & 1 \\ 1 & -1 & 0 & 0 \\ 0 & 1 & -1 & 0 \\ 0 & 0 & 1 & -1 \end{pmatrix} \begin{pmatrix} I^a \\ I^b \\ I^c \\ I^d \end{pmatrix} \\ \Rightarrow \mathbf{I}_{\mathbf{C}} &= \mathbb{H}_{L \rightarrow C} \mathbf{I}_{\mathbf{L}} \end{aligned} \quad (\text{D.5})$$

and

$$\begin{aligned} \begin{pmatrix} V^a \\ V^b \\ V^c \\ V^d \end{pmatrix} &= \begin{pmatrix} 1 & -1 & 0 & 0 \\ 0 & 1 & -1 & 0 \\ 0 & 0 & 1 & -1 \\ -1 & 0 & 0 & 1 \end{pmatrix} \begin{pmatrix} V^{(1)} \\ V^{(2)} \\ V^{(3)} \\ V^{(4)} \end{pmatrix} \\ \Rightarrow \mathbf{V}_{\mathbf{L}} &= \mathbb{W}_{C \rightarrow L} \mathbf{V}_{\mathbf{C}}. \end{aligned} \quad (\text{D.6})$$

On using Eqs. (D.5), (D.6) in (D.2), (D.4), we obtain the following matrix equation:

$$\begin{pmatrix} \mathbf{V}_C \\ \mathbf{I}_C \end{pmatrix} = \begin{pmatrix} 0 & \mathbb{Z} \\ \mathbb{H}_{L \rightarrow C} \mathbb{Y} \mathbb{W}_{C \rightarrow L} & 0 \end{pmatrix} \begin{pmatrix} \mathbf{V}_C \\ \mathbf{I}_C \end{pmatrix}. \quad (\text{D.7})$$

Eq. (D.7) has a nontrivial solution only if the determinant of the coefficient matrix is zero. This leads to the condition

$$\mathbf{U} - \tilde{\Omega} = 0, \quad (\text{D.8})$$

where

$$\tilde{\Omega} = \mathbb{Z} \mathbb{H}_{L \rightarrow C} \mathbb{Y} \mathbb{W}_{C \rightarrow L}^1. \quad (\text{D.9})$$

We can immediately obtain the eigenfrequencies of the circuit from the roots by diagonalizing the  $\tilde{\Omega}$  matrix in Eq. (D.8),

$$\mathbb{M}^T \tilde{\Omega} \mathbb{M} = \mathbf{\Omega} = \frac{\omega_0^2}{\omega^2} \begin{pmatrix} 4 & 0 & 0 & 0 \\ 0 & 2 & 0 & 0 \\ 0 & 0 & 2 & 0 \\ 0 & 0 & 0 & 0 \end{pmatrix}, \quad (\text{D.10})$$

where  $\omega_0 = 1/\sqrt{L_J C}$ . The respective mode vectors can be read off from the

---

<sup>1</sup>Note that the matrices  $\mathbb{W}$  and  $\mathbb{H}$  represent singular or *non-invertible* transformations, as seen from the fact that their determinant is zero. This occurs in circuits like JRM which have purely inductive loops not connected to any capacitors or purely capacitive nodes not connected to any inductors. One way to work around such singular configurations is to include extra elements (such as a large capacitor interrupting the JRM ring) and calculate the dynamics in the vanishing limit of the spurious elements. Another way to alleviate such singular behavior is to work in an extended basis, explicitly including internal degrees of freedom such as the circulating current in the ring. The presence of such networks, however, is not necessarily pathological for the calculation. For instance, Eq. (D.8) shows us that only a product of  $\mathbb{W}$  and  $\mathbb{H}$  matrices with  $\mathbb{Z}$  and  $\mathbb{Y}$  is required. Of course, the singularity leaves its imprint in the final diagonalized product  $\tilde{\Omega}$  with one of the eigenfrequencies being zero, corresponding to a “W” mode which doesn’t have any dynamical significance.

columns of the orthogonal matrix  $\mathbb{M}$  as

$$I^Z = \frac{-I^{(1)} + I^{(2)} - I^{(3)} + I^{(4)}}{2}, \quad (\text{D.11a})$$

$$I^Y = \frac{-I^{(2)} + I^{(4)}}{\sqrt{2}}, \quad (\text{D.11b})$$

$$I^X = \frac{-I^{(1)} + I^{(3)}}{\sqrt{2}}, \quad (\text{D.11c})$$

$$I^W = \frac{I^{(1)} + I^{(2)} + I^{(3)} + I^{(4)}}{2}. \quad (\text{D.11d})$$

The resultant current configurations of the JRM circuit for different modes are shown in Fig. (1.10).

---

## Loop Variables for the dc SQUID

---

In this appendix we establish the correspondence between the differential mode variables introduced in the analysis of sections 4.1 and 4.2 and the input variables required for the hybrid representation discussed in section 4.3. The output variables in the two representations have a simple relationship as explained in section 4.3.

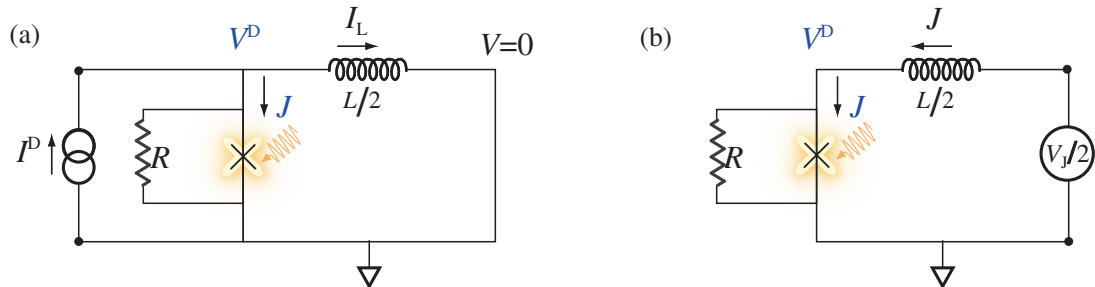


Figure E.1: **Equivalence between the SQUID differential mode and the op-amp input variables.** Here we have used the symmetric version of the SQUID ring to divide the ring along the equipotential for simplicity. The circuit in (a) models the device as an impedance response function to an imposed current source  $I^D$ , as a result of which a voltage drop  $\pm V^D$  develops across the left (right) junction. (b) Hybrid representation for the SQUID, which models the input response by introducing a differential voltage source in the squid loop and recording the current that flows across the junction. The junction at this point is replaced with an effective junction pumped using the various Josephson harmonics generated by the static bias current (also see Fig. 4.4(c)).

Figure E.1 shows the two representations [cf. Figs. 4.9(b) and (c)], one in terms

of differential mode quantities ( $V^D, I^D$ ) suitable for a scattering or matched representation (since the input and output impedances are just the transmission line impedance) and the other in terms of a circulating current  $J$  and a loop voltage  $V_J$ , which are the relevant input quantities for the device in an unmatched hybrid description. In Fig. E.1(a) Kirchhoff's current law gives,

$$J = I^D - I_L, \quad (\text{E.1})$$

while in Fig. E.1(b), from Kirchhoff's voltage law, we have

$$-\frac{V_J}{2} = V^D + \frac{i\omega L}{2}J, \quad (\text{E.2})$$

with  $J = I_L$ .

To establish the equivalence of the two representations from the point of view of the junction, we require the voltage across the junction  $V^D$  and current through the junction  $J$  to be conserved (Fig. E.1). Thus using Eq. (E.1) in (E.2), we obtain

$$V_J = -i\omega L I^D. \quad (\text{E.3})$$

Similarly it is easily seen that the circulating current  $J$  is given as

$$J = \frac{2V^D}{i\omega L}. \quad (\text{E.4})$$

---

## Static analog circuit for the SQUID

---

The SQUID can be thought of as a current amplifier with a current transferred from a low-impedance input port to a high-impedance output port. This description is very close to the FET dual model with the gain given by a transimpedance instead of a transconductance. The equivalent ‘current gain’ of such a device (Fig. F.1) for frequencies sufficiently close to zero [ $\omega_m \ll \rho_{\text{in}}R/L = \omega_0/(\pi\beta_L)$  to be precise] can be modelled as:

$$\frac{I_{\text{out}}}{I_{\text{in}}} \approx \frac{V_{\Phi}L}{R_D}. \quad (\text{F.1})$$

This leads to a power gain,

$$G_P^{\text{dc}} = \left( \frac{I_{\text{out}}}{I_{\text{in}}} \right)^2 \frac{R_D}{\text{Re}[Z_{\text{in}}]}. \quad (\text{F.2})$$

For frequencies of interest,  $\text{Re}[Z_{\text{in}}] \approx \omega_m^2 L^2 / (\rho_{\text{in}}R)$ . Using this result in Eq. (F.2), we obtain the power gain

$$G_P^{\text{dc}} = \frac{\rho_{\text{in}}}{\rho_{\text{out}}} \left( \frac{V_{\Phi}}{\omega_m} \right)^2, \quad (\text{F.3})$$

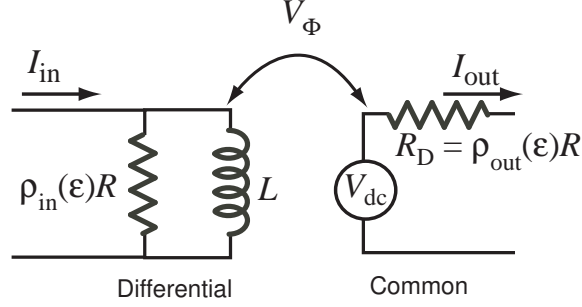


Figure F.1: **Equivalent low frequency circuit for a SQUID for calculation of unilateral power gain.** The input circuit is modelled as an effective impedance viewed by a low frequency differential mode current. The output circuit impedance comprises a bias-dependent resistor denoting the dynamic impedance of the junction, that converts the output voltage to a corresponding output current. The net “transimpedance” is given by the dc flux-to-voltage transfer function of the device. The symbols  $\rho_{in, out}$  denote bias-dependent constants of order unity.

which can be rewritten as,

$$G_P^{\text{dc}} \approx \rho_g \left( \frac{\omega_0}{\omega_m} \right)^2 \quad (\text{F.4})$$

with  $\rho_g$  as a bias-dependent and frequency-independent constant. Here we have used the relation  $V_{\Phi}^{\text{opt}} = R/L = \omega_0/\pi$  [Clarke and Braginski, 2006] for  $\beta_L = 1$ . This shows that the gain drops quadratically with increasing signal frequency, and no power gain is obtained for signal frequencies close to the plasma frequency of each junction in the SQUID. This frequency dependence of the power gain is borne out by the full rf analysis shown in Fig. 4.10(b). Figure F.2 shows a comparison of gain calculated using quasistatic response functions as shown in Eq. (F.3) and a full rf calculation at low frequencies [see Fig. 4.10(a)]. The agreement is better for lower values of  $\varepsilon$  where high frequency components of the device are less significant. Also, the impedance matrix calculation generates extra terms due to the inversion operation involved in its calculation [cf. Eq. (4.27)] — this leads to higher order corrections absent from the purely quasistatic calculation.

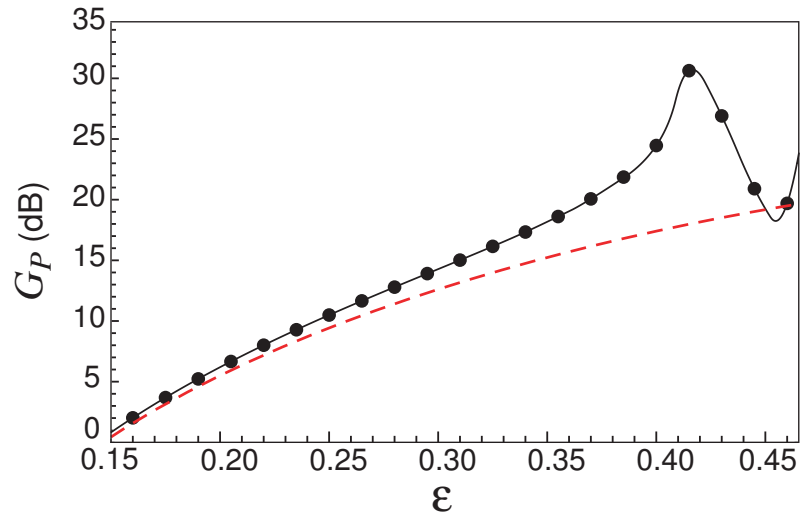


Figure F.2: Comparison of the power gain as a function of bias  $\varepsilon = I_0/I_B$  calculated using a full rf calculation (solid black line) and a purely quasistatic calculation (dashed red line) of Eq. (F.3). For the quasistatic gain calculation,  $V_\Phi$  and  $\rho_{\text{in,out}}$  were obtained from the  $I - V$  characteristics evaluated in Sec. 4.2.1.

---

## Bibliography

---

- [[Abdo et al., 2013a](#)] B. Abdo, A. Kamal, and M. Devoret. Nondegenerate three-wave mixing with the Josephson ring modulator. *Phys. Rev. B*, 87:014508, 2013a.
- [[Abdo et al., 2013b](#)] B. Abdo, K. Sliwa, L. Frunzio, and M. Devoret. Directional amplification with a Josephson circuit. 2013b. [arXiv:1302.4663](#).
- [[Bergeal et al., 2010a](#)] N. Bergeal, F. Schackert, M. Metcalfe, R. Vijay, V. E. Manucharyan, L. Frunzio, D. E. Prober, R. J. Schoelkopf, S. M. Girvin, and M. H. Devoret. Phase-preserving amplification near the quantum limit with a Josephson ring modulator. *Nature*, 465:64, 2010a.
- [[Bergeal et al., 2010b](#)] N. Bergeal, R. Vijay, V. E. Manucharyan, I. Siddiqi, R. J. Schoelkopf, S. M. Girvin, and M. H. Devoret. Analog information processing at the quantum limit with a Josephson ring modulator. *Nat Phys*, 6:296–302, 2010b.
- [[Bradley et al., 2003](#)] R. Bradley, J. Clarke, D. Kinion, L. J. Rosenberg, K. van Bibber, S. Matsuki, M. Mück, and P. Sikivie. Microwave cavity searches for dark-matter axions. *Rev. Mod. Phys.*, 75:777–817, 2003.
- [[Castellanos-Beltran and Lehnert, 2007](#)] M. A. Castellanos-Beltran and K. W. Lehnert. Widely tunable parametric amplifier based on a superconducting quantum interference device array resonator. *Appl. Phys. Lett.*, 91(8):083509, 2007.

- [[Caves, 1982](#)] C. M. Caves. Quantum limits on noise in linear amplifiers. *Phys. Rev. D*, 26:1817–1839, 1982.
- [[Clarke and Braginski, 2004](#)] J. Clarke and A. I. Braginski, editors. *The SQUID Handbook Vol. I: Fundamentals and Technology of SQUIDs and SQUID Systems*. Wiley-VCH, Weinheim, Germany, 2004.
- [[Clarke and Braginski, 2006](#)] J. Clarke and A. I. Braginski, editors. *The SQUID Handbook Vol. II: Applications of SQUIDs and SQUID Systems*. Wiley-VCH, Weinheim, Germany, 2006.
- [[Clarke et al., 2011](#)] J. Clarke, M. H. Devoret, and A. Kamal. Squid amplifiers. In *Les Houches, Quantum Machines*, 2011.
- [[Clerk, 2006](#)] A. A. Clerk. Backaction noise in strongly interacting systems: The dc squid and the interacting quantum point contact. *Phys. Rev. Lett.*, 96:056801, 2006.
- [[Clerk et al., 2003](#)] A. A. Clerk, S. M. Girvin, and A. D. Stone. Quantum-limited measurement and information in mesoscopic detectors. *Phys. Rev. B*, 67(16):165324, 2003.
- [[Clerk et al., 2010](#)] A. A. Clerk, M. H. Devoret, S. M. Girvin, F. Marquardt, and R. J. Schoelkopf. Introduction to quantum noise, measurement, and amplification. *Rev. Mod. Phys.*, 82:1155–1208, 2010.
- [[Courty and Reynaud, 1992](#)] J.-M. Courty and S. Reynaud. Generalized linear input-output theory for quantum fluctuations. *Phys. Rev. A*, 46(5):2766–2777, 1992.
- [[Courty et al., 1999](#)] J.-M. Courty, F. Grassia, and S. Reynaud. Quantum noise in ideal operational amplifiers. *Europhys. Lett.*, 46(1):31–37, 1999.

- [[Danilov et al., 1983](#)] V. Danilov, K. Likharev, and A. Zorin. Quantum noise in squids. *IEEE Transactions on Magnetics*, 19(3):572 – 575, 1983.
- [[Devoret, 1995](#)] M. H. Devoret. Quantum fluctuations in electrical circuits. In *Les Houches Session LXIII, Quantum Fluctuations*, pages 351–386, 1995.
- [[Devoret and Schoelkopf, 2000](#)] M. H. Devoret and R. J. Schoelkopf. Amplifying quantum signals with the single-electron transistor. *Nature*, 406:1039, 2000.
- [[Etaki et al., 2008](#)] S. Etaki, M. Poot, I. Mahboob, K. Onomitsu, H. Yamaguchi, and H. S. J. van der Zant. Motion detection of a micromechanical resonator embedded in a d.c. squid. *Nature Physics*, 4:785, 2008.
- [[Flach et al., 2000](#)] S. Flach, O. Yevtushenko, and Y. Zolotaryuk. Directed current due to broken time-space symmetry. *Phys. Rev. Lett.*, 84:2358–2361, 2000.
- [[Hanggi and Marchesoni, 2009](#)] P. Hanggi and F. Marchesoni. Artificial brownian motors: Controlling transport on the nanoscale. *Rev. Mod. Phys.*, 81:387–442, 2009.
- [[Hansryd et al., 2002](#)] J. Hansryd, P. Andrekson, M. Westlund, J. Li, and P.-O. Hedekvist. Fiber-based optical parametric amplifiers and their applications. *Selected Topics in Quantum Electronics, IEEE Journal of*, 8(3):506–520, 2002.
- [[Henry et al., 1981](#)] R. W. Henry, D. E. Prober, and A. Davidson. Simple electronic analog of a Josephson junction. *Am J. Phys.*, 49:1035, 1981.
- [[Ho Eom et al., 2012](#)] B. Ho Eom, P. K. Day, H. G. LeDuc, and J. Zmuidzinas. A wide-band, low-noise superconducting amplifier with high dynamic range. *Nat. Phys.*, 8:623–627, 2012.
- [[Hoffman et al., 2011](#)] A. J. Hoffman, S. J. Srinivasan, S. Schmidt, L. Spietz, J. Aumentado, H. E. Türeci, and A. A. Houck. Dispersive photon blockade in a superconducting circuit. *Phys. Rev. Lett.*, 107:053602, 2011.

- [[Hover et al., 2012](#)] D. Hover, Y.-F. Chen, G. J. Ribeill, S. Zhu, S. Sendelbach, and R. McDermott. Superconducting low-inductance undulatory galvanometer microwave amplifier. *Applied Physics Letters*, 100:063503, 2012.
- [[Ingold and Grabert, 1999](#)] G.-L. Ingold and H. Grabert. Effect of zero point phase fluctuations on Josephson tunneling. *Phys. Rev. Lett.*, 83:3721–3724, 1999.
- [[Ingold et al., 1994](#)] G.-L. Ingold, H. Grabert, and U. Eberhardt. Cooper-pair current through ultrasmall Josephson junctions. *Phys. Rev. B*, 50:395–402, 1994.
- [[Joyez et al., 1999](#)] P. Joyez, D. Vion, M. Gtz, M. H. Devoret, and D. Esteve. The Josephson effect in nanoscale tunnel junctions. *Journal of Superconductivity*, 12:757–766, 1999.
- [[Kamal et al., 2009](#)] A. Kamal, A. Marblestone, and M. Devoret. Signal-to-pump back action and self-oscillation in double-pump Josephson parametric amplifier. *Phys. Rev. B*, 79:184301, 2009.
- [[Kamal et al., 2011](#)] A. Kamal, J. Clarke, and M. H. Devoret. Noiseless non-reciprocity in a parametric active device. *Nature Physics*, 7:311–315, 2011.
- [[Kamal et al., 2012](#)] A. Kamal, A. Roy, J. Clarke, and M. H. Devoret. *in preparation*, 2012.
- [[Kane et al., 2002](#)] C. L. Kane, R. Mukhopadhyay, and T. C. Lubensky. Fractional quantum hall effect in an array of quantum wires. *Phys. Rev. Lett.*, 88:036401, 2002.
- [[Kapitulnik et al., 2009](#)] A. Kapitulnik, J. Xia, E. Schemm, and A. Palevski. *New J. Phys.*, 11:055060, 2009.
- [[Kinion and Clarke, 2011](#)] D. Kinion and J. Clarke. Superconducting quantum interference device as a near-quantum-limited amplifier for the axion dark-matter experiment. *Applied Physics Letters*, 98(20):202503, 2011.

- [[Koch et al., 2010](#)] J. Koch, A. A. Houck, K. L. Hur, and S. M. Girvin. Time-reversal-symmetry breaking in circuit-qed-based photon lattices. *Phys. Rev. A*, 82:043811, 2010.
- [[Koch et al., 1980](#)] R. H. Koch, D. J. Van Harlingen, and J. Clarke. Quantum-noise theory for the resistively shunted Josephson junction. *Phys. Rev. Lett.*, 45:2132–2135, 1980.
- [[Koch et al., 1981](#)] R. H. Koch, D. J. V. Harlingen, and J. Clarke. Quantum noise theory for the dc squid. *Applied Physics Letters*, 38(5):380–382, 1981.
- [[Landau and Lifshitz, 1984](#)] L. D. Landau and E. M. Lifshitz. *Electrodynamics of continuous media*. Pergamon Press, (second edition) edition, 1984.
- [[Leibbrandt et al., 2009](#)] D. R. Leibbrandt, J. Labaziewicz, V. Vuletić, and I. L. Chuang. Cavity sideband cooling of a single trapped ion. *Phys. Rev. Lett.*, 103:103001, 2009.
- [[Likharev, 1996](#)] K. K. Likharev. *Dynamics of Josephson junctions and circuits*. Gordon and Breach, Amsterdam, 1996.
- [[Maletinsky et al., 2007](#)] P. Maletinsky, C. W. Lai, A. Badolato, and A. Imamoglu. Non-linear dynamics of quantum dot nuclear spins. *Phys. Rev. B*, 75:035409, 2007.
- [[Mallet et al., 2009](#)] F. Mallet, F. R. Ong, A. Palacios-Laloy, F. Nguyen, P. Bertet, D. Vion, and D. Esteve. Single-shot qubit readout in circuit quantum electrodynamics. *Nat Phys*, 5:791–795, 2009.
- [[Marhic et al., 2001](#)] M. E. Marhic, K. K. Y. Wong, M. C. Ho, and L. G. Kazovsky. 92% pump depletion in a continuous-wave one-pump fiber optical parametric amplifier. *Opt. Lett.*, 26(9):620–622, 2001.

- [Masluk et al., 2012] N. A. Masluk, I. M. Pop, A. Kamal, Z. K. Mineev, and M. H. Devoret. Microwave characterization of Josephson junction arrays: Implementing a low loss superinductance. *Phys. Rev. Lett.*, 109:137002, 2012.
- [Metcalf et al., 2007] M. Metcalfe, E. Boaknin, V. Manucharyan, R. Vijay, I. Siddiqi, C. Rigetti, L. Frunzio, R. J. Schoelkopf, and M. H. Devoret. Measuring the decoherence of a qutrit qubit with the cavity bifurcation amplifier. *Phys. Rev. B*, 76(17):174516, 2007.
- [Mück et al., 1998] M. Mück, M.-O. Andre, J. Clarke, J. Gail, and C. Heiden. Radio-frequency amplifier based on a niobium dc superconducting quantum interference device with microstrip input coupling. *Applied Physics Letters*, 72(22):2885–2887, 1998.
- [Mück et al., 2001] M. Mück, J. B. Kycia, and J. Clarke. Superconducting quantum interference device as a near-quantum-limited amplifier at 0.5 GHz. *Applied Physics Letters*, 78(7):967–969, 2001.
- [Nandkishore and Levitov, 2011] R. Nandkishore and L. Levitov. Polar kerr effect and time reversal symmetry breaking in bilayer graphene. *Phys. Rev. Lett.*, 107:097402, 2011.
- [Orfanidis, 2008] S. J. Orfanidis. Electromagnetic waves and antennas, 2008. Available as an ebook at [www.ece.rutgers.edu/~orfanidi/ewa](http://www.ece.rutgers.edu/~orfanidi/ewa).
- [Pamtech] Pamtech. <http://pamtechinc.com/cryogenic-components/>.
- [Polder, 1949] D. Polder. On the theory of electromagnetic resonance. *Phil. Mag.*, 40:99, 1949.
- [Pozar, 2005] D. M. Pozar. *Microwave Engineering*. Wiley, ed. 3, 2005.

- [Ribeill et al., 2011] G. J. Ribeill, D. Hover, Y.-F. Chen, S. Zhu, and R. McDermott. Superconducting low-inductance undulatory galvanometer microwave amplifier: Theory. *Journal of Applied Physics*, 110(10):103901, 2011.
- [Schoelkopf] R. J. Schoelkopf. *Studies of noise in Josephson-effect mixers and their potential for submillimeter heterodyne detection*. PhD thesis, California Institute of Technology, Pasadena.
- [Shapiro, 1963] S. Shapiro. Josephson currents in superconducting tunneling: The effect of microwaves and other observations. *Phys. Rev. Lett.*, 11:80–82, 1963.
- [Shinagawa, 2000] K. Shinagawa. Faraday and Kerr effects in ferromagnets. In S. Sugano and N. Kojima, editors, *Magneto-Optics*, pages 137–178, Heidelberg, Germany, 2000. Springer.
- [Siddiqi] I. Siddiqi. private communication.
- [Spietz et al., 2008] L. Spietz, K. Irwin, and J. Aumentado. Input impedance and gain of a gigahertz amplifier using a dc superconducting quantum interference device in a quarter wave resonator. *Applied Physics Letters*, 93(8):082506, 2008.
- [Tesche and Clarke, 1977] C. D. Tesche and J. Clarke. dc squid: noise and optimization. *J. Low. Temp. Phys.*, 27:301–331, 1977.
- [Teufel et al., 2008] J. D. Teufel, J. W. Harlow, C. A. Regal, and K. W. Lehnert. Dynamical backaction of microwave fields on a nanomechanical oscillator. *Phys. Rev. Lett.*, 101:197203, 2008.
- [Teufel et al., 2011] J. D. Teufel, T. Donner, D. Li, J. W. Harlow, M. S. Allman, K. Cicak, A. J. Sirois, J. D. Whittaker, K. W. Lehnert, and R. W. Simmonds. Sideband cooling of micromechanical motion to the quantum ground state. *Nature*, 475: 359–363, 2011.

- [Tholen et al., 2007] E. A. Tholen, A. Ergul, E. M. Doherty, F. M. Weber, F. Gregis, and D. B. Haviland. Nonlinearities and parametric amplification in superconducting coplanar waveguide resonators. *Applied Physics Letters*, 90:253509, 2007.
- [Tien, 1961] P. K. Tien. Traveling wave parametric amplifier. (Patent 3012203), 1961. URL <http://www.archpatent.com/patents/3012203>.
- [Tinkham, 1996] M. Tinkham. *Introduction to superconductivity*. Dover Publications Inc., Mineola, New York, 1996.
- [Tucker, 1979] J. R. Tucker. Quantum limited detection in tunnel junction mixers. *IEEE Journal of Quantum Electronics*, 15:1234–1258, 1979.
- [Tucker and Feldman, 1985] J. R. Tucker and M. J. Feldman. Quantum detection at millimeter wavelengths. *Rev. Mod. Phys.*, 57:1055–1113, 1985.
- [Vijay et al., 2009] R. Vijay, M. H. Devoret, and I. Siddiqi. Invited review article: The Josephson bifurcation amplifier. *Review of Scientific Instruments*, 80(11):111101, 2009.
- [Wallraff et al., 2004] A. Wallraff, D. I. Schuster, A. Blais, L. Frunzio, R.-S. Huang, J. Majer, S. Kumar, S. M. Girvin, and R. J. Schoelkopf. Strong coupling of a single photon to a superconducting qubit using circuit quantum electrodynamics. *Nature*, 431:162, 2004.
- [Wang et al., 2008] Z. Wang, Y. D. Chong, J. D. Joannopoulos, and M. Soljačić. Reflection-free one-way edge modes in a gyromagnetic photonic crystal. *Phys. Rev. Lett.*, 100:013905, 2008.
- [Wellstood et al., 1994] F. C. Wellstood, C. Urbina, and J. Clarke. Hot-electron effects in metals. *Phys. Rev. B*, 49:5942–5955, 1994.

- [[Yamamoto et al., 2008](#)] T. Yamamoto, K. Inomata, M. Watanabe, K. Matsuba, T. Miyazaki, W. D. Oliver, Y. Nakamura, and J. S. Tsai. Flux-driven Josephson parametric amplifier. *Appl. Phys. Lett.*, 93(4):042510, 2008.
- [[Yariv, 1997](#)] A. Yariv. *Optical Electronics in Modern Communications*. Oxford University Press, 1997.
- [[Yurke, 2004](#)] B. Yurke. Input output theory (chapter 3). In P. Drummond and Z. Ficek, editors, *Quantum Squeezing*, pages 53–95. Springer, 2004.